ISBN 978-82-326-0494-4 (printed version)
ISBN 978-82-326-0495-1 (electronic version)
ISSN 1503-8181

Doctoral Thesis

Joakim Haugen

Doctoral theses at NTNU, 2014:291

Joakim Haugen

# Autonomous Aerial Ice Observation

**NTNU**
Norwegian University of
Science and Technology
Faculty of Information Technology,
Mathematics and Electrical Engineering
Department of Engineering Cybernetics

**NTNU – Trondheim**
Norwegian University of
Science and Technology

Doctoral theses at NTNU, 2014:291

NTNU

**NTNU – Trondheim**
Norwegian University of
Science and Technology

Joakim Haugen

# Autonomous Aerial Ice Observation

Thesis for the degree of Philosophiae Doctor

Trondheim, October 2014

Norwegian University of Science and Technology
Faculty of Information Technology,
Mathematics and Electrical Engineering
Department of Engineering Cybernetics

**NTNU – Trondheim**
Norwegian University of
Science and Technology

**NTNU**
Norwegian University of Science and Technology

Thesis for the degree of Philosophiae Doctor

Faculty of Information Technology,
Mathematics and Electrical Engineering
Department of Engineering Cybernetics



ISBN 978-82-326-0494-4 (printed version)
ISBN 978-82-326-0495-1 (electronic version)
ISSN 1503-8181
ITK Report 2014-6-W

Doctoral theses at NTNU, 2014:291

Printed by Skipnes Kommunikasjon as

# Summary

This work is concerned with autonomous aerial ice observation. Ice observation is a supporting activity in cold regions marine operations that are disturbed by various ice features. This supporting activity is motivated by the requirement of maintaining an awareness map of the surrounding ice conditions in order to execute an operation in a responsible manner. It is desired that the ice monitoring occurs both efficiently and as autonomously as possible. A part of the ice monitoring is thus to construct frameworks that are capable of executing various monitoring tasks without, or with minimal human intervention.

Chapter 2 covers viable instrumentation configurations for remotely sensing different ice features from unmanned aerial vehicles. The chapter also motivates the use of unmanned aerial vehicles together with other sensor platforms, so that the strengths and weaknesses of the various sensor platforms can be exploited when maintaining the ice condition awareness map.

The task of monitoring moving surface objects, often called *target tracking*, is examined in Chapter 3. We make use of nonlinear programming to construct feasible continuous trajectories for mobile sensing agents. The proposed framework uses each object's Riccati differential equation, which is based on the continuous extended Kalman filter, in feasibly guiding the mobile agents between the objects. The framework is validated by a full-scale hybrid experiment where a singular fixed-wing aircraft monitors three simulated objects in a constricted region of operation.

We also explore the nonlinear programming approach in solving the *dynamic coverage problem* in Chapter 4. Here, the task is to remotely monitor a dynamic process in a planar region with mobile sensor agents. As in Chapter 3, the mobile sensor agents have maneuverability constraints that the framework takes into consideration when finding paths that the sensors should follow. The framework employs a simpler model, compared to the Riccati equation in Chapter 3, in describing how the possible information reward changes in space and time. The machinery of control theory and Lyapunov functions is investigated in Chapter 5 as a more computational efficient alternative to the nonlinear programming approach.

# Preface

This thesis is submitted in partial fulfillment of the requirements for the degree of philosophiae doctor (PhD) at the Norwegian University of Science and Technology (NTNU). The research has been conducted at the Department of Engineering Cybernetics during the period between August 2010 and February 2014. My supervisor has been Prof. Lars Imsland and co-supervisors have been Prof. Roger Skjetne and Prof. Sveinung Løset. This work was supported by the Norwegian Research Council through the KMB: Arctic DP project 199567/I40 with its consortium partners Statoil, Det norske Veritas, and Kongsberg Gruppen.

## Acknowledgments

There are many people that have contributed in different ways during the course of my PhD work. I would like to thank all of them. The people in the following list deserve particular recognition:

**Supervisor:** Prof. Lars Imsland.

**Friends and colleagues at the Department of Engineering Cybernetics:** Christoph Backi, Anne Mai Ersdal, Esten Grøtli, Tor Aksel Heirung, Eleni Kelasidi, Brage Knudsen, Phillip Maree, Lars Semb, Kristoffer Skøien, and Anders Willersrud.

**Arctic DP project members:** Kenneth Eik, Ulrik Jørgensen, Øivind Kjerstad, Prof. Sveinung Løset, Ivan Metrikin, Francesco Scibilia, Prof. Roger Skjetne, Biao Su, Qin Zhang, and miscellaneous industry partners.

**Professional encounters:** Vegard Hovstein, Carl Erik Stephansen, Rune Storvold, and Maritime Robotics AS.

**Family:** The Haugens: Bjørn Arild and Gunn Margrethe, Daniel, and Silje Marlen.

**Undisclosed persons** .

*Joakim Haugen*
*Trondheim, August 2014*

# Contents

# List of figures

# List of tables

# Abbreviations

Abbreviations

**ADR** advection-diffusion-reaction.

**CIS** Canadian Ice Service.

**CPS** cyber-physical system.

**DP** dynamically positioned.

**DPS** distributed parameter system.

**EKF** extended Kalman filter.

**EnKF** ensemble Kalman filter.

**FIM** Fisher information matrix.

**FOV** field of view.

**GLONASS** global navigation satellite system.

**GNSS** global navigation satellite system.

**GPR** ground penetrating radar.

**GPS** global positioning system.

**GSD** ground sample distance.

**INS** inertial navigation system.

**IPOPT** interior point optimizer.

**ISIS** Ice Services Integrated System.

**IVP** initial value problem.

**MHE** moving horizon estimation.

**NLP** nonlinear programming.

**OCP** optimal control problem.

**ODE** ordinary differential equation.

**PDE** partial differential equation.

**RPAS** remotely piloted aircraft system.

**SAR** synthetic aperture radar.
**SUPG** streamline upwind Petrov-Galerkin.

**TIR** thermal infrared.

**UAV** unmanned aerial vehicle.
**UKF** unscented Kalman filter.
**USV** unmanned surface vehicle.
**UUV** unmanned underwater vehicle.

**VNIR** visible to near infrared.
**VTOL** vertical take-off and landing.

# Chapter 1

# Introduction

The scope of this work is to construct path planning schemes for unmanned aerial vehicles (UAVs) with the purpose to remotely collect information about various ice features in ice-infested waters. This chapter provides relevant motivation and context for the research problems examined in later chapters.

## 1.1 Arctic Dynamic Positioning

The United States Geological Survey has estimated that a considerable amount of the undiscovered oil and gas resources are located north of the Arctic Circle (Gautier et al., 2009). These resources are becoming increasingly more attractive to develop. Low-cost petroleum resources are rarer than before, and the recent retreat of polar ice may make exploration and development of offshore petroleum in cold regions a reality in the future.

An increased human intervention in cold regions will involve the presence of vessels carrying out various types of tasks such as: lifting, installation, crew change, evacuation, maintenance, and drilling (Gürtner et al., 2012). These tasks often require the relevant vessels to perform stationkeeping, that is, remain at a fixed location, or more generally, to be dynamically positioned (DP), for instance slowly maneuvering close to an offshore installation (Fossen, 2011, Ch. 6). The existing technology for performing dynamic positioning is intended for open water conditions. The ice in ice-infested waters greatly contributes to the external forcing on the DP vessel and Jenssen et al. (2009); Kuehnlein (2009) concluded that new control systems need to take these forces into account to permit good Arctic DP performance.

The very first Arctic DP operation was performed in May–June 1999 offshore the island Sakhalin, Russia in the Pacific Ocean. The purpose of the operation was to support a diving mission. The DP vessel was assisted by two icebreakers, whose task was to perform *physical ice management*. Sea ice physical management involves reducing the severity of the drifting sea ice moving toward the DP vessel, see Fig. 1.1. The ice conditions were considered highly dynamic, with ice coverage of typically 90 %, but also as low as 0 %. The ice were recorded with thicknesses ranging from 0.7 m to 1.5 m, drifting at speeds up to 1.0 m $s^{-1}$. The ice also included

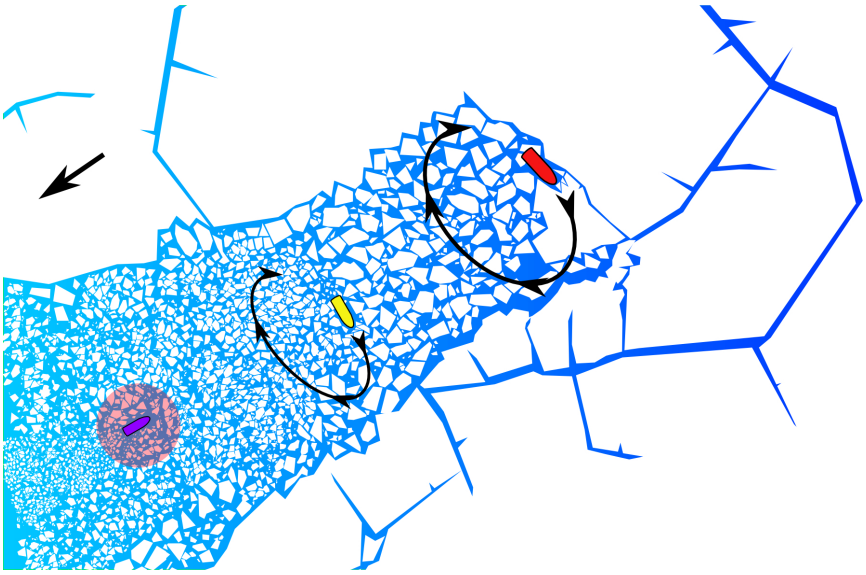

**Figure 1.1** Illustration of a dynamic positioning operation, which is supported by two upstream icebreakers that perform sea ice physical management.

severe ice conditions, such as occasional occurrences of ice ridges (see Fig. 1.2) with up to 5 m sails.

In August–September 2004 another Arctic DP operation, Arctic Coring Expedition, was conducted in the polar ice pack of the Arctic Ocean (K. Moran et al., 2006). The operation performed drilling for core sediment samples more than 400 m below the seabed, which was at up to 1300 m water depths. The operation experienced severe multi-year ice, but with the help of two icebreakers, the DP drilling ship remained mostly within the operational envelope without having to suspend the dynamic positioning. The managed ice that drifted toward the DP ship necessitated human intervention in controlling the position of the vessel.

The above pioneering full-scale experiments of DP in ice, together with similar operations, such as iceberg detection and tracking (see Eik (2008)), learned that a wide range of supporting activities are essential for responsible and safe offshore operations in cold regions.

### 1.1.1 Ice Defense

Arctic Marine Solutions (2014) uses *ice defense* as the aggregate term for supporting activities involved in cold regions marine operations such as Arctic DP. Important activities in ice defensing include (Eik, 2008; Keinonen, 2008):

- Protecting the DP vessel or structure from hazardous ice through physical ice management (e.g. ice breaking and/or iceberg towing).
- Gathering and processing information for decision support.
- Decision-making such as operational threat assessment and strategies.

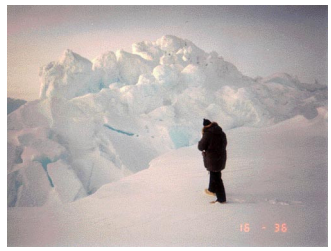

**Figure 1.2** An ice ridge is a pile of broken ice floes stacked on top of each other, both over (sail) and under (keel) the water. Photo courtesy of Ben Holt and Susan Digby.

A utopian objective of ice defense operations includes creating a complete ice features awareness map of a vast spatial region and maintaining it continuously over time. This is neither economically nor practically feasible, so prioritization of the information gathering is needed. The region surrounding the DP operation is often divided into different zones depending on the estimated time of arrival (ETA) of the drifting ice (Edmond et al., 2011; Sheykin, 2010). In the various zones, distinct monitoring objectives apply with different required level of urgency and detail. We divide the region into three conceptual surveillance zones:

**Far-field zone.** Here, we execute regional surveillance/coverage for detection and classification of hazardous ice features such as icebergs, ice ridges, and ice cover type. This information is crucial for threat assessment and operation planning. 1–7 days upstream.

**Mid-field zone.** This is the area within which ice features may reach the region where sea ice physical management is finding place. Ice identification (of for instance ice drift dynamics, ice concentration, and ice thickness) is important for operational efficiency, such as the choice of both ice breaking strategy and tactics (Hamilton et al., 2011). 6–24 hours upstream.

**Close-field zone.** The region of ice that most likely will reach the DP vessel. Detailed information about the ice feature geometry, ice thickness, ice concentration, ice drift velocity, and more may all be important for good DP performance (Metrikin et al., 2013). Up to a few hours upstream.

The zones have different extents and no single sensor platform is able to perform all the monitoring tasks by itself. Eik et al. (2009) motivates unmanned underwater vehicles (UUVs) as a tool in collecting ice intelligence for ice defense, whereas Haugen et al. (2011) (contained in Chapter 2) motivates UAVs to do the same together several other sensor platforms in a collaborative effort, see Fig. 1.3.

The sensor platforms constitute an ice observation system, which is an integral part of both the ice defense and the dynamic positioning. Since the resources are constrained with respect to cost, physical, and practical considerations, some kind of high-level task allocation procedures need to choose the appropriate sensor platforms for the required monitoring tasks. This task allocation happens both before and during the operation execution:

**In the planning phase,** decisions such as the choice of immobile sensors, type and number of mobile sensor platforms are made. These choices are made

**Figure 1.3** Illustration of a possible future Arctic dynamic positioning operation that consists of many important components, including icebreakers, unmanned underwater vehicles, and unmanned aerial vehicles. Picture courtesy of Bjarne Stenberg.

based on the required level of information and redundancy for the particular operation in question.

**During the operation** *dynamic mission planning* occurs, which involves allocating needed tasks to the fleet of singular or teams of mobile sensor networks. The dynamic planning allows for low response times in deployment and may facilitate real-time acquisition of information, so that important operational decisions can be made. There is a wide range of monitoring missions that may be needed in ice defensing. With respect to the mid-field and far-field zones, possible missions for remotely piloted aircraft systems (RPASs) are:

**Mission 1.** *Iceberg and ice ridge detection, identification, and tracking.*

**Mission 2.** *Sea ice identification and dynamic coverage.*

## 1.2 Remotely Piloted Aircraft Systems in Cold Regions

A remotely piloted aircraft system (RPAS) is a subgroup of the more general category of unmanned aircraft systems (UASs). The RPAS consists all the components needed to operate such a system: one or several UAVs, a ground station including the pilot station, launch and recovery systems, communication equipment, and more (CAA–Norway, 2014). A RPAS may be autonomous in the sense that the


**Figure 1.4** A launch system for the CryoWing fixed-wing aircraft operated by Norut (2014) in Longyearbyen, Svalbard, May 2011.

system can make its own decisions during the course of operation execution, but with the restriction that an operator can intervene and remotely pilot the UAVs.

The inclusion of RPASs in cold regions comes with a whole range of challenges that need to be addressed. Common keywords when talking about operations in Arctic regions are remoteness, darkness, and low temperatures. Robustness against these attributes is very important and may include sophisticated launch and recovery systems from ships (Crowe et al., 2012), robust communication systems (Frew et al., 2009), and fault-tolerant guidance, navigation, and control (GNC) systems. Other aspects that need to be addressed include (Crowe et al., 2012; Haugen et al., 2011): icing problems, vibration issues, water intrusion, and airspace access. Norwegian research communities working with problems connected to RPAS in cold regions include AMOS (2014); Norut (2014); Simicon (2011).

### 1.2.1 Autonomous Aerial Ice Observation

Apart from GNC, one aspect of an autonomous aircraft system is its ability to create paths that help in solving some monitoring task. In a cold regions operation setting, one can think of many different tasks that need a specialized system that can perceive its environment and make intelligent decisions based on the observations. In this thesis, we are concerned with the following ice observation sub-tasks: *target tracking*, related to Mission 1, and *dynamic coverage control*, related to Mission 2.

#### Target Tracking

Suppose a set of possibly hazardous icebergs and ice ridges has been detected in the far-field zone with the use of satellites. The acquired satellite data are of too coarse resolution to provide conclusive answers (Eik, 2008; Haugen et al., 2011). To confirm/refute the possible hazards, current practices involve manned aircraft (Eik, 2008) and reconnaissance vessels (Sheykin, 2010). We motivate the use of UAVs as a tool which may reduce costs and environmental footprint when solving this monitoring task. The task is formulated as a *target tracking* objective and

approached by assuming that a small number of UAVs is dispatched to remotely gather more information before further actions are taken.

The target tracking problem is the task of monitoring mobile or immobile objects using (usually mobile) sensor agents. Many problems can be cast as a target tracking problem, so the literature is rich on various approaches, see Haugen et al. (2014b) (contained in Chapter 3) and references therein. Haugen et al. (ibid.) classify contributions as "$n_m$ to $n_o$" tracking, where $n_m$ is the number of sensors and $n_o$ is the number of objects. The above defined problem is a multi-target tracking objective, where the number of mobile sensor agents are possibly more than one.

In solving the target tracking problem, contributions usually choose between two main methodologies: resource allocation and information-driven approaches. In the resource allocation problem, the targets are prescribed to be visited a predefined number of times. It is formulated as a modified traveling salesperson problem (Looker, 2008; Rathinam et al., 2007; Savla et al., 2008), often taking the limited turning radius of the mobile sensor into account. Unlike resource allocation, information-driven methods define the visitations of the targets according to some information reward. Information gradients are usually utilized in the formulation of optimization problems, which are seeking to minimize measures related to the information level, either minimize time between target measurements (Tang et al., 2005), maximize observation time (Parker, 1999), or minimizing the targets' estimation error covariance (Haugen et al., 2013a,b, 2014b).

### Dynamic Coverage Control

Imagine you want to get an awareness map of a bounded region in the mid-field zone. When creating this awareness map may, one task may be to get more detailed information about relevant ice conditions, for instance the ice concentration, which is the area fraction of ice versus open water. Current approaches include using satellites, reconnaissance vessels, and marine radars (Sheykin, 2010). We propose to use UAVs to cover the region of interest. Since the ice has a drifting velocity, the task can be formulated as a *dynamic coverage problem*.

Wang et al. (2012) describes the dynamic coverage problem as the problem of covering a given region using mobile sensor networks. The desired information to be gathered changes in both time and space, so a non-dynamic coverage algorithm may not be sufficient to capture the information with the required level of accuracy. The monitoring task is therefore to perform state estimation of some distributed parameter system (DPS), usually described as a partial differential equation (PDE).

Previous work on state estimation dynamic coverage falls under two main approaches: optimal control formulations (Burns et al., 2009; Choi et al., 2010; Haugen et al., 2014a), and gradient-based guidance algorithms (Demetriou, 2010; Demetriou et al., 2009; Haugen et al., 2012), for which Haugen et al. (2014a) and Haugen et al. (2012) are contained in Chapters 4 and 5, respectively. In the optimal control problem (OCP) formulation, one seeks to minimize some kind of objective functions that quantify the information reward of visiting a particular region. The formulations often use a measure based on the estimation error covariance dynamics (Burns et al., 2009; Choi et al., 2010), but to facilitate computational speed, simplified information dynamics has also been proposed (Haugen et al., 2014a).

Gradient-based guidance algorithms are more computationally efficient, but often rely on locally available estimation error to guide the vehicles (Demetriou, 2010; Demetriou et al., 2009; Haugen et al., 2012).

### 1.2.2 Scope of this Thesis

There are several important aspects that need to be addressed when solving the given aerial ice observation tasks. We mainly restrict our attention to design frameworks that promote autonomy of the path determination. Hence, the mobile sensor agents should solve the path planning tasks without, or with minimal human involvement. We further assume that the agents operate in uncluttered environments, except the cooperating mobile agents themselves, so collision avoidance of foreign objects or no-fly-zones inside the convex mission domain are not considered. However, it is important that cooperating agents avoid collision with each other, and that the agents remain within a bounded admissible region, since other missions may occur outside this region. A mobile sensor usually have maneuverability constraints, for instance limited turning radius if it is a fixed-wing aircraft. To encourage compliance between requested and executed flown paths, the mobile sensors' maneuverability constraints should be taken into consideration when planning paths for the monitoring tasks.

It would be beneficial if the solution proposals showed flexibility in the formulations, so that additional requirements could be included without too much difficulty. This includes the possibility of integrating the frameworks with high-level manipulation, e.g. to dynamically change the mission parameters during execution, for instance changing the number of mobile sensors agents or the environment to monitor. In this work, however, we focus on the task of autonomously finding efficient paths that solve given target tracking or dynamic coverage problems. We will only consider cooperative and centralized approaches, where the path planning algorithms themselves are the center of attention, not other features of RPASs, such as communication limitations, *et cetera*.

## 1.3 Research Methods

The requirements within the above defined scope need to be taken into consideration when investigating the target tracking and dynamic coverage problems. To do so, the two main contributions of this thesis involve formulating the research questions as optimal control problems. We are concerned with constructing path planning designs that exhibit real-time feasibility. Hence, there should be some focus on using state of the art tools that facilitate implementations that can be used in real-world scenarios. In this context, wired communication with a commercial RPAS's ground station, as part of a field experiment, is considered as one of the tasks in verifying the proposed design. The proposed frameworks are mostly verified through numerical simulations, but some full-scale hybrid experiments are also performed as proof-of-concept.

### 1.3.1 Optimal Control Problem (OCP)

An optimal control problem deals with finding control inputs of a dynamic system in such a way that a scalar objective function is locally minimized. There are three main components of the OCPs used in this thesis, an objective function (1.1a), an initial value problem (IVP) of an ordinary differential equation (ODE) (1.1b), and algebraic path constraints (1.1c). Let $x(t)$ be the state vector, $u(t)$ the control vector, and $t$ the time, with $t \in [t_0, t_f]$. The general Bolza-type optimal control problem (Biegler, 2010, Sec. 8.3) is written as

$$\min_u \quad J(t,u) = \Phi_L(t,u) + \Phi_M(t_f) \tag{1.1a}$$

subject to (s.t.)

$$\frac{dx}{dt} = f(t,x,u), \qquad x(t_0) = x_0, \tag{1.1b}$$

$$g_I(t,x,u) \leq 0, \qquad g_E(t,x,u) = 0 \tag{1.1c}$$

The above OCP consists of both a Lagrange integral term

$$\Phi_L(t,u) = \int_{t_0}^{t_f} \phi_L(t,x(t),u(t))dt, \tag{1.2a}$$

and a Mayer terminal cost term

$$\Phi_M(t_f) = \phi_M(t_f, x(t_f)). \tag{1.2b}$$

The OCP formulation has the benefit that it often is straightforward to include various types of dynamic systems and restrictions like the ones outlined in Section 1.2.2. Finding analytic solutions to these problems are often very difficult, but there exist several approaches to solve the problem numerically.

#### Numerical Solution to Optimal Control Problems

Biegler (ibid., Sec. 8.6) describes two main approaches for solving OCPs: "optimize then discretize" and "discretize then optimize". The *direct collocation* method (Biegler, 1984), which falls under the latter category, is a simultaneous approach where both the states and controls are discretized in time, giving a so-called nonlinear programming (NLP) problem. Other methods of the "discretize then optimize" approach include single and multiple shooting methods. In this thesis, only direct collocation has been used because the resulting NLP problem is sparse and contains structure that can be exploited by NLP solvers. A NLP problem has the form

$$\min_z \quad F(z) \tag{1.3a}$$

s. t.

$$g(z) = 0, \tag{1.3b}$$

$$h(z) \leq 0. \tag{1.3c}$$

These problems quickly become big, so in order to strive for real-time solutions, the receding horizon approach has been employed, that is, successive finite time

horizon problems have been solved. Notable state of the art libraries we use to solve the NLPs include IPOPT (Wächter et al., 2006), CasADi (Andersson et al., 2012), and OpenBLAS (Xianyi et al., 2012) on a C++ programming platform. Books on OCP, NLP, and direct collocation include Betts (2010); Biegler (2010).

## 1.4 Outline and Contributions

This thesis is divided into four main parts, each considering different aspects of autonomous monitoring in cold regions. The contents of each chapter are self-contained, and can therefore be read independently.

**Chapter 2** motivates the need for cost-effective ice monitoring systems in polar marine activities. The main contributions in this part are:

1. The definition of important components in an ice monitoring system.
2. A comparison of possible sensor platforms.
3. The motivation and benefits of an UAV as a sensor platform.

This part consists of Haugen et al. (2011).

**Chapter 3** covers the topic of object monitoring using UAVs: The *target tracking* problem. The main contributions in this part are:

1. Design of an optimization-based mathematical framework for monitoring moving surface objects.
2. Full-scale hybrid experiments as validation of the framework.
3. An extension to create collision-free flight trajectories in the case of multiple mobile sensors.

This part is based on Haugen et al. (2013a,b, 2014b).

**Chapter 4** contains work on regional monitoring of a distributed parameter system: The *dynamic coverage control* problem. The main contributions in this part are:

1. Design of an optimization-based mathematical framework for monitoring a planar advection-diffusion PDE.
2. Case study where a drifting sea ice concentration field is monitored using both a singular, and multiple UAVs.

The work in Chapter 4 consists of Haugen et al. (2014a).

**Chapter 5** also considers the *dynamic coverage control* problem. The main contributions are:

1. A gradient-based guidance scheme for a planar advection PDE.
2. Numerical simulation of the approach with two mass-spring-damper mobile sensors that monitor a drifting sea ice thickness distribution field.

This part consists of Haugen et al. (2012).

## 1.5 Publications

The following list of publications form the basis of this thesis.

- **Haugen, J.** and Imsland, L. (Oct. 2014a). "Monitoring an Advection-Diffusion Process Using Aerial Mobile Sensors". In: *Unmanned Systems.* Submitted.
- **Haugen, J.** and Imsland, L. (2014b). "Monitoring Moving Objects Using Aerial Mobile Sensors". In: *IEEE Transactions on Control Systems Technology.* Accepted.
- **Haugen, J.** and Imsland, L. (Nov. 20–22, 2013b). "UAV Path Planning for Multitarget Tracking with Experiments". In: *Proceedings of the 2nd IFAC Workshop on Research, Development and Education of Unmanned Aerial Systems.* Compiègne, France, pp. 316–323.
- **Haugen, J.** and Imsland, L. (July 17–19, 2013a). "Optimization-Based Autonomous Remote Sensing of Surface Objects Using an Unmanned Aerial Vehicle". In: *Proceedings of 2013 European Control Conference (ECC).* Zurich, Switzerland, pp. 1242–1249.
- **Haugen, J.**, Grøtli, E. I., and Imsland, L. (Oct. 3–5, 2012). "State Estimation of Ice Thickness Distribution Using Mobile Sensors". In: *Proceedings of 2012 IEEE Multi-Conference on Systems and Control.* Dubrovnik, Croatia, pp. 336–343.
- **Haugen, J.**, Imsland, L., Løset, S. and Skjetne, R. (June 19–24, 2011). "Ice Observer System for Ice Management Operations". In: *Proceedings of the Twenty-first (2011) International Offshore and Polar Engineering Conference.* Maui, HI, USA, pp. 1120–1127.

# Chapter 2

# Ice Observer System for Ice Management Operations

*This chapter describes the structure of an ice observer system, which is intended to aid decisions regarding risk assessment of the ice environment, as well as control performance of dynamic positioning systems, in offshore operations. An ice observer system collects, analyses and employs ice intelligence during operations in ice. Furthermore, unmanned aerial vehicles (UAVs) are presented as a viable sensor platform for close and far field ice monitoring. The work presented in this chapter was published in Haugen et al. (2011).*

## 2.1 Introduction

MARINE activities in ice-infested regions rely on information about the environment to operate in a safe manner. Shipping activities in Arctic waters are of interest due to their possible favorable economic properties; the Northern Sea Route drastically reduces the traveling distance to the Far East compared to alternative routes through the Suez Canal or around Africa (Johannessen et al., 2007). Good ice information increases the confidence when determining routes in Arctic waters and thus reduces the risk of damage and additional transit time (Kubat et al., 2007a).

The US Geological Survey suggests that a quarter of the remaining oil and gas resources in the world are located in the Arctic (Eik, 2008). As a consequence, the hydrocarbon exploration and exploitation in Arctic waters are expected to increase in the future. When performing operations in ice-infested waters, reliable information about the surrounding environment is crucial. In open waters there exists extensive experience with respect to the influences of currents, waves, and wind on offshore installations and vessels. In regions exposed to sea ice and icebergs, on the other hand, limited experience is available. A convenient overview of previous and current operations in ice-infested waters can be found in Eik (ibid.). The common factor of all these operations is the necessity of some kind of *ice management* to ensure successful operation.

### 2.1.1 Ice Management

Eik (2008) defines *ice management* as:

**Definition 2.1.** "Ice management is the sum of all activities where the objective is to reduce or avoid actions from any kind of ice features. This will include, but is not limited to:

- Detection, tracking and forecasting of sea ice, ice ridges and icebergs
- Threat evaluation
- Physical ice management such as ice breaking and iceberg towing
- Procedures for disconnection of offshore structures applied in search for or production of hydrocarbons."

The objective of detecting, tracking and forecasting ice features needs *ice intelligence*, which is the process of collecting and analyzing relevant information about the ice environment in a region of interest. Previous and current ice intelligence approaches include reconnaissance aircraft equipped with radar systems, satellite imagery, shipboard sensors, drift buoys and visual observations (Timco et al., 2005). Recently, subsurface ice intelligence systems have been motivated because the approach is weather-independent and ice characteristics are more distinct under water (Eik et al., 2009). However, none of the mentioned approaches is able to supply sufficient information about the ice situation by themselves (Eik, 2008). A complete *ice intelligence system* will thus consist of several sensor platforms for obtaining the required ice information in a collaborated effort; this also ensures a degree of redundancy, which is needed in a robust solution.

The amount of information provided by one such intelligence system may be daunting and time consuming to process by humans. Several different products exist where the purpose is to provide captains and operation managers with relevant information. At the Canadian Ice Service (CIS), a data pre-processing system called the Ice Services Integrated System (ISIS) makes the incoming data conveniently available for analysts and forecasters (Flett, 2003). The analyses are used in shipping through the software program Ice-Vu (Asmus et al., 1996), which delivers graphical ice charts, text-based bulletins and other advisory services (Timco et al., 2005). Other services include ICEWATCH, whose task is to monitor the Northern Sea Route (Johannessen et al., 1997) and ICEMON; sea ice monitoring in the polar regions (ICEMON, 2011).

Although these services are invaluable to operators in Arctic marine operations, an automated system is desired for processing the information in a more sophisticated manner, i.e. reduce the need for analysts and forecasters. Specifically, some kind of computer software must analyze the input data and provide useful output information. In this regard, output constitutes visualization to human operators, suggested operational decisions, and tasks to other automated systems. Previous work in the topic of automated interpretation of ice intelligence includes Soh et al. (2004). The authors present a promising approach to automated sea ice classification[1] using different data sources without human intervention. Other authors who

[1] Concentration and ice type in accordance with (WMO, 1989).

also employ data fusion in sea ice remote sensing include Beaven et al. (1996); Bogdanov et al. (2005); Partington (2000). The mentioned authors provide algorithms for extracting sea ice concentration from imagery.

To fully understand the spatial and temporal evolution of sea ice with respect to marine activities, it is of interest to obtain as much information about the sea ice as possible, for instance using unmanned aerial vehicles as a mobile sensor network. Later, we will discuss which ice features and parameters that are of relevance in this context. Once the information has been obtained, the next step is to use it in models to deduce something meaningful about the ice situation, both presently and in the future. These models can thus aid the determination of uncertainties in the picture of the ice situation. Using this knowledge is helpful in operational planning of mobile sensor networks.

## 2.2 Ice Observer System

If the environment affecting a marine floater or installation changes rapidly, an underlying control and decision system needs timely predictions of the actions exerted by the environment on the object in question. With proper design, a computer system is able to provide this information systematically in real-time. Thus, designing an automated ice observer system is beneficial with respect to safety and robustness in Arctic waters.

Developing one such automated ice observer system gives rise to several challenging aspects that must be addressed, such as:

- How should the system be structured to be robust and reliable?
- Which models and what fidelity are needed to describe the ice environment?
- What kind of information is needed for updating these models?
- How can this information be obtained?

The following sections will attempt to discuss these aspects in more detail.

### 2.2.1 Ice Observer System Structure

The urgency of accurate information varies; in some cases hazardous ice features must be identified in due time to prevent dangerous situations, whereas in other cases threatening ice features need not be identified at an early stage. These requirements depend on the flexibility of the operation. Specifically, in shipping there are several stages in planning a route through ice-infested waters. First, an initial route is set up. At this stage, highly detailed information is not needed since the ice situation is constantly changing and thus the information becomes less reliable after some time. During the journey through the waters, the captain needs updated information about the ice situation, and the area closest to the vessel is most critical (Timco et al., 2007). Similar deductions can be made for operations in search for or production of hydrocarbons in Arctic waters. A dynamically positioned (DP) vessel performing well intervention in an ice-infested water is affected by the surrounding ice (Hamilton et al., 2011; Keinonen, 2008). Aiding systems, such as icebreakers, must somehow minimize the ice actions exerted on the DP vessel. Since the various ice features need different ice-breaking strategies in order

to effectively reduce these ice actions, information about the incoming ice situation is needed to prepare for these maneuvers. Furthermore, hazardous ice features such as icebergs must be identified in due time to allow maneuvers to avoid collision, for instance, by aborting the DP operation or iceberg towing (Eik, 2010).

Economic and practical constraints limit the means that are available to acquire the ice information. Regardless of the available sensors, a general structure for the ice observer system can be outlined. The ice observer system can be set up as a hierarchically divided structure, see Fig. 2.1. In the *strategical* level the planning occurs. The geographical region in which the operation is going to find place is known. By taking ice states and predictions of future ice motion into account, the areas where better measurements are needed can be determined. Once the planning is finished, execution of the planned tasks are done on the *tactical* level, that is, the measurements are performed. This may include obtaining information from unmanned underwater vehicles (UUVs), unmanned surface vehicles (USVs), or UAVs in the region of interest. When the necessary information has been obtained, the next step is to *analyze* it. This includes image processing and utilizing the information in models that describe the current and future ice situation. Finally, the analyzed information is fed to other parts of the system. New planning occurs through a feedback to the strategical level. Thus, the system is an iterative process which constantly provides fresh information for future decisions. This process is similar to what is known as *data assimilation* in meteorological communities. In this paper we call this an *ice observer*. Once the ice information is readily available, the human operators receive appropriate visualizations of the existing information to aid the high-level decisions.

### 2.2.2 Ice Information

The goal of the ice observer system is to provide and present information such that a supervisory system can make assessments with respect to safety and accuracy of the operation (Eik, 2011). This includes the estimation of ice actions, which are local and global actions exerted on the structure(s) at hand (Løset et al., 2006). Different failure modes, such as crushing, buckling, cracking etc., come to play for various structural geometries, ice properties, and ice features (Sanderson, 1988). Furthermore, various failure modes introduce fundamental differences in the microscopic mechanics and the properties controlling them. For this reason it is difficult to determine which ice characteristics that are important to determine in the general case. Nevertheless, an overview of potentially relevant characteristics from an ice observer point of view is given in Fig. 2.2.

The ice observer's objective is, to the extent possible, to identify the parameters given in Fig. 2.2. This is a challenging objective, since measuring some of the ice properties are extremely difficult without doing *in situ* measurements (Eicken et al., 2009). Scaling effects also complicate the reliability of measurements. To overcome the inability to measure some parameters directly, estimates of these parameters can be obtained indirectly from the knowledge of other parameters, models and statistics (Lubin et al., 2006). For instance, possessing measurements of the sea ice temperatures aid the determination of its strength.

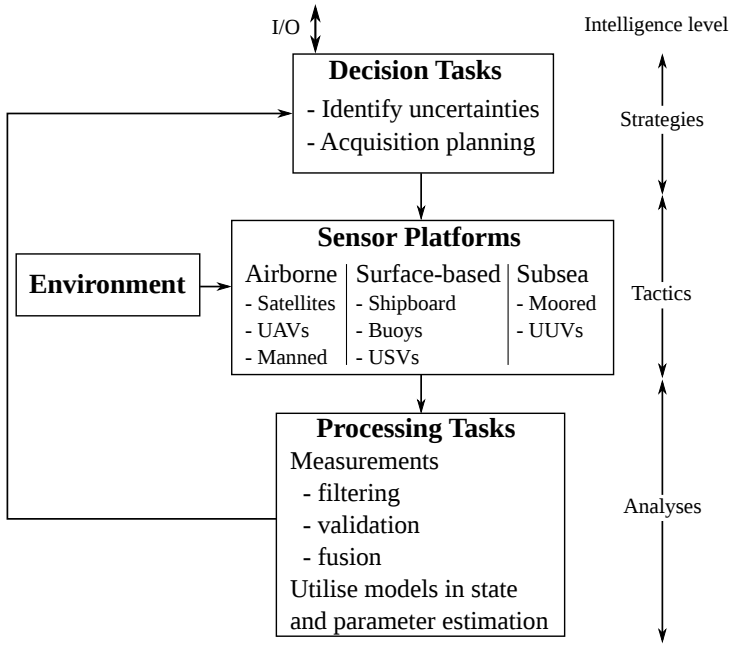


**Figure 2.1** The structure of an Ice Observer System.

Flett (2003) provides a table which shows the CIS ice information requirements. The information requirements are prioritized as follows:

**Primary**: ice edge, ice concentration, ice floe distribution, and stage of development.

**Secondary**: leads, ice thickness, ice topography and roughness, ice strength, and other ice properties.

The *stage of development* includes the ice type, i.e., whether it is new ice, first-year or multi-year ice. It is important to distinguish these ice types since the ice strength is significantly different. Flett's (2003) table also indicates required spatial and temporal resolution of the different information. One must keep in mind that the table provided by Flett (ibid.) is designed for creating ice charts in shipping, so local measurement requirements are not included.

### 2.2.3 Ice Modeling

Sea ice conditions can change rapidly and have big impact on marine activities. Hence, accurate forecasts are crucial for offshore operations, and therefore numerical ice models are needed to describe the ice environment.

**Sea ice dynamics** The physics of sea ice dynamics can be divided into four elements (Leppäranta, 2005):

(i) Conservation of momentum; the forces acting are external forcing from air and water, internal stresses, Coriolis force, etc.

(ii) Conservation of ice; ice thickness redistribution, ice growth and decay.

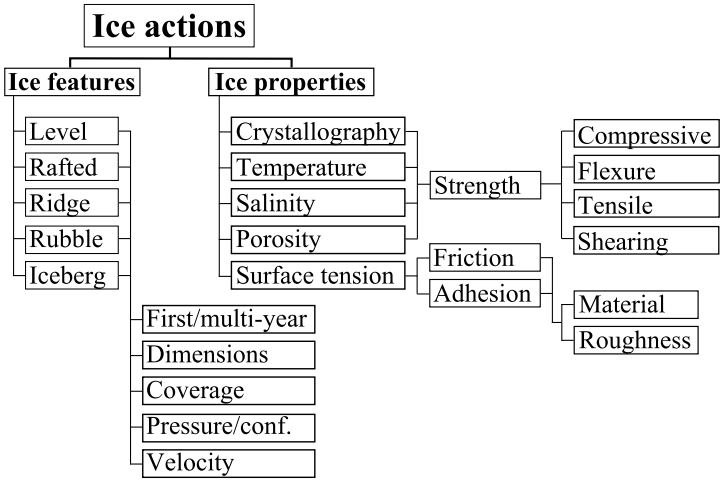


**Figure 2.2** Ice characteristics of interest.

(iii) Constitutive law; ice rheology, which relates stress to strength and deformation.
(iv) Ice states; parameters affecting ice strength, such as thickness and floe-size distribution.

The numerical methodology can either be discrete particle models or continuum models. Løset (1993) described a discrete element model, but on larger scale discrete models have traditionally been too computationally demanding, so continuum models are widely used. On the other hand, as pointed out by Leppäranta (2005), the continuum approach is only valid if the grid sizes are chosen sufficiently large. As a result, the continuum approach may not be applicable on scales relevant of operational ice modeling. An important property of the sea ice model is to accurately model ice features such as ice ridges and hummocks, since these features can consist of significant portion of the total ice volume. Consult Leppäranta (2005, 2011) for an in-depth overview of sea ice drift models.

**Iceberg drift and deterioration** Smith (1993) mentioned three different approaches in modeling iceberg drift trajectories:

- Statistical models using probability distributions of previous trajectories to predict velocity and position.
- Kinematic models with empirical relationships with other parameters, such as rule-of-thumbs.
- Dynamic models which estimate forces acting on an iceberg, that is, Newton's law of motion.

Extensive research efforts have been made to develop precise iceberg drift models using dynamic models. Long-term forecasting models (months) have been investigated by Bigg et al. (1997); Death et al. (2006); Eik (2009); Keghouche et al. (2009); Kubat et al. (2005), while short-term (<month) models have been discussed in Mountain (1980); Napoleoni (1979); Smith et al. (1983), to mention a

few. In the Grand Banks region, iceberg drift models are being used operationally to assess the inflow of icebergs (Kubat et al., 2007b).

**External forcing and model fidelity** Sea ice and iceberg drift models based on Newton's law of motion depend on input from both meteorological and oceanographic models. Models for wind and waves give today decent reproduction of relevant parameters, whereas oceanographic models still produce biases and offsets in the ocean current velocities (Eik, 2009). A high-fidelity model is pointless if the forces driving it are incorrect. On the other hand, a good model will closely follow the true state if these driving forces are modeled correctly. Thus, a coupled *met-ice-ocean model* will not be stronger than its weakest link. Furthermore, the environmental models in an ice observer structure will continuously be updated by measurements to reduce these error drifts. A major objective, which can be accomplished with estimation techniques, is how to optimally combine models and measurements.

### 2.2.4 Estimation Techniques

The models just outlined should mimic the true behavior of the ice environment, and could therefore be used to predict future ice dynamics. However, several issues reduce the validity and prediction capabilities of these models:

- Inaccurate models due to very complex phenomena.
- Limited complexity of model implementations for computational feasibility.
- Quality/availability of initial conditions, boundary conditions, and driving forces.

To minimize the effect of at least some of these issues, it is important to obtain as much additional information (measurements and other relevant information) about the ice environment, and use estimation techniques to fuse this information with the models.

There exist numerous estimation methods that are widely used in engineering and econometric solutions, such as control systems and macroeconomic models (Simon, 2006). The *Kalman filter* is an example of a recursive estimation method, but in its general form it is not suitable for nonlinear models. Hence, suboptimal variants such as extended Kalman filters (EKFs) and unscented Kalman filters (UKFs) have been developed (ibid.). These estimation methods use uncertainty information of models and measurements in the form of covariance matrices to determine the appropriate fusion of model and measurement. In large-scale systems, these covariance matrices become huge and make these Kalman filter algorithms intractable. To address this problem, the ensemble Kalman filter (EnKF) (Evensen, 2003) avoids propagating the covariance matrix by replacing it with a sample covariance. The EnKF is for instance used in environmental data assimilation of both atmospheric and ocean models (consult Evensen (ibid.) and references therein).

The estimation methods mentioned so far do not have built-in mechanisms for dealing with constraints in the estimations. For instance, in the case of a sea ice model, the estimations can in theory yield negative ice thicknesses, which is non-physical. Kalman filter variants which address constraints can be found in the

literature, but a more transparent and straightforward way of dealing with constraints is perhaps to use methods based on constrained numerical optimization, such as moving horizon estimation (MHE) (Rao et al., 2003). Moving horizon estimation combines information in previous estimates with a constrained optimization on a finite horizon of measurements to update the model state. Recent developments in large-scale optimization have made these approaches viable also for rather large-scale models.

## 2.3 Ice Monitoring Systems

In operational detection and monitoring of icebergs in the Grand Banks region there is extensive use of ice intelligence systems. They are needed to detect and track icebergs close to offshore installations with sufficient confidence (McClintock et al., 2007). Equivalently, when also monitoring sea ice in addition to icebergs and other ice features, several intelligence systems are needed to identify and track these features with satisfactory accuracy. The different sensor platforms possess both strengths and weaknesses. These attributes influence coverage, resolution and frequency of the measurements. As previously mentioned, none of the platforms can by themselves provide all the information that is needed in an ice observer system. Thus, considerations must be taken when choosing sensor platforms. The objective is therefore to create a synergy between the different platforms such that they complement each other with respect to coverage, spatial and temporal resolution, in addition to parameters that are measured. Table 2.1 depicts an overview of platforms and its applicable sensor types which is relevant in an ice observer system. As can be seen in the table, there is some overlap between the different platforms and which sensors that are applicable. Note that manned aircraft have the same instrumentation possibilities as UAVs.

**Resolution** of the sensing devices is important to consider when obtaining ice information. To capture the characteristics of remotely sensed objects, several attributes affect the reliability of the information. The ground sample distance (GSD), which is the distance between two captured pixels, determines whether or not an object can be distinguished from the surroundings. Each footprint is an average of the characteristics in that particular footprint. In terms of identifying ice features, the GSD must be sufficiently short to allow detection with required probability (Leachtenauer et al., 2001). Other resolution considerations include spectral resolution, radiometric resolution and data resolution.

### 2.3.1 Sensor Types

Different sensors have both appealing features and inherent drawbacks that influence the measured quantities. These properties are important to consider when choosing which sensors to utilize on a platform. The theoretical fundamentals of remote sensors are too comprehensive for this paper, but the main possibilities and limitations will be stated here for convenience. The material is mainly based on Lubin et al. (2006).

**Table 2.1** Sensor platform overview.

| | Platform | | | | |
|---|---|---|---|---|---|
| Sensor type | Satellite | UAV | Shipboard | Buoy | Underwater |
| Optical (VNIR and TIR) | ✓ | ✓ | ✓ | | |
| Laser altimeter/scanner | ✓ | ✓ | | | ✓ |
| Radiometer | ✓ | ✓ | ✓ | | |
| SAR | ✓ | ✓ | | | |
| Marine radar | | | ✓ | | |
| Scatterometer | ✓ | ✓ | | | |
| Radar altimeter | ✓ | ✓ | | | |
| Acoustic techniques | | | ✓ | | ✓ |
| Meteorological suite | | ✓ | ✓ | ✓ | |
| Oceanographic suite | | | ✓ | | ✓ |

**Visible to near infrared (VNIR)** is a part of the electromagnetic spectrum where reflections dominates the emission from Earth's surface. For these wavelengths, the albedo of the surface varies depending on the object's molecular structure, thickness, salinity and density (ibid.). The VNIR spectrum can thus be used in ice classification. The penetration depth of VNIR is not big, so even a thin snow cover will alter the albedo significantly. Clouds are also visible in this part of the spectrum and thus hampers measurements, whereas solar illumination is needed to obtain reflections. These drawbacks drastically reduce the applicability of such sensors, but on the bright side, these sensors permit very fine resolutions.

**Laser** devices emit laser pulses and records the time of the round trips to measure distances. This technique can be used by *laser altimeters* or *laser scanners*. If it is combined with geographic coordinates from a global navigation satellite system (GNSS), the surface elevation of the ice cover can be measured. Laser scanners shoots sequential laser pulses within a swath width and is thus an imaging device. This device can be used for topographic mapping of the ice cover. A drawback is its inability to penetrate dense clouds.

**Thermal infrared (TIR)** sensors measure emission from objects. This emission depends on temperature and emissivity and can be used to derive ice surface temperatures. This property can be exploited by high resolution TIR sensors in determination of ice motion, iceberg detection, and floe-size distribution (ibid.). Unlike the VNIR spectrum, solar illumination is not needed, but TIR radiation cannot easily penetrate cloud covers and can therefore only be used as a complementary sensor in ice intelligence applications.

**Passive microwave** techniques using radiometers can, as opposed to VNIR and TIR, penetrate both clouds and polar darkness, but might have problems in pre-

cipitating clouds. The radiation depends on the physical properties of the object, such as crystalline structure (Lubin et al., 2006). For this reason, differentiation of water and sea ice is possible. Unfortunately, there are high variability and uncertainty in the emissivity of sea ice (Comiso et al., 1989), which complicates the analysis of the obtained measurements. In addition, the emitted energy levels are small, so fine spatial resolution is limited.

**Active microwave** devices emit electromagnetic signals toward a region of interest and the reflections are detected by the device. There are three classes of commonly used active microwave devices in aerial remote sensing, namely synthetic aperture radars (SARs), scatterometers and radar altimeters (Lubin et al., 2006). Common for them all is their ability of penetrating clouds, polar darkness and even precipitation.

*SAR* is a high spatial resolution imaging technique that provides complex pictures of a region. The reflected signals depend on a number of physical properties of the depicted objects and are difficult to interpret. Under favorable conditions it is possible to classify different ice features and differentiate water from sea ice. This makes it possible to use SAR for ice-type classification, ice motion, ice deformation, et cetera. SAR is one of the few sensor types which, due to the penetration capabilities, is able to distinguish between first-year and multi-year ice. Favorable conditions are rarely the case, so interpretation of SAR images is challenging in the general case. Several techniques exist to overcome this challenge and depend on the technology of the SAR device. Important device parameters in this context include frequency band, polarization and incidence angle (consult Lubin et al. (ibid.)). Despite the mentioned difficulties, SAR as a sensory device is appealing due to all-weather, day and night possibilities.

A *scatterometer* records the energy backscattered from the surface. For sea ice, it can provide information about roughness and dielectric properties of the surface (ibid.). Despite its high temporal resolution and coverage, the coarse spatial resolution (km for satellite-borne scatterometers) limits usefulness in relatively small scale ice intelligence operations. On the other hand, SAR devices can operate as scatterometers (ISRO, 2011), which may be useful in some cases.

*Radar altimeters* measure the travel time of a pulse from the sensor to the object in question and back again. From this measurement it is possible to derive the distance between them. Radar altimeters can to some degree penetrate dry snow covers. This implies that the freeboard[2] can be measured in a similar fashion as laser altimeters through incorporation of geographic coordinates. By assuming hydrostatic equilibrium and estimating the density of the ice, the ice thickness can be estimated (Hendricks et al., 2006). To be able to do this, estimates of both the density and thickness of the snow cover are needed[3]. The main limitation of this device is its narrow footprint and thus limited coverage.

Shipboard marine radars have also been used for ice detection of hazardous multi-year ice and icebergs. Recently, O'Connell (2008) demonstrated a more sophisticated *ice hazard radar* for use in Arctic waters. This type of radar provides

[2]The elevation of the ice above the water surface.

[3]Snow cover thickness can be estimated by utilizing a laser altimeter.

more detailed images than conventional marine radars and can be used as an intelligence device in an ice observer system. The reliability of the measurements diminishes with distance from the vessel. If, for instance, the disconnection time of equipment attached to a dynamically positioned vessel is long in comparison to the reach of the radar, the inflow of hazardous ice features cannot always be detected in due time with this device.

**Acoustic sensors** are generally more suited for underwater platforms. Upward-looking sonars can be used to create the underwater topography of the sea ice (Wadhams et al., 2008). By employing the Doppler effect, the drift velocity of the ice cover can be estimated. Furthermore, it is possible to identify multi-year ice using this sensor type (ibid.). The main drawback of this sensor type is its limited coverage and propagation delays which greatly varies with temperature and salinity (Akyildiz et al., 2005).

**A meteorological suite** of sensors can measure temperature, wind velocity and humidity of the atmosphere. These measurements are important in meteorological models. Higher spatial and temporal resolution of these measurements can increase the accuracy of the weather forecasts in an area of interest. As a consequence, wind and temperature fields can be fed into the ice model and to achieve higher accuracy of the ice estimates.

**Oceanographic sensor suites** are useful in measuring water temperature, salinity, and currents. These states are important through interaction between sea ice and water, namely drag forces and heat flux. The mentioned states are very difficult to measure from airborne vehicles when the ocean is covered by ice floes.

**Other devices** of interest include:

**GNSS**: NAVISTAR's global positioning system (GPS), global navigation satellite system (GLONASS), and Galileo, which are needed for accurate geopostioning of measured data.

**Inertial navigation systems (INSs)**, which are complementary to GNSS.

**Electromagnetic systems** for thickness measurements. These may be too heavy ($\sim 100\,\mathrm{kg}$ (Hendricks et al., 2006)) to be applicable for small UAVs. However, for USVs it could be relevant.

**Ground penetrating radars (GPRs)** can be used for ice thickness measurements from a USV, but due to ice salinity, mixed success should be expected (Maijala et al., 1998).

### 2.3.2 Sensor Platforms

When evaluating the applicability of a sensor platform in an ice observer system, attributes such as cost, coverage, spatial and temporal resolution, as well as robustness, communication, and logistics are important to consider.

**Satellites** have for a long time been an invaluable platform for remote sensing. In the case of sea ice, much research effort has been invested in exploiting the sensors that have been deployed on various Earth orbiting satellites (for a thorough overview, see Lubin et al. (2006)). Today, a wide range of sea ice parameters can be estimated from space. However, due to the high altitudes of the satellites, inherent challenges and limitations exist with respect to the sensory performance. In particular, there are trade-offs between obtainable temporal and spatial resolution, as well as coverage (ibid.). Consequently, you cannot obtain fine-resolution imagery over huge areas at arbitrary sampling interval, one must prioritize one of these properties. In global climate models, large scale measurements of sea ice extent are of interest rather than highly detailed measurements at geographically small regions. Thus, global coverage at intermediate temporal and spatial resolutions is sufficient in most cases (ibid.).

For operational monitoring and forecasting of the environment, on the other hand, both fine temporal and spatial resolutions are desired, but with smaller geographical coverage. These demands are difficult to meet by using satellite sensors. Although spaceborne passive-microwave sensors provide daily coverage of the global sea ice cover, their spatial resolution is too coarse to identify ice features such as ice ridges with confidence (ibid.). Conversely, spaceborne SARs possess the spatial resolution to do so, but the temporal resolution may not be sufficiently fine for the sea ice models to predict inter-sample changes with required accuracy. Table 2.2 shows commercial satellites carrying SARs and a selection of their operating modes and properties. It is important to understand that the *repeat cycle*; the time span between two concurrent geographic projections of the satellite, is not the same as sampling interval (or *revisit time*; the time span between two consecutive measurements of a point), and it is hence possible to obtain finer temporal resolution than the repeat cycle in case of variable-swath direction SAR satellites (ibid.). Unfortunately, this is not necessarily true when the highest available spatial resolution of a satellite's operation mode is desired. Luckily, though, the revisit time of polar-orbiting satellites depends on the latitude of the desired measurement location; it is reduced closer to the poles due to reduced cross-track distance between the projected trajectories of the satellite's orbit. In sum, fine-resolution SAR satellite images can be obtained at sampling intervals in the range of a few days, perhaps even more often, but with varying spatial resolution depending on which satellite who provides them. It is also worth mentioning that some of these satellites do not have multi-polarization capability, which affects the confidence of the derived geophysical parameters.

As indicated in Table 2.1, there also exist satellites who carry other sensor types. But as discussed, these sensor types either cannot penetrate darkness and clouds, have coarse resolution, or provide too limited spatial coverage to operate on their own. Thus, all the remaining satellite sensors can be viewed as complementary sensors to the SAR. Still, it is important to acknowledge that these sensors indeed can provide additional information during problematic parts of the year. Specifically, microwave-based images are difficult to analyze during the melt season (ibid.), so complementary information are welcome when they are available.

**Table 2.2** Satellites equipped with SAR and some of their properties.

| Satellite | Band (IEEE, 1984) | Repeat cycle [days] | Operation mode | Resolution [m] | Swath width [km] |
|---|---|---|---|---|---|
| ERS-2 | C | 35 | - | $6 - 30 \times 26$ | 102.5 |
| ENVISAT | C | 35 | Image Mode | 30 | $58 - 109$ |
| RADARSAT-1 | C | 24 | Fine | 8 | 45 |
| RADARSAT-2 | C | 24 | Ultra-fine | $3 \times 3$ | 20 |
| ALOS | L | 46 | High Res. | $7 - 44$ | $40 - 70$ |
| TerraSAR-X | X | 11 | Spotlight | 1 | $5 \times 10$ |
| Cosmo-SkyMed (4 satellites) | X | 4? | Spotlight | 1 | $10 \times 10$ |

Source: (ibid., Appendix) and (Cosmo-SkyMed, 2011)

**Ships** will always be present in surface-based offshore operations. This fact implies that the ship as a sensor platform is relatively cheap and problems with communication and logistics are almost nonexistent. Table 2.1 shows possible instrumentation. Measurements can generally be obtained despite the weather or darkness. Certainly, some of the sensors are rendered inoperable in unfavorable conditions, but the marine radar is a robust sensor that provides year-round operation. Unfortunately, heavy sea can make it difficult to detect ice features (O'Connell, 2008). Care must be taken when placing sensors; environmental disturbances such as icing and ice-floes can damage the equipment.

**Buoys** provide accurate velocity data of the sea cover. This data can be used to validate ice drift velocities obtained by remote sensing (Heil et al., 2001). Moreover, by mounting a meteorological sensor suite on the buoy, atmospheric pressure, wind velocity, air temperatures can be measured with high geopositional accuracy (Lubin et al., 2006). Due to the cost, logistical difficulty of deployment and sparse coverage, the spatial resolution is limited. Nonetheless, such a platform would provide invaluable information to an ice observer system.

**Underwater** sensor platforms are the only sensor platform which are independent of weather conditions. This is a big advantage over other platforms, but this platform has characteristic shortcomings, such as cost, limited coverage, communication challenges, navigation, and difficulty of logistics. For an overview of research challenges with respect to underwater acoustic sensor networks, consult Akyildiz et al. (2005). Eik et al. (2009) specified requirements for a subsurface ice intelligence system.

**Table 2.3** Sensor platform comparison.

**(a)** Property comparison.

| | | Resolution | | |
|---|---|---|---|---|
| Platform | Coverage | Space | Time | Cost per area |
| Satellites | Excellent | Intermediate | Coarse | Intermediate |
| UAVs | Very good | Fine | Intermediate | Intermediate |
| Shipboard | Low | Intermediate | Fine | Low |
| Buoys | High | Sparse | Intermediate | High |
| USVs | Intermediate | Sparse | Low | High |
| Sub-sea | Good | Very fine | Intermediate | |

**(b)** Suitable region of operation.

| Platform | Suggested regions of operation |
|---|---|
| Satellites | Distant |
| UAVs | Distant, intermediate, close |
| Shipboard | Close |
| Buoys | Distant, intermediate |
| USVs | Intermediate |
| Sub-sea | Close, intermediate |

**A Summary** of the different sensor platforms in terms of coverage, resolution, and cost per area is given in Table 2.3. Based on these properties, the table also provides suggested regions of operation for the different sensor platforms.

### 2.3.3 UAV as a Sensor Platform

Unlike the previously discussed sensor platforms, UAVs demonstrate flexibility in geographical coverage, spatial and temporal resolution, and these abilities are important in sensor platforms. Thus, UAV is a strong candidate to operate as a sensor platform in an ice observer system. Nevertheless, there are many challenges that must be addressed in order to successfully employ unmanned aerial vehicles as part of an ice intelligence system.

The UAVs must be economically efficient to deploy, and they must compete with the other intelligence systems with respect to cost of information per area. Furthermore, manual intervention and maintenance of the vehicles should be minimal, employing as few people as possible. Thus, launch and recovery systems should be automated to enable all-weather, day and night operation, in addition to the data collection itself. Fault tolerance is a requirement since both the vehicles and the instrumentation are costly. Consequently, having high material quality reduces maintenance and increases the reliability of the UAVs.

Due to nonnegligible ice-modeling inaccuracies and uncertainties, the predicted ice conditions will eventually diverge from the true situation if measurements are not received. Continuity of information gathering is therefore essential to compensate these error drifts and maintain safe operation. Robustness against environmen-

tal disturbances such as extreme coldness, high wind speeds and icing problems is crucial to achieve this objective.

Fine resolution imaging produces big data volumes. This information needs to be processed and utilized as quickly as possible, requiring an efficient data communication system to a central processing unit. Since the vehicles may travel far away from the base and out of reach of direct communication, either satellite communication, or communication chaining is needed to transmit the input information in a timely manner (Frew et al., 2009).

Other aspects that must be addressed include vibration issues, water intrusion, fly zones, legislation, electromagnetic noise, guidance, navigation, and control (see Crowe et al. (2012) and references therein).

**UAV classification** The Unmanned Vehicle Systems International (UVSI, 2011) has classified unmanned aerial vehicles according to key properties such as weight, maximum payload, altitude, endurance, range, speed and so forth. These characteristics are important to consider when designing UAVs for Arctic intelligence operations. Notably, the UAV is supposed to operate as a sensor platform and the payload determines which and how many sensors that are possible to equip on the vehicle. Likewise, other attributes such as maximum altitude, endurance, range, and speed affect both coverage and spatial and temporal resolution. Moreover, weight and UAV design influence both maneuverability of the vehicles and robustness against environmental disturbances. There are also constraints in the physical size of the vehicles, which in particular impact space requirements for launch and recovery systems. In sum, there are many trade-offs during the design process. Currently, research and development on UAVs is being performed in a variety of locations. In Norway, Norut (2014) and Simicon (2011) are both doing research on UAVs for use in Arctic Environments.

UAV classes that should be considered as a sensor platform are:

**Rotary-wing vehicles** have vertical take-off and landing (VTOL) capabilities and good maneuverability, but intermediate range.

**Fixed-wing vehicles** have higher range capabilities than the other two classes, but at the cost of complex launch and recovery, and more limited maneuverability.

**Aerostats** have the least flexibility in terms of mobility, but on the other hand, endurance is achieved at low costs. A moored aerostat can operate during bad weather and can give a good overview over the close-field ice situation.

**Instrumentation** is one element of the UAV-design process which affects the output information of the sensor platform. In particular, the right choice of sensor devices is important in order to obtain reliable information about the ice environment with required degree of redundancy. The sensors have pros and cons, so the right sensor combination is an issue that must be addressed. Table 2.4 provides an overview of a selection of currently available sensors that can be mounted on a relatively small unmanned aerial vehicle. The specifications given in this table are a subset of all the attributes that affects the performance of the sensor platform. For instance, the operational temperature range of the Nikon digital camera is cer-

**Table 2.4** Specifications for UAV-applicable sensors.

| | Sensor type | | |
|---|---|---|---|
| Properties | Visible | TIR | Laser scanner |
| Sensor | D300s | Photon 640 | LMS-Q240i |
| Lens size [mm] | 50 | 35 | - |
| Weight [g] | 840 | 250 | $\sim 7000$ |
| Day and night | No | Yes | Yes |
| Fog | No | Light | Light |
| Range$^\star$ [m] | 140 | 140 | $0 - 500$ |
| Accuracy | - | 50 mK | 2 cm$^\dagger$ |
| GSD/footprint$^*$ [cm] | 3.3 | 20 | $\sim 80$ |
| Sampling frequency [Hz] | 7 | 30 | 10000 |
| Temperature range [°C] | 0 to +40 | −40 to +80 | −10 to +50 |
| Reference | Nikon (2011) | FLIR (2011) | RIEGL (2011) |
| | Sensor type | | |
| Properties | Laser altimeter | Radar altimeter | SAR |
| Sensor | ILM-R 300 | MRA Type 1 | NanoSAR B |
| Lens size [mm] | - | - | - |
| Weight [g] | 950 | 400 | 1600 |
| Day and night | Yes | Yes | Yes |
| Fog | Light | Yes | Yes |
| Range$^\star$ [m] | - | - | -$^\ddagger$ |
| Accuracy | 5 cm$^\dagger$ | 50 cm$^\dagger$ | - |
| GSD/footprint$^*$ [cm] | $\sim 90$ | - | 30 |
| Sampling frequency [Hz] | 9 | 10 | -$^\ddagger$ |
| Temperature range [°C] | −10 to +60 | −40 to +55 | -$^\ddagger$ |
| Reference | MDL (2011) | Roke (2011) | ImSAR (2011) |

$^\star$ Horizontal range at 300m altitude, depends on the FOV of the device.
$^*$ GSD in horizontal direction of image, or footprint diameter of beam.
$^\dagger$ Specified instrument accuracy at 300 m altitude, absolute accuracy combined with GPS is poorer.
$^\ddagger$ Not specified by vendor.
See Reuder et al. (2009) for an example of an meteorological sensor suite in UAVs.
A UAV-borne radiometer has been demonstrated by Acevo-Herrera et al. (2010).

tainly not wide enough to operate in a cold climate. Moreover, the temperature in Arctic regions can get far colder than −10 °C and the reliability of some of the sensors are thereby reduced.

Even though the sampling rates of the sensors are relatively high, a single measurement has very limited coverage. High operational altitude increases the coverage, but at the cost of spatial resolution. Thus, the sensor platform must be placed in an appropriate altitude to accommodate both required coverage and resolution. Table 2.4 shows the horizontal range at an altitude of 300 m and the corresponding GSD/footprint. As previously discussed, too coarse spatial resolution will increase the probability of not detecting hazardous ice features. When monitoring a specified region with the required spatial resolution, the platform must move around.

This mobility is not instantaneous, so to effectively cover a region, smartness must be incorporated in the path planning.

### 2.3.4 Mobile sensor networks

As far as the authors are aware, no published results on a mobile sensor network for sea ice monitoring exist. However, the problem of mobile sensors has been addressed by several authors, see e.g. Choi et al. (2010); Daescu et al. (2004); Majumdar et al. (2002); Palmer et al. (1998). This network, in our context unmanned (aerial) vehicles, should exploit the strengths of each sensor platform in the sensor placements and path planning. In ice management operations, this involves the determination of when, where, and which type of sensor platform is needed to achieve an uncertainty reduction of a region of interest. In this decision making, the sensor platform properties discussed in previous sections are important to consider in order to make the information gathering economically and practically feasible. With these attributes in mind, Table 2.3b indicates in which regions each sensor platform is feasible.

For an ice observer, the following requirements must be considered in the mobile sensor network problem formulation:

(i) Localization and classification of ice features.
(ii) Urgency of closeness to operation.
(iii) Ice drift velocity and its variability.
(iv) Time since surveillance.

Requirement (i) implies that a relatively big geographical region must be covered. Requirement (ii) states that as the ice comes closer to the operation, the desired level of information increases. To minimize the covered region, Requirement (iii) ensures that the ice drift is incorporated in the path planning, e.g., only the ice in upstream direction is of interest. Furthermore, the predicted changes in the ice drift is also important to incorporate in the path planning. The final requirement accounts for the modeling inaccuracies which can introduce discrepancies between the modeled and real world. These requirements should be aided by numerical models and estimation techniques.

## 2.4 Conclusions

An ice observer structure has been outlined where the important elements have been presented. The paper emphasizes the need for numerical models combined with estimation techniques in the forecasting of the ice environment. Furthermore, the possibility of using this combination in the path planning of mobile sensor networks has been motivated.

The usefulness of unmanned aerial vehicles as a sensor platform for ice monitoring has been argued. UAVs show flexibility with respect to coverage and resolution, which are key attributes for a sensor platform. Moreover, UAVs can be equipped with sensors that provide important information about the surrounding environment, including temperature, wind velocity, ice-floe distribution, ice velocity, and other ice parameters. Another important driver pushing the development and use of UAV is occupational safety and health.

# Chapter 3

# Monitoring Moving Objects Using Aerial Mobile Sensors

*We propose an optimization-based path planning framework for an aerial mobile sensor network. The purpose of the path planning is to monitor a set of moving surface objects. The algorithm provides collision-free mobile sensor trajectories that are feasible with respect to user-defined vehicle dynamics. The objective of the resulting optimal control problem is to minimize the uncertainty of the objects, represented as the trace of the augmented state and parameter estimation error covariance. The dynamic optimization problem is discretized into a large-scale nonlinear programming (NLP) problem using the direct transcription method known as simultaneous collocation. The optimization problem is solved with a receding horizon and both a field experiment and a numerical simulation illustrate the approach. The work in this chapter is published in Haugen et al. (2014b), which is based on Haugen et al. (2013a,b).*

## 3.1 Introduction

REMOTE sensing is useful for several different applications, including urban planning (Netzband et al., 2007), crop monitoring (M. S. Moran et al., 1997), polar remote sensing (Lubin et al., 2006), other environmental applications (Elachi et al., 2006), and maritime patrolling. Common sensor platforms in this regard are satellites and manned aerial vehicles, which in many cases provide the required accuracy and frequency of acquisition. For some demanding applications, finer resolution and higher frequency of acquisition are necessary requirements to enable a safe operation. One example is the monitoring of icebergs and hazardous ice features in ice management operations. In Haugen et al. (2011), the authors argued that unmanned aerial vehicles may become a cost-effective sensor platform for ice management operations.

Suppose we have a number of moving objects that we want to keep track of. At our disposal we have several aerial mobile sensors that are capable of remotely sensing the objects in question. We assume that each object has at least a mathematical description of its planar displacement dynamics, but that this description

has modeling uncertainties. The two main tasks we seek to answer are how to monitor these objects efficiently, and how to minimize the uncertainty of estimated future trajectories of the objects. Thus, we want to develop an autonomous remote sensing framework that provides object measurements for input to state and parameter estimation of the objects' dynamics.

The topic of object monitoring, also known as target tracking, has received much attention in literature. The main reason for this is because of its various possible application areas. As a consequence, there also exist many different approaches, ranging from a single sensor tracking a single object (Geiger, 2009), to using multiple mobile sensors for tracking multiple moving targets (Morbidi et al., 2013; Parker, 1999; Tang et al., 2005). Generally, we can classify contributions according to the number $n_m$ of sensors and $n_o$ objects being considered, denoted "$n_m$ to $n_o$". For the mobility of sensors, different models have been considered. The use of mass-spring-damper models for describing mobile sensors (Morbidi et al., 2013; Parker, 1999; Zhou et al., 2011) are less common than nonholonomic vehicle models with bounded turning radius (Geiger, 2009; Klesh et al., 2009; Quintero et al., 2010; Tang et al., 2005), also called *Dubins vehicle* or *Dubins paths*. The latter model is more popular due to its simple, but more realistic description of fixed-wing aircraft, wheeled ground vehicles, and torpedo-like underwater vehicles. The measuring capability of the sensors can generally be divided into either globally or locally supported footprint. Globally supported devices include measurements providing range, range-bearing, and bearing type of measurements, where the signal-to-noise ratio for instance can be proportional to the distance between the sensor and object being measured (Klesh et al., 2009; Morbidi et al., 2013; Zhou et al., 2011). Locally supported devices have a clear distinction for providing a measurement or not, like a camera with a limited field of view (Geiger, 2009; Parker, 1999; Quintero et al., 2010; Tang et al., 2005). Objects being tracked are described using a variety of dynamic models in literature. Common models include zero-velocity (Klesh et al., 2009; Rathinam et al., 2007; Savla et al., 2008), constant velocity (Geiger, 2009; Looker, 2008; Quintero et al., 2010), or linear dynamics (Morbidi et al., 2013). For the path planning algorithm, authors usually consider either resource allocation-based applications, where the objects are to be visited once or a predefined number of times, or information-driven applications that provide paths based on scalar functions representing information reward of visiting an object.

Geiger (2009) successfully carried out a field experiment of real-time trajectory planning of an unmanned aerial vehicle. The objective was to maximize observation time of a single object, moving or static, using direct collocation. Klesh et al. (2009) used a spatially motivated signal-to-noise ratio as a weighting of the measurement noise together with a Kalman filter in the path planning of a nonholonomic vehicle. The purpose was to observe a set of static objects with corrupted visibility or uncertain object location.

The multi-target tracking objective has also been approached using resource allocation, where the problem is formulated as a traveling salesperson problem with nonholonomic vehicle description. Savla et al. (2008) solves the minimum-time "1 to $n_o$" visitation path planning with static objects. The more general problem of minimum distance coverage of "$n_m$ to $n_o$" is solved in Rathinam et al. (2007), but with restrictions on the minimum distance between the static objects. The single

vehicle moving target traveling salesperson problem, where the objects move with constant velocities was solved by Looker (2008) with minimum distance Dubins paths.

Early work on the "$n_m$ to $n_o$" can be found in Parker (1999) where homogeneous mobile sensors with local measurement support tracked moving targets in a bounded and uncluttered region of interest. It was formulated as an optimization problem and the objective was to maximize observation time of the targets. Nonholonomic vehicle dynamics was not considered. In Tang et al. (2005), the "$n_m$ to $n_o$" was solved using a gradient-based approach with nonholonomic vehicles. The objective was to minimize the average time duration between consecutive observations of each target. All the above contributions considered a centralized and cooperative approach, with the exception of Tang et al. (ibid.), where decentralization by heuristic K-means clustering also was proposed. Recently, Morbidi et al. (2013) developed a gradient-based control scheme for the "$n_m$ to $n_o$" problem that minimized the targets' covariance matrix using different optimum experimental design criteria, such as the trace of the estimation error covariance matrix. In the approach, linear object dynamics is considered, with globally supported measurements. The sensor dynamics is unconstrained mass-spring-damper models without considering collision avoidance. The authors discuss both cooperative and non-cooperative approaches, and provide upper and lower bounds on the position covariance of the targets.

In Haugen et al. (2013a,b), cooperative autonomous monitoring of moving surface objects was accomplished by formulating and solving an optimal control problem for the "1 to $n_o$" problem. The problem minimized weighted traces of the objects' state estimation covariance matrices by determining a feasible path for a single mobile sensor. Herein, we extend Haugen et al. (2013a) to "$n_m$ to $n_o$" capability. Both a field experiment and a numerical simulation successfully demonstrate the approach. The framework supports multiple mobile sensors with collision-free trajectories. In addition, the objective function can take into consideration the possibility of reducing parameter uncertainties of the objects when performing the path planning. Locally supported measurement models are used. Both nonholonomic, mass-spring-damper dynamics, and more involved vehicle models are possible with the proposed framework.

### 3.1.1 Notation

An n-dimensional column vector of ones is denoted $1_{n\times 1}$. $I_n$ is the $n \times n$ identity matrix. A countable finite index set of positive natural numbers is defined as $\mathbb{I}_n := \{i \in \mathbb{N}^+ : i \leq n\}$. A block diagonal matrix of other matrices $X_{i\in\mathbb{I}_s} \in \mathbb{R}^{m_i\times n_i}$ is defined as $\text{bdiag}_{i\in\mathbb{I}_s}(X_i) := \bigoplus_{i\in\mathbb{I}_s} X_i$, where $\oplus$ is the direct sum. The vertically stacked matrix of other matrices $X_{i\in\mathbb{I}_s} \in \mathbb{R}^{m_i\times n}$ is denoted $\text{col}_{i\in\mathbb{I}_s}(X_i) := \text{bdiag}_{i\in\mathbb{I}_s}(X_i) \cdot (1_{s\times 1} \otimes I_n)$, where $\otimes$ is the Kronecker product. The diagonal of a column vector $x \in \mathbb{R}^n$ is the block diagonal of its scalar elements $x_i$, $\text{diag}(x) := \text{bdiag}_{i\in\mathbb{I}_n}(x_i)$. The space of non-zero $n$-dimensional real vectors is denoted $\mathbb{R}^n_{\neq 0}$. Define the set of positive definite real matrices as $\Pi_n := \{A \in \mathbb{R}^{n\times n} : \forall x \in \mathbb{R}^n_{\neq 0}, x^\mathsf{T} A x > 0\}$. The orientation space is defined by $\mathbb{S} := [-\pi, \pi)$. Define the $L^p$-normed metric space $M_p = (\mathbb{R}^n, \|\cdot\|_p)$. The corresponding open ball with origin

$\eta \in \mathbb{R}^n$ is $\mathcal{B}_p(\eta; r) := \{x \in M_p : \| \cdot \|_p < r\}$. The first moment of a random vector $x$ is denoted by the expectation operator $\mathrm{E}(x)$. The covariance matrix of two random vectors $x$ and $y$ is defined as $\mathrm{cov}(x, y) := \mathrm{E}[(x - \mathrm{E}(x))(y - \mathrm{E}(y))^\mathsf{T}]$. Non-negative real numbers are defined by the set $\mathbb{R}_{\geq 0}$. A zero-mean continuous-time white noise process $w(t)$ of dimension $n$ has the properties $\mathrm{E}(w) = 0$ and $\mathrm{cov}(w(t), w(\tau)) = Q(t)\delta(t - \tau)$, where $Q : \mathbb{R}_{\geq 0} \to \Pi_n$ is the deterministic spectral density and $\delta(t)$ is the dirac delta function. The above mentioned properties of $w(t)$ are written compactly as $w(t) \sim (0, Q(t))$.

## 3.2 Problem Description

We are interested in using multiple aerial mobile sensor to monitor multiple moving objects. We proceed by defining an illustrating example that serves as a simplified exposition of the problem description. Once the illustrating example has been defined, we give an overview of the system components needed to solve the problem. This includes a quantified description of the uncertainties of the objects' states and parameters. We will revisit the illustrating example when all the relevant components of the monitoring systems have been defined and further generalized.

### 3.2.1 Illustrating Example

Suppose that we have $n_o$ objects (e.g. icebergs) moving with almost constant velocity that we want to monitor. We assume that we have estimated initial positions of the objects at time $t_0$, but that the objects' states and parameters are uncertain. In particular, the accurate position and drift velocity of each object are not known. A mobile aerial sensor is able to sense the objects using for instance a camera with a limited field of view (FOV). Since the FOV is limited, the objects cannot necessarily be observed simultaneously. The objective is thus to steer the mobile sensor such that all the objects' states and parameters can be estimated.

Let {ned} denote a right-handed stationary reference frame whose axes denote north, east, and down coordinates, respectively. The dynamics of the objects can be described $\forall o \in \mathbb{I}_{n_o}$ as

$$\dot{N}_o(t) = v_{N,o} + w_{N,o}(t), \tag{3.1a}$$

$$\dot{E}_o(t) = v_{E,o} + w_{E,o}(t), \tag{3.1b}$$

where $\chi_o := \mathrm{col}(N_o, E_o)$ is object $o$'s north and east coordinates, the uncertain velocity parameter vector is $\rho_o := \mathrm{col}(v_{N,o}, v_{E,o})$, and $\mathrm{col}(w_{N,o}(t), w_{E,o}(t)) =: w_o^\chi(t) \sim (0, Q_o(t))$ is process noise.

The sensor dynamics is intended for path-planning purposes and need not be a high-fidelity model. It is, however, important that the planned paths are feasible with respect to maneuverability constraints of the mobile sensors. We consider a constant-altitude kinematic model with the bank angle $u_\theta(t)$ as control input. Let $x_N(t)$ and $x_E(t)$ denote the north and east position of the sensor, and $\psi(t) \in \mathbb{S}$ the right-hand screw z-axis rotation of a body-fixed reference frame {b} relative to

{ned}. The dynamics is

$$\dot{x}_N(t) = V_a \cos(\psi), \tag{3.2a}$$
$$\dot{x}_E(t) = V_a \sin(\psi), \tag{3.2b}$$
$$\dot{\psi}(t) = \frac{g}{V_a} \tan(u_\theta(t)), \tag{3.2c}$$

where $V_a$ is the positive airspeed and $g$ is the standard gravity. We constrain the commanded bank angle, so that the resulting state trajectories are sufficiently conservative and feasible. For all $t \in \mathbb{R}_{\geq 0}$ and $u_{\theta,L}, u_{\theta,H} \in \mathbb{S}$, let

$$u_{\theta,L} \leq u_\theta(t) \leq u_{\theta,H}. \tag{3.2d}$$

We also restrict the planar position of the mobile sensor. In particular, we define a closed convex polygon

$$\mathcal{K} := \{y \in \mathbb{R}^2 : m \geq 3, A \in \mathbb{R}^{m\times 2}, b \in \mathbb{R}^m, Ay \leq b\},$$

so that $x(t) := \text{col}(x_N(t), x_E(t), \psi(t))$ is constrained for all $t \in \mathbb{R}_{\geq 0}$ by

$$x(t) \in \mathcal{K} \times \mathbb{S} =: \mathbb{X}. \tag{3.2e}$$

**Problem 3.1.** Perform state and parameter estimation of the objects $o \in \mathbb{I}_3$ of (3.1) for all $t \in [t_0, T]$, where $T$ is the final time of interest. This should be accomplished by determining a feasible input $u_\theta(t)$ for the mobile sensor (3.2) to obtain intervals of measurement of all the objects.

### 3.2.2 System Overview

We consider a monitoring system consisting of three main components:

**RPAS:** Remotely piloted aircraft system that acts as a mobile sensor network. It provides measurements of the objects.

**Observer:** Processes raw measurements and other inputs to return the most likely model state and parameters of the mobile sensors and the objects.

**Path Planner:** Generates guidance inputs of where and when we want the mobile sensors to obtain measurements of the objects.

The monitoring system is governed by a supervision component that decides the configuration of the containing components. This includes the size of the mobile sensor network, which objects to monitor, specific mathematical descriptions, and other relevant considerations. The monitoring system is also influenced by the environment through both the actual objects being monitored, environmental disturbances, as well as future forecasts. The system under consideration is shown in Figure 3.1. The main focus of this manuscript is to develop an optimization-based *Path-Planner* component.

#### Mobile Sensor Dynamics

We assume that first-order nonlinear ordinary differential equations (ODEs) with state and input constraints describe the vehicle dynamics with sufficient fidelity.

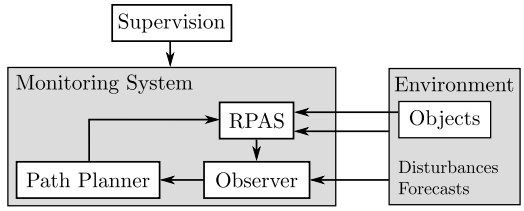


**Figure 3.1** Components of the system under consideration.

Let $n_m$ be the number of mobile sensors and define the index set $\mathbb{M} := \mathbb{I}_{n_m}$. For all $m \in \mathbb{M}$ and $t \geq t_0 \geq 0$ we have that $x_m(t) \in \mathbb{R}^{n_{x_m}}$ denote the state vector, $u_m(t) \in \mathbb{R}^{n_{u_m}}$ the control input, and $\vartheta_m \in \mathbb{R}^{n_{\vartheta_m}}$ a vector of constant parameters for mobile sensor $m$. Then, $\forall m \in \mathbb{M}$ the mobile sensor models are described by the deterministic systems

$$\dot{x}_m(t) = f_m(t, x_m(t), u_m(t), \vartheta_m), \tag{3.3a}$$
$$x_m(t_0) = x_{m,0}, \tag{3.3b}$$
$$x_m(t) \in \mathbb{X}_m \subseteq \mathbb{R}^{n_{x_m}}, \tag{3.3c}$$
$$u_m(t) \in \mathbb{U}_m \subseteq \mathbb{R}^{n_{u_m}}, \tag{3.3d}$$

where $f_m : \mathbb{R}_{\geq 0} \times \mathbb{R}^{n_{x_m}} \times \mathbb{R}^{n_{u_m}} \times \mathbb{R}^{n_{\vartheta_m}} \to \mathbb{R}^{n_{x_m}}$ is a sufficiently smooth function, and both $\mathbb{X}_m$ and $\mathbb{U}_m$ are convex sets.

### Object Dynamics

Let $n_o$ be the number of objects and define the index set $\mathbb{O} := \mathbb{I}_{n_o}$. For all $o \in \mathbb{O}$ and $t \geq t_0$ we have that $\chi_o(t) \in \mathbb{R}^{n_{\chi_o}}$ is the state vector, $w_o^\chi(t) \in \mathbb{R}^{n_{\chi_o}} \sim (0, Q_o^\chi(t))$ is the state process noise, and $p_o \in \mathbb{R}^{n_{p_o}}$ is a vector of constant or slowly-varying parameters. The dynamics of the objects can be described by first-order stochastic nonlinear ODEs as

$$\dot{\chi}_o(t) = f_o^\chi(t, \chi_o(t), w_o^\chi(t), p_o), \tag{3.4a}$$
$$\chi_o(t_0) = \chi_{o,0}, \tag{3.4b}$$

where $f_o^\chi : \mathbb{R}_{\geq 0} \times \mathbb{R}^{n_{\chi_o}} \times \mathbb{R}^{n_{p_o}} \to \mathbb{R}^{n_{\chi_o}}$ is a sufficiently smooth function.

We separate the parameter vector into two vectors $\rho_o$ and $\sigma_o$ such that $p_o := \mathrm{col}(\rho_o, \sigma_o)$, where $\rho_o$ is regarded as uncertain with parameter process noise $w_o^\rho(t) \in \mathbb{R}^{n_{\rho_o}} \sim (0, Q_o^\rho(t))$. The purpose of splitting the vector is for estimating the uncertain parameters. Define the augmented vector $z_o := \mathrm{col}(\chi_o, \rho_o)$, so that the augmented state dynamics is

$$\begin{aligned}\dot{z}_o(t) &= \mathrm{col}(f_o^\chi(t, \chi_o(t), w_o^\chi(t), p_o), w_o^\rho(t)) \\ &=: f_o(t, \chi_o(t), w_o(t), p_o),\end{aligned} \tag{3.5a}$$
$$z_o(t_0) = \mathrm{col}(\chi_{o,0}, \rho_{o,0}), \tag{3.5b}$$

where $w_o(t) = \mathrm{col}(w_o^\chi(t), w_o^\rho(t)) \sim (0, Q_o(t))$ and $Q_o(t) := \mathrm{bdiag}(Q_o^\chi(t), Q_o^\rho(t))$.

When a mobile sensor is sufficiently close to an object, it obtains a measurement of it. This output is for each object $o \in \mathbb{O}$ and sensor $m \in \mathbb{M}$ defined as

$$y_{o,m}(t) = h_{o,m}(t, \chi_o(t), v_{o,m}(t)), \tag{3.5c}$$

where $\chi_o(t)$ is the object state vector, $v_{o,m}(t) \in \mathbb{R}^{n_{y_{o,m}}} \sim (0, R_{o,m}(t))$ is measurement noise for sensor $m$ on object $o$, and $h_{o,m} : \mathbb{R}_{\geq 0} \times \mathbb{R}^{n_{\chi_o}} \times \mathbb{R}^{n_{y_{o,m}}} \to \mathbb{R}^{n_{y_{o,m}}}$ is a sufficiently smooth function. We assume that the mobile sensors collectively are able to measure each object in such a way that some sort of observability property of the object is satisfied. This property involves obtaining sufficiently informative measurements to be able to monitor the objects.

**Remark 3.1.** Knowing whether the objects' states and parameters are observable or not is important for the usefulness of the monitoring system. Observability for nonlinear systems is complicated in general. To illustrate the observability of a single object, we consider the linear time-varying and noise-free system

$$\dot{x} = A(t)x + B(t)u, \tag{3.6a}$$
$$y = C(t)x. \tag{3.6b}$$

It is stated in C.-T. Chen (1999, Th. 6.O11) that (3.6) is observable at time $t_0$ if and only if there exist $t_1 > t_0$ such that the matrix

$$W_o(t_0, t_1) = \int_{t_0}^{t_1} \Phi^{\mathsf{T}}(\tau, t_0) C^{\mathsf{T}}(\tau) C(\tau) \Phi(\tau, t_0)\, d\tau, \tag{3.7}$$

where $\Phi(t, \tau)$ is the state transition matrix of $\dot{x} = A(t)x$, is nonsingular. In our monitoring system, the object will either be measured or not, that is, $C(t)$ may switch between a constant matrix and the zero-matrix at regular intervals. Consequently, the above integral consists of piecewise nonzero interval contributions, where

$$W_\ell(t_{\ell,0}, t_{\ell,1}) = \int_{t_{\ell,0}}^{t_{\ell,1}} \Phi^{\mathsf{T}}(\tau, t_{\ell,0}) C^{\mathsf{T}}(\tau) C(\tau) \Phi(\tau, t_{\ell,0})\, d\tau \tag{3.8}$$

is the $\ell$th contribution with $t_{\ell,1} > t_{\ell,0} \geq t_0$. The object's states are observable if there exist a number $\ell_t$ of intervals such that

$$W_o(t_0, t_{\ell_t,1}) = \sum_{\ell=1}^{\ell_t} W_\ell(t_{\ell,0}, t_{\ell,1}) \tag{3.9}$$

is nonsingular. For systems with time-invariant $A$-matrix, each interval contribution is structurally identical. This means that if $W_\ell$ is singular, then the system is unobservable because $W_o$ is singular for all $t$. In case of observability, measurement windows will gradually improve the estimates.

### Object Uncertainty Measure

The augmented states of the objects are random variables and may be characterized by quantitative measures, such as the mean and covariance descriptions. More

specifically, $\forall o \in \mathbb{O}$ we define $\mathrm{E}(\chi_o(t)) = \hat{\chi}_o(t)$ as the state estimate of $\chi_o(t)$ and $E(\rho_o) = \hat{\rho}_o(t)$ as the parameter estimate of $\rho_o$. For each $o \in \mathbb{O}$, we define the state and parameter estimation errors as

$$\tilde{\chi}_o(t) = \chi_o(t) - \hat{\chi}_o(t), \tag{3.10a}$$

$$\tilde{\rho}_o(t) = \rho_o - \hat{\rho}_o(t), \tag{3.10b}$$

which combined give the augmented estimation error vector

$$\tilde{z}_o(t) = \mathrm{col}(\tilde{\chi}_o(t), \tilde{\rho}_o(t)), \tag{3.10c}$$

and the estimation error covariance

$$P_o(t) = \mathrm{cov}(\tilde{z}_o(t), \tilde{z}_o(t)). \tag{3.10d}$$

**Problem Statement**

The objective is to minimize the uncertainties of the objects' states and parameters to allow probable estimates of the objects future state trajectories. The task includes generating feasible collision-free trajectories for the mobile sensors. The problem will be approached by formulating and efficiently solving a receding horizon optimization problem that mathematically describes the objective. A sub-task is to find a model for the mobile sensors' influence on the objects' covariance dynamics.

## 3.3 Measurement Models

For each $m \in \mathbb{M}$, define the two-dimensional Cartesian coordinates of sensor $m$ as $\varrho_m(t) \in \mathbb{R}^2$. Further, $\forall o \in \mathbb{O}$ we have the object positions $q_o(t) \in \mathbb{R}^2$. We assume that the positions of each object $o$ will remain within a subset $\mathbb{D}_o$ of the combined configuration spaces of the sensors. We also assume that the planar position is part of the dynamics of both the sensors and the objects, that is, for each $m \in \mathbb{M}$ and $o \in \mathbb{O}$, knowledge about $x_m$ and $\chi_o$ implies knowledge about $\varrho_m$ and $q_o$. Some low-level logic is assumed to properly associate measurements to the respective objects, for instance through object shape identification.

We assume that the objects are located in such a way that the mobile sensors cannot necessarily measure all the objects simultaneously. Each mobile sensor has a limited FOV. This capability has to be properly described using a so-called *sampling function* (Tricaud et al., 2012). We propose to use sampling functions that depend on the coordinates of the mobile sensors to reflect how the output vectors are sampled by the sensors. In this context, the output vector is a vector function that depends on the state vector of an object being monitored. A mobile sensor may consist of a set of measuring devices that samples the states in different ways. These devices may not have the same measuring capabilities, so in order to keep the representation general, we assume that each element of the output vector $y(t) \in \mathbb{R}^{n_y}$ is shaped with its own scalar sampling function.

The characteristics of the sampling functions are different depending on where they are used. We take a realistic model as a starting point and define two different types of sampling functions, which will be used later in the manuscript. More

precisely, we distinguish between non-smooth and smooth sampling functions. The non-smooth sampling function is a more accurate description of a FOV-type of measuring device, and is useful in the *Observer*. The non-smooth property is practical in the chosen implementation of the *Path Planner*, so a smooth approximation also needs to be defined.

Let the family of scalar sampling functions be defined as $\mathbb{W}$ and let $\mathbb{B}$ be the codomain of this family. For all $i \in \mathbb{I}_{n_y}$ let $w_i : \mathbb{R}_{\geq 0} \times \mathbb{R}^2 \times \mathbb{R}^2 \times \mathbb{S} \to \mathbb{B}$ and define a diagonal matrix function $W(t, \varrho(t), q(t), \psi(t)) = \operatorname{bdiag}_{i \in \mathbb{I}_{n_y}}(w_i)$ with codomain $\in \mathbb{B}^{n_y \times n_y}$. The shaped measurement vector is therefore defined as

$$y_w(t) = W\left(t, \varrho(t), q(t), \psi(t)\right) y(t). \tag{3.11}$$

A shaped measurement vector captures the case where a measuring device has compact support, for instance an image obtained from an optical device with a limited field of view.

### 3.3.1 Non-Smooth Sampling Function

The purpose of this model is to simulate that the measuring device has a field of view, in which it is able to obtain measurements. This includes for instance the cases of roll and pitch stabilized downward-looking optical devices and spectrometers.

Let $\Delta_{x_i} > 0$, $i \in \{1, 2\}$ and define $\Delta_x := \operatorname{col}(\Delta_{x_1}, \Delta_{x_2})$. We define the two-dimensional FOV metric as a weighted infinity norm

$$\|x\|_\infty^{\Delta_x} := \max\left(\frac{|x_1|}{\Delta_{x_1}}, \frac{|x_2|}{\Delta_{x_2}}\right). \tag{3.12}$$

Suppose the position $\varrho(t)$ of a sensor is the origin of a body-fixed Cartesian coordinate system $\{b\}$. Furthermore, suppose the orientation $\psi(t)$ of $\{b\}$ is defined relative some stationary reference frame $\{i\}$ following the right-hand rule. Let $\mathbb{B}_{\mathcal{C}^{-1}} := \{0, 1\}$ be the codomain of a binary sampling function $w_{\mathcal{C}^{-1}} : \mathbb{R}_{\geq 0} \times \mathbb{R}^2 \times \mathbb{R}^2 \times \mathbb{S} \to \mathbb{B}_{\mathcal{C}^{-1}}$, such that the codomain is nonzero only if a coordinate point $q(t) \in \mathbb{R}^2$ of an object is within the convex set formed by a FOV metric. The two-dimensional rotation matrix is

$$R(\psi) = \begin{bmatrix} \cos\psi & -\sin\psi \\ \sin\psi & \cos\psi \end{bmatrix}. \tag{3.13}$$

We can write the binary sampling function as

$$w_{\mathcal{C}^{-1}}(t, \varrho, q, \psi) := \begin{cases} 1, \left\|R^{\mathsf{T}}(\psi)(q - \varrho)\right\|_\infty^{\Delta_x} < 1 & \text{(3.14a)} \\ 0, \text{ otherwise.} & \text{(3.14b)} \end{cases}$$

Figure 3.2 graphically illustrates the behavior of the binary sampling function. We see that $\Delta_{x_1}$ and $\Delta_{x_2}$ quantify respectively the field of view in $x$ and $y$ direction of the body-fixed reference frame.

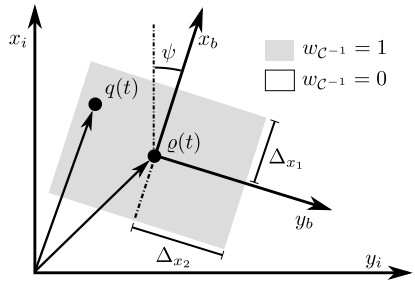


**Figure 3.2** The non-smooth sampling function is one for $q(t)$ inside the box and zero otherwise. $x_i$ and $y_i$ denote the axes of the stationary reference frame.

### 3.3.2 Smooth Sampling Function

In some cases, for instance in an optimization problem, a continuously defined sampling function with positive codomain may be preferred as an approximation to some non-smooth sampling function. Let $\mathbb{B}_{\mathcal{C}^\infty} := \{w \in \mathbb{R} : 0 \leq w \leq 1\}$. Define a smooth sampling function $w_{\mathcal{C}^\infty}(t, \varrho, q, \psi) : \mathbb{R}_{\geq 0} \times \mathbb{R}^2 \times \mathbb{R}^2 \times \mathbb{S} \to \mathbb{B}_{\mathcal{C}^\infty}$, which is 1 if $\varrho = q$ and less than 1 otherwise.

**Example 3.1.** Let $K_{i \in \mathbb{I}_n} \in \Pi_2$, and $\tilde{q} = q - \varrho$. A possible smooth sampling function is the linear combination of $n$ two-dimensional Gaussian functions, for instance

$$w_{\mathcal{C}^\infty}(t, \varrho, q, \psi) := \sum_{i \in \mathbb{I}_n} \lambda_i e^{-\tilde{q}^\mathsf{T} R(\psi) K_i R^\mathsf{T}(\psi) \tilde{q}}, \tag{3.15}$$

where $\sum_{i \in \mathbb{I}_n} \lambda_i = 1, \lambda_i \geq 0$. The purpose of having a combination of exponential functions is that the sampling surface can be shaped in such a way that it approximates a non-smooth sampling surface while still being smooth and having a nonzero image. Figure 3.3 displays an example of such a sampling surface.

## 3.4 Path Planner

### 3.4.1 Adapted Covariance Dynamics

The estimation error covariance (3.10d) of the objects quantify the uncertainties of the state vector and the uncertain parameter vector. We want to reduce these uncertainties by measuring the objects using the mobile sensors. The covariance response of the objects can be described by the corresponding equation in the continuous-time extended Kalman filter (Simon, 2006). We present in the following a version with both time-varying process noise and measurement matrices.

For each object $o \in \mathbb{O}$, the system equations defined by (3.5a)-(3.5b) are linearized along the predicted trajectories of the objects, with both measurement and process noise set to zero. Let $\hat{\chi}_o(t)$ be the solution to the initial value problem (IVP) (Iserles, 1996) (3.4), with $\chi_o(t_0) = \hat{\chi}_{o,0}$ and $p_o = \hat{p}_{o,0}$, which are the best estimates at time $t_0$. Then, the predicted trajectory is $\hat{\chi}_o(t)$ and for each $(o, m) \in \mathbb{O} \times \mathbb{M}$, we

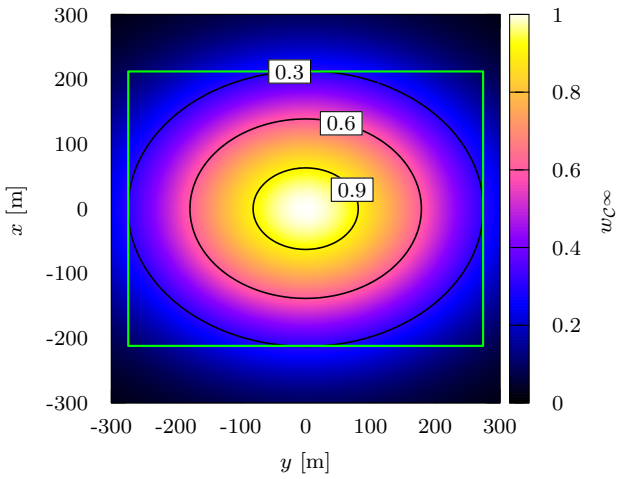


**Figure 3.3** A smooth sampling function. The axes are $\text{col}(x, y) = \tilde{q} = (q - \varrho)$, which are the relative planar coordinates between an object and a sensor. The green box is the non-smooth sampling function being approximated.

define the following partial derivatives along the augmented trajectory as

$$A_o(t) = \frac{\partial f_o}{\partial z_o}(t, \hat{\chi}_o(t), 0, \hat{p}_o), \tag{3.16a}$$

$$L_o(t) = \frac{\partial f_o}{\partial w_o}(t, \hat{\chi}_o(t), 0, \hat{p}_o), \tag{3.16b}$$

$$C_{o,m}(t) = \frac{\partial h_{o,m}}{\partial \chi_o}(t, \hat{\chi}_o(t), 0), \tag{3.16c}$$

$$M_{o,m}(t) = \frac{\partial h_{o,m}}{\partial v_{o,m}}(t, \hat{\chi}_o(t), 0). \tag{3.16d}$$

To model the mobile sensors' influence on the object covariance dynamics we make use of the measurement models presented in Section 3.3. More specifically, we use the smooth sampling function to define a diagonal matrix function for each sensor on each object $W_{o,m} : \mathbb{R}_{\geq 0} \times \mathbb{R}^2 \times \mathbb{R}^2 \times \mathbb{S} \to \mathbb{B}_{\mathcal{C}^\infty}^{n_{y_{o,m}} \times n_{y_{o,m}}}$, where the diagonal elements are smooth sampling functions. We get $\forall (o, m) \in \mathbb{O} \times \mathbb{M}$

$$W_{o,m}(t, \varrho_m, q_o, \psi_m) = \text{bdiag}_{i \in \mathbb{I}_{n_{y_{o,m}}}}(w_{\mathcal{C}^\infty, o, m, i}). \tag{3.17}$$

The motivation for using smooth sampling functions is that the chosen solver needs smoothness and curvature to find a solution to the optimization problem. More specifically, the solver needs an objective function and constraints that are at least twice continuously differentiable. The local solver also needs curvature in the objective to obtain search directions. Hence, non-smooth sampling functions need to be approximated using smooth sampling function. The proposed shaping can be tuned in such a way that the codomain approximates the behavior of a field of view with local support. A mobile sensor will significantly affect the covariance

dynamics of the object if it is sufficiently close to it. The closer a mobile sensor is to the object, the bigger stabilizing impact it will have on the object's covariance.

We use the matrix sampling functions to shape the measurement operators $C_{o,m}(t)$ along the predicted trajectories of the objects. So for each $(o, m) \in \mathbb{O} \times \mathbb{M}$ we get

$$C^w_{o,m}(t) = W_{o,m}(t, \varrho_m, \hat{q}_o, \psi_m) C_{o,m}(t). \tag{3.18}$$

When a mobile sensor is sufficiently far away from the object, the shaping of the measurement should be so small that it in practice does not affect the covariance; the mobile sensor is not able to measure the object. For the sensors to still be attracted to distant objects, we propose to manipulate the process noise matrices $Q_o(t)$. We use a non-vanishing sampling function to reduce the process noise when a sensor is close to an object. In this way, the mobile sensor's movement will always affect the covariance of the objects, but only slightly. Let $\varrho := \mathrm{col}_{m\in\mathbb{M}}(\varrho_m)$ and $\psi := \mathrm{col}_{m\in\mathbb{M}}(\psi_m)$. Define for all objects $o \in \mathbb{O}$

$$Q^w_o(t, \varrho, \hat{q}_o, \psi) = Q_o(t) \left(1 - \frac{1}{n_m} \sum_{m\in\mathbb{M}} w_{\mathcal{C}^\infty}(\varrho_m, \hat{q}_o, \psi_m)\right). \tag{3.19}$$

Define the shorthand expressions

$$\overline{Q}^w_o(t, \varrho, \hat{q}_o, \psi) = L_o(t) Q^w_o(t, \varrho, \hat{q}_o, \psi) L^\mathsf{T}_o(t), \tag{3.20a}$$

$$\overline{R}_{o,m}(t) = M_{o,m}(t) R_{o,m}(t) M^\mathsf{T}_{o,m}(t). \tag{3.20b}$$

Now, we have the definitions in place to formulate the adapted covariance dynamics intended for the optimization problem. For simplicity, we omit the arguments of the expressions, and so for each $o \in \mathbb{O}$ we get the differential Riccati equation of the extended Kalman filter:

$$\dot{P}_o(t) = A_o P_o + P_o A^\mathsf{T}_o + \overline{Q}^w_o - \sum_{m\in\mathbb{M}} P_o C^{w\,\mathsf{T}}_{o,m} \overline{R}^{-1}_{o,m} C^w_{o,m} P_o, \tag{3.21a}$$

$$P_o(t_0) = P_{o,0}. \tag{3.21b}$$

### 3.4.2 Collision Avoidance

The mobile sensor trajectories must be constructed so that the sensors do not collide with each other. Let for each $m \in \mathbb{M}$ the vector $\eta_m(t) \in \mathbb{R}^3$ define the body-fixed origin of sensor $m$ relative the stationary frame $\{i\}$. Each sensor is enclosed by its own open ball $\mathcal{B}_2(\eta_m; r_m) \subset \mathbb{R}^3$ that no other sensor should enter. We formulate the collision avoidance as constraints between each pair of mobile sensors. These constraints can be found by defining a complete graph (Ray, 2013). Each vertex represents a mobile sensor and each edge $(i, j) \in E$ is assigned an orientation such that sensor $i$ has a larger exclusion ball than sensor $j$, that is $r_i \geq r_j$. Let $G = (\mathbb{M}, E)$ be the described directed graph. Collision avoidance is obtained if $\forall t \in \mathbb{R}_{\geq 0}$, and for each $(i, j) \in E$

$$\eta_j(t) \notin \mathcal{B}_2(\eta_i(t); r_i). \tag{3.22}$$

A similar approach may be used to avoid other aerial objects or to stay away from surface installations. Non-differentiable convex exclusion regions such as polytopes are possible, see Patel et al. (2011).

### 3.4.3 Dynamic Optimization Problem

The object monitoring can be formulated as a Bolza-type optimal control problem (OCP) (Biegler, 2010). Let $t_0, t_f \in \mathbb{R}_{\geq 0}$ respectively denote the start and the end of the optimization horizon. The decision variables are $\forall m \in \mathbb{M}$ the control inputs $u_m(t)$. Define $u(t) := \mathrm{col}_{m\in\mathbb{M}}(u_m(t))$. Let $P(t) := \mathrm{bdiag}_{o\in\mathbb{O}}(P_o(t))$, $\Gamma(t) := \mathrm{bdiag}_{m\in\mathbb{M}}(\Gamma_m(t))$, and $\Xi(t) := \mathrm{bdiag}_{m\in\mathbb{M}}(\Xi_m(t))$, where $\Gamma_m(t) \in \Pi_{n_{u_m}}$ and $\Xi_m(t) \in \Pi_{n_{u_m}}$ are time-varying design variables.

We define the Lagrange term as

$$\Phi_L(t,u) = \int_{t_0}^{t_f} \mathrm{tr}(P(t)\,\mathrm{diag}(v^L(t))) + \frac{du}{dt}^{\mathsf{T}} \Gamma(t) \frac{du}{dt} + u^{\mathsf{T}}\Xi(t)u\,dt, \tag{3.23a}$$

where $v^L(t) := \mathrm{col}_{o\in\mathbb{O}}(v_o^L(t))$ is a vector function to be designed.

The Mayer term is

$$\Phi_M(t_f) = \mathrm{tr}(P(t_f)\,\mathrm{diag}(v^M)), \tag{3.23b}$$

where $v^M := \mathrm{col}_{o\in\mathbb{O}}(v_o^M)$ is a design vector.

The resulting optimization problem is to minimize (3.23) constrained by the mobile sensor network, its collision avoidance, and the objects' covariance dynamics, that is, $\forall t \in [t_0, t_f]$, $\forall (i,j) \in E, \forall o \in \mathbb{O}, \forall m \in \mathbb{M}$:

$$\min_{u} \quad \Phi_L(t,u) + \Phi_M(t_f) \tag{3.24a}$$

$$\text{s. t.} \quad (3.3), (3.22), (3.21). \tag{3.24b}$$

The solution to (3.24) provides $\forall m \in \mathbb{M}$ the optimal input vectors $u_m^\star(t) \in \mathbb{U}_m$ in the interval $t \in [t_0, t_f]$. Given the variables $u_m^\star$, $\hat{x}_{m,0}$, and $\hat{\vartheta}_m$ we can $\forall m \in \mathbb{M}$ solve the IVP formed by (3.3a)-(3.3b) over the optimization horizon. This results in optimal mobile sensor state trajectories, denoted for each $m \in \mathbb{M}$ as

$$x_m^\star(t) \in \mathbb{X}_m,\ t \in [t_0, t_f]. \tag{3.25}$$

Equation (3.25) serves as guidance input to path-maneuvering controllers for the mobile sensors.

### 3.4.4 Receding Horizon

Suppose we want to monitor the objects in the time interval $\mathbb{T} := [t_0, T]$. If $T$ is sufficiently large, the optimization problem (3.24) needs to be solved using a receding horizon. There are several factors that motivate this design decision:

(i) The optimization problem may become computationally intractable due to the problem size.

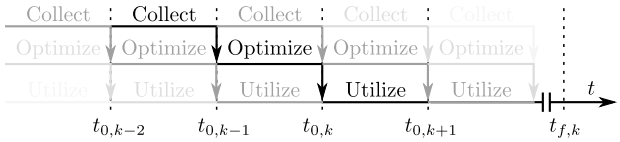


**Figure 3.4** The monitoring system consists of a three-step procedure of collecting, optimizing, and utilizing.

(ii) There are modeling inaccuracies, so the predicted object trajectories may drift away from the true trajectories.

(iii) The ambient conditions change.

We solve the optimization problem with receding horizon, so that the formulation can take into consideration updated information to improve the monitoring performance. We utilize a time interval of the optimized control input. Let $k_t \in \mathbb{N}_1$ be the number of optimization intervals and $\mathbb{T}_k := [t_{0,k}, t_{f,k}]$ be the optimization interval for the $k$th iteration. The desired monitoring time interval is covered by the receding horizons: $\mathbb{T} \subseteq \bigcup_{k \in \mathbb{I}_{k_t}} \mathbb{T}_k$. We assume that the end time $t_{e,k}$ of the utilization time interval is less than the optimization horizon, so for horizon $k$ we have $t_{0,k} < t_{e,k} < t_{f,k}$. The start of the next optimization horizon is therefore equal to the utilization time of the preceding iteration: $t_{0,k+1} \equiv t_{e,k}$.

Consider the $k$th iteration of the monitoring process. We divide it into a three-step procedure of collecting, optimizing, and utilizing. The first step, which is performed by the *Observer*, involves collecting measurements of the objects' and sensors' states. At time $t_{0,k-1}$ the collected information so far is used to perform state and parameter estimation. This involves predicting the future state of the objects and sensors at time $t_{0,k}$. The next step is to optimize by solving (3.24) to obtain the desired paths (3.25). This is accomplished by the *Path Planner*. The optimized paths should be readily available by the time $t_{0,k}$, since they at this time instant should be utilized by the remotely piloted aircraft system (RPAS), which is the final step.

The three steps of the procedure execute concurrently with earlier and later time steps: when the monitoring system is optimizing for iteration $k$, it is collecting for iteration $k+1$, and utilizing iteration $k-1$. Figure 3.4 illustrates the three-step procedure.

In the first few intervals we do as follows. Let the first interval be $k = 1$, so that the monitoring starts at $t_{0,0}$, cf. Figure 3.4. We provide a priori defined paths that we make sure are feasible with respect to the admissible region as well as collision avoidance. These offline defined paths are considered as substitute for the output of the optimization phase from iteration $k = 0$. The first optimized path will be utilized from $t_{0,1}$, but is calculated on the basis of offline collected data $t < t_{0,0}$. In that regard, the monitoring system is fully operative from $t_{0,1}$, but the effect of the optimized paths in the actual collected data will not be reflected in the path planning before $t_{0,2}$.

**Remark 3.2.** In the above description we have indicated that the collection ends at $t_{0,k-1}$. This choice is only made to simplify the presentation of the procedure. In

practice the time instant going from collection to optimization is only governed by the maximal optimization time $T_p$. The collection should therefore end at $t_{0,k} - T_p$.

During a continuous monitoring operation the set of objects may change over time. Some objects may leave the region of interest, while new objects may appear. Inclusion and removal of objects in the optimization are straightforward and can be done between optimization intervals.

## 3.5 Observer

As mention previously, the purpose of the *Observer* is to process data to provide state and parameter estimates. For iteration $k$, the collection stops at $t_{0,k-1}$, but the optimization problem (3.24) needs initial conditions at $t_{0,k}$. Hence, the *Observer* needs to perform a prediction from $t_{0,k-1}$ to $t_{0,k}$. To facilitate reasonable covariance estimates for the objects at $t_{0,k}$, state trajectories of all the objects and sensors are required to solve the expected closed-loop covariance response of (3.21).

**Criterion 3.1.** *Given the collected measurements for $t \in [t_{0,k-2}, t_{0,k-1}]$, the* Observer *component must provide the following estimates for iteration $k$, $\forall m \in \mathbb{M}, \forall o \in \mathbb{O}$*

$$x_m(t_{0,k-1}) = \hat{x}_m(t_{0,k-1}), \qquad \vartheta_m = \hat{\vartheta}_m(t_{0,k-1}), \tag{3.26a}$$

$$\chi_o(t_{0,k-1}) = \hat{\chi}_o(t_{0,k-1}), \qquad \rho_o = \hat{\rho}_o(t_{0,k-1}), \tag{3.26b}$$

$$P_o(t_{0,k-1}) = \hat{P}_o(t_{0,k-1}). \tag{3.26c}$$

This leaves flexibility in terms of the choice of observer(s) used in the monitoring system. For instance, both hybrid extended Kalman filters (Simon, 2006, Section 13.2.2) and moving horizon estimators satisfy Criterion 3.1.

**Criterion 3.2.** *The solution to the noise-free IVP in* (3.4) *$\forall o \in \mathbb{O}$ for $t \in [t_{0,k-1}, t_{0,k}] =: \mathbb{T}_{k-1}^k$, given the initial conditions from Criterion 3.1, is $\hat{\chi}_{o,k}(t)$. The expected closed-loop trajectory for each mobile sensor $m \in \mathbb{M}$ given the above initial conditions is denoted $\hat{x}_{m,k}^\star(t)$. Then, solving* (3.21) *in $t \in \mathbb{T}_{k-1}^k$ for each $o \in \mathbb{O}$ and all $m \in \mathbb{M}$ given $\hat{\chi}_{o,k}(t)$ and $\hat{x}_{m,k}^\star(t)$, results in the predicted covariance response $\hat{P}_{o,k}(t)$, which is valid for $t \in \mathbb{T}_{k-1}^k$.*

Criterion 3.2 provides the *Path Planner* with the required initial conditions $\forall m \in \mathbb{M}, \forall o \in \mathbb{O}$:

$$x_m(t_{0,k}) = \hat{x}_{m,k}^\star(t_{0,k}), \qquad \vartheta_m = \hat{\vartheta}_m(t_{0,k-1}), \tag{3.27a}$$

$$\chi_o(t_{0,k}) = \hat{\chi}_{o,k}(t_{0,k}), \qquad \rho_o = \hat{\rho}_o(t_{0,k-1}), \tag{3.27b}$$

$$P_o(t_{0,k}) = \hat{P}_{o,k}(t_{0,k}), \tag{3.27c}$$

where we notice that the parameter estimates are assumed to be constant $\forall t \in \mathbb{T}_{k-1}^k$.

**Remark 3.3.** If we consider sensor $m$, it may not have the ideal initial condition $x_m(t_{0,k-1}) = x_m^\star(t_{0,k-1})$. For instance, the orientation may be slightly different, so

using the optimized control input $u_m^\star(t)$ to predict the closed-loop behavior is not wise. This choice would produce a completely different path than we found from the optimization. Thus, we need a reasonable expected closed-loop response for the mobile sensor when we are given the initial condition $\hat{x}_m(t_{0,k-1})$ and the desired closed-loop behavior $x_m^\star(t)$ for all $t \in \mathbb{T}_{k-1}$. This can be achieved by applying a path-maneuvering controller to the dynamics of the sensor to solve the problem $\forall t \in \mathbb{T}_{k-1}^k$:

$$\min_{u_m} \quad |x_m^\star(t) - x_m(t)| \tag{3.28a}$$

$$\text{s. t.} \quad \dot{x}_m(t) = f_m(t, x_m(t), u_m(t), \vartheta_m), \tag{3.28b}$$

$$x_m(t_{0,k-1}) = \hat{x}_m(t_{0,k-1}), \quad \vartheta_m = \hat{\vartheta}_m. \tag{3.28c}$$

See for instance Skjetne et al. (2004).

## 3.6 Implementation

To efficiently solve the OCP (3.24), we choose a direct transcription approach where both the state and control variables are discretized into a finite-dimensional nonlinear programming (NLP) problem. The simultaneous collocation of finite elements is used to obtain Lagrange interpolation polynomial descriptions of the state variables. The control input is piecewise constant, whereas the states are described using K-point Radau collocation, for details consult Biegler (2010).

The resulting large-scale NLP formulation benefits from being sparse and having structure. These properties can be exploited using an efficient NLP solver. We formulate the problem in the symbolic framework CasADi (Andersson et al., 2012), which provides the necessary derivative information required by both the extended Kalman filter and the NLP solver. The CasADi library contains an interface for the primal-dual interior-point NLP solver IPOPT (Wächter et al., 2006). IPOPT is compiled with OpenBLAS (Xianyi et al., 2012) and the linear algebra sparse direct solvers MA27 in Section 3.7.1 and MA57 in Section 3.7.2 (HSL, 2011).

When solving initial value problems, for instance when finding predicted trajectories of the objects or expected closed-loop behavior of the mobile sensors, we use the ODE solver CVODES of the SUNDIALS suite (Hindmarsh et al., 2005).

Initial desired paths are provided a priori because paths need to be available when the first optimization is running. We provide control inputs that ensure collision avoidance and feasible execution within the constrained region. The performance of the discretized optimization problem benefits from good initial conditions. We initialize the object state and covariance variables by solving the matching IVPs with expected closed-loop behaviors of the sensors given their respective predicted initial conditions. Since a new optimization horizon goes beyond the previous, we use the previous iterations final control input as extrapolation.

**Figure 3.5** Maritime Robotics' Penguin B from UAV Factory that was used during the experiments.

## 3.7 Results

### 3.7.1 Case 1 (Experiment): Problem 3.1 Revisited

In the following, we take a second look at Problem 3.1 with $n_o = 3$ and employ the path-planning framework outlined in the previous sections in an experiment to serve as proof of concept. The models for the mobile sensor and the objects are as described in Section 3.7.1.

#### Setup

A set of simulated objects were monitored by an unmanned aerial vehicle (UAV) with waypoint-tracking capability. More specifically, a Penguin UAV B from UAV Factory (UAV Factory, 2013) was used as the mobile sensor platform, see Figure 3.5. The fixed-wing aircraft is equipped with a Piccolo autopilot and is operated through the flight management software Piccolo Command Center from Cloud Cap Technology (Cloud Cap Technology, 2013). The unmanned aircraft system was hosted by Maritime Robotics AS (Maritime Robotics, 2013) and the experiments were performed at Eggemoen Aviation and Technology Park, Ringerike, Norway.

The path-planning algorithm was run on a laptop computer and received aircraft telemetry data at 1 Hz (aircraft position and orientation) from the Piccolo Command Center trough a TCP/IP connection. The continuous-time north and east trajectories of the planned path were sampled at 1/8 Hz. These coordinates, together with a constant altitude of 600 m, were transformed into latitude and longitude decimal degrees (WGS84) and written to compatible waypoint files. These files were manually uploaded to the aircraft autopilot by a flight operator in a timely manner.

The north and east operational region is a closed convex polygon described by the linear inequality $Ay \leq b$. The mobile sensor's initial condition was $\hat{x}(t_0) = \text{col}(1360.36, 819.14, 4.14)$, with $t_0 = 0.84\,\text{s}$. The bank angle was constrained to be within $[u_{\theta,L}, u_{\theta,H}] = [-\frac{\pi}{9}, \frac{\pi}{9}]$. The initial condition for the bank was $u_\theta(t) = 0.1$. The standard gravity $g$ was set to $9.81\,\text{m}\,\text{s}^{-2}$ and the airspeed $V_a$ was $28\,\text{m}\,\text{s}^{-1}$. The field of view of the mobile sensor is defined as in (3.12) with $\Delta_{x_1} = \Delta_{x_2} = 300\,\text{m}$. We use the same smooth sampling functions for all the measurement matrices

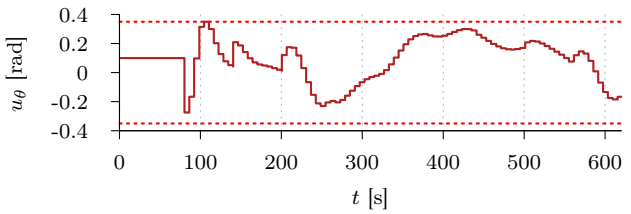


**Figure 3.6** The optimized control input that are used together with the low-fidelity vehicle model to construct the desired paths for the mobile sensor. The input remains within the upper and lower constraint, which are indicated by dashed lines.

$W_{o\in\mathbb{I}_3,1} = w_{\mathcal{C}^\infty}(\cdot)I_2$, where $w_{\mathcal{C}^\infty}(\cdot)$ is defined as in Example 3.1 with $n = 1$, $K_1 = 3.3 \times 10^{-5} I_2$.

All the objects were described with constant velocity dynamics with initial positions $\hat{\chi}_1(t_0) = \text{col}(1360, 700)$, $\hat{\chi}_2(t_0) = \text{col}(2946, -689)$, and $\hat{\chi}_3(t_0) = \text{col}(2400, 440)$, where $t_0 = 1.00\,\text{s}$. The velocity parameters were $\rho_1 = \text{col}(-1.15, -0.96)$, $\rho_2 = \text{col}(-0.82, 0.57)$, and $\sigma_3 = \text{col}(0, 0)$. Object 1 and 2 were considered to have uncertain velocities, so augmented extended Kalman filters were used in the observer with initial parameter estimates $\hat{\rho}_1(t_0) = \text{col}(-2, -0.2)$ and $\hat{\rho}_2(-1.2, 0)$. The estimation error covariance matrices in the filters were $P_1(t_0) = P_2(t_0) = I_4$ and $P_3 = I_2$. The spectral density used by the Kalman filters were $Q^{\chi}_{o\in\mathbb{I}_3} = 0.1 I_2$ and $Q^{\rho}_{o\in\mathbb{I}_2} = 10^{-3} I_2$. The positions of all the objects were measured with $C_{o\in\mathbb{I}_3} = I_2$ with measurement spectral density $R_{o\in\mathbb{I}_3} = 10 I_2$ and measurement frequency of 1 Hz (if inside the FOV). It is worth pointing out that the path planner itself modeled the covariance dynamics of the objects as state estimation only, that is, $P_{o\in\mathbb{I}_3} = I_2$ and $Q_{o\in\mathbb{I}_3} = 0.1 I_2$. The sampling function in (3.19) is for each $o \in \mathbb{I}_3$ defined as the bell curve of Example 3.1 with $n = 1$ and $K_1 = 5.2 \times 10^{-7} I_2$.

The optimization horizon was 120 s and the sampling interval 60 s. A 2-point Radau collocation was used for the state variables with a total of 40 finite elements at each optimization horizon. The control input was piecewise constant with 20 finite elements over the horizon. The resulting optimization problem had 2540 variables. Variables with unit meter were scaled by 1/100 in the optimization problem and the following variables were used in the scaled OCP: $v^L_{o\in\mathbb{I}_3}(t) = 25\,\text{col}(1, 1)$, $\Gamma_1(t) = 5$, $\Xi_1(t) = 0$, and $v^M_{o\in\mathbb{I}_3} = 40\,\text{col}(1, 1)$. The experiment was run for a total of 9 sampling intervals.

### Experimental Results

The solution time of each sampling interval was on average 19.55 s with a standard deviation of 11.75 s. The maximal solve time was 30.09 s, so all the optimization problems found optimal solutions and sampling intervals could be uploaded by the operator within the time limit of 60 s. The optimized control input used to construct the executed desired paths are displayed in Figure 3.6. The commanded input always remains within the indicated bounds, so the paths are feasible with respect to the low-fidelity vehicle model.

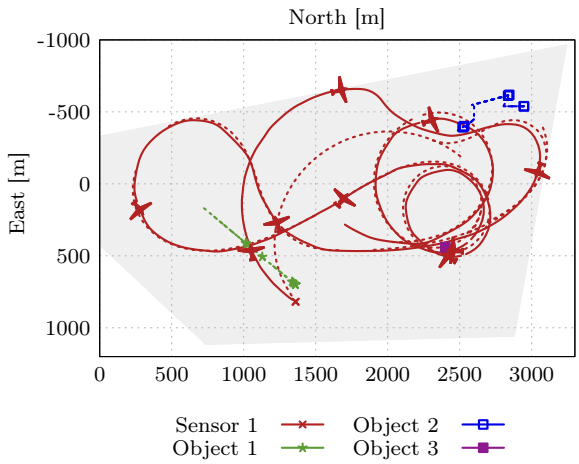


**Figure 3.7** The mobile sensor performs remote sensing of the three objects in question. The dashed line represents optimized/predicted trajectories, whereas solid lines are filtered values. Every aircraft marker represents the instant when a new sampling interval is employed. An object observation is represented with a line marker. The shaded polygon is the admissible region.

In Figure 3.7, the position trajectories of the sensor and all the objects are displayed. The dashed lines indicate optimized or predicted paths, and the measured paths are solid. Each measurement observation is indicated by a line marker. A new sampling interval is indicated by an aircraft marker. We see that with the exception of the first sampling interval, the mobile sensor followed the planned path fairly well. The reason why the aircraft did not follow the first sampling interval was because there was a discrepancy between the a priori uploaded nominal path, which the aircraft actually followed, and the calculated corresponding path for this iteration. The first iteration was not found using an optimization, but rather by solving the low-fidelity model with a constant control input and the mobile sensor's initial condition. Since this model did not take into account wind parameters, the slip-angle of the aircraft at the initial state resulted in the mentioned discrepancy. Otherwise, we see that the aircraft remained within the shaded operation region, but had some tendency to circulate close to Object 2 and 3.

As the aircraft moved between the different objects, the uncertainty of an object's position were reduced at each matching object observation. Figure 3.8 illustrates the traces of the object's covariance matrices, which represent the position uncertainties. Since the velocity parameters of Object 1 and 2 were considered uncertain in the Observer component, the position variances increased more rapidly than for Object 3. At each observation of Object 2, we can see from Figure 3.9 that the estimated velocity parameters got closer and closer to the actual velocities.

A subset of the planned paths are illustrated in Figure 3.10. We can observe that the paths are connected at the time instant of switching of sampling intervals (indicated by a perpendicular solid line). The switching occured every 60 s, which is

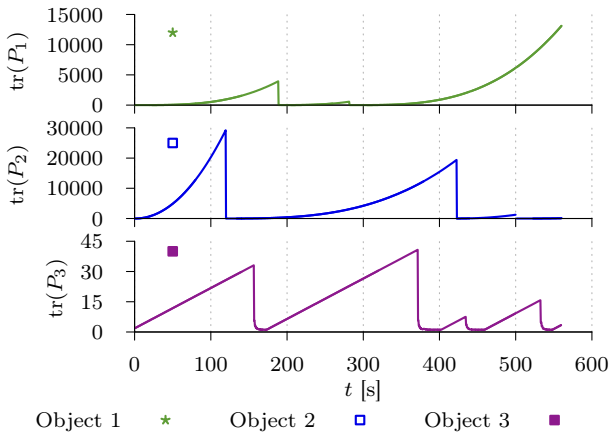


**Figure 3.8** The trace of each object's covariance matrix. An object observation is indicated by a significant reduction in the trace magnitude.

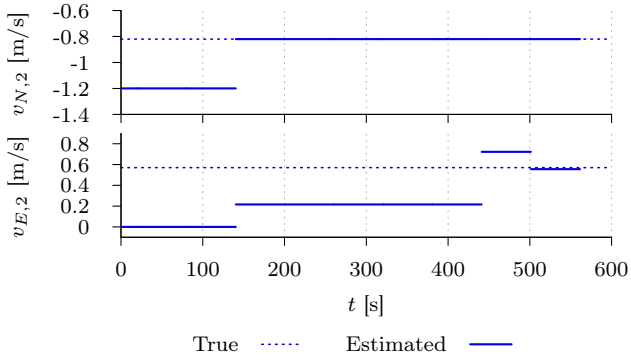


**Figure 3.9** The north and east velocity parameters for Object 2. The parameter estimates remain constant between observations.

half of the optimization horizon. Each aircraft marker in Figure 3.10 has a period of 15 s. If we count aircraft markers within Iteration 3, we see that the aircraft spent more than 60 s following this sampling interval. The low-fidelity vehicle model did not include wind velocity. The aircraft was set to follow the waypoints sampled from the optimized path at a constant airspeed. As a consequence, the nonzero wind velocity influenced how fast the aircraft moved along the desired path. This discrepancy between model and reality forced early or delayed switching of sampling intervals by the flight operator.

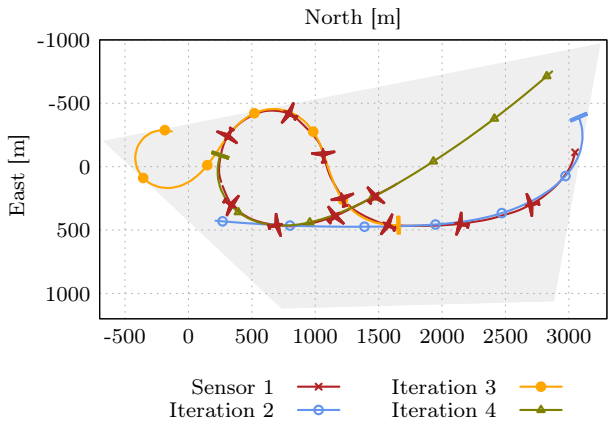


**Figure 3.10** Three iterations of planned paths are displayed. A new sampling interval is indicated by a path-perpendicular bold line, which occurs once every 60 s. Each optimization horizon is 120 s. The mobile sensor's actual position is indicated by an aircraft marker every 15 s.

### 3.7.2 Case 2 (Simulation) Sensor Network

#### Setup

We will investigate a bigger case with two mobile sensors and six objects to be monitored. In this case we employ collision avoidance where the exclusion regions of the sensors are balls with radius of 1000 m. The sensor dynamics of each sensor is identical to the previous case with the same parameters unless stated otherwise. The initial conditions for the sensors' states were $x_1(0) = \text{col}(1000, -1000, 0)$ and $x_2(0) = \text{col}(1000, 1000, 0)$.

The objects were considered to have known parameters and had either constant velocity dynamics as described in (3.1) or the following circular dynamics:

$$\dot{\chi}_N = V\cos(2\pi ft + \phi) + w_N(t), \tag{3.29a}$$
$$\dot{\chi}_E = V\sin(2\pi ft + \phi) + w_E(t), \tag{3.29b}$$

where $\chi_N$ and $\chi_E$ is the north and east coordinates, $V$ ($\text{m}\,\text{s}^{-1}$), $f$ (Hz), and $\phi$ (rad) are known parameters, so $\sigma := \text{col}(V, f, \phi)$, and $\text{col}(w_N(t), w_E(t)) =: w^\chi(t) \sim (0, Q(t))$ is process noise. Common for all the objects are the following parameters: $P_{o\in\mathbb{I}_6} = I_2$, $Q_{o\in\mathbb{I}_6}(t) = 0.1I_2$, $C_{o\in\mathbb{I}_6}(t) = I_2$, $R_{o\in\mathbb{I}_6}(t) = 10I_2$, and the sampling function in (3.19) is the bell curve of Example 3.1 with $n = 2$, $\lambda_1 = 0.4$, $K_1 = 1.4 \times 10^{-8} I_2$ and $K_2 = 1.2 \times 10^{-7} I_2$. Otherwise, the initial conditions, parameters, and dynamics are indicated in Table 3.1.

We used the same optimization horizon, sampling interval and collocation as in the previous case. This time the optimization problem had 5080 variables. Variables with unit meter were again scaled by 1/100 in the optimization problem and the following variables were used in the scaled OCP: $v^L_{o\in\mathbb{I}_6}(t) = 25\,\text{col}(1, 1)$, $\Gamma_{m\in\mathbb{I}_2}(t) = 5$, $\Xi_{m\in\mathbb{I}_2}(t) = 0.5$, and $v^M_{o\in\mathbb{I}_6} = 40\,\text{col}(1, 1)$. The experiment was run for a total of 17 sampling intervals.

**Table 3.1** Object data for the multi-sensor numerical simulation.

| o | Initial state [m] | Parameters ($\sigma_o$) | Dynamics |
|---|---|---|---|
| 1 | $[5200, -3300]^\mathsf{T}$ | $[-2.82, 1.03]^\mathsf{T}$ | (3.1) |
| 2 | $[5000, 2400]^\mathsf{T}$ | $[-2, -1]^\mathsf{T}$ | (3.1) |
| 3 | $[3000, -1750]^\mathsf{T}$ | $[3, 1800, \pi/2]^\mathsf{T}$ | (3.29) |
| 4 | $[3000, 1000]^\mathsf{T}$ | $[5, 1500, 25\pi/36]^\mathsf{T}$ | (3.29) |
| 5 | $[5500, -1500]^\mathsf{T}$ | $[-2.6, 1.5]^\mathsf{T}$ | (3.1) |
| 6 | $[5500, 1500]^\mathsf{T}$ | $[-1, 0]^\mathsf{T}$ | (3.1) |

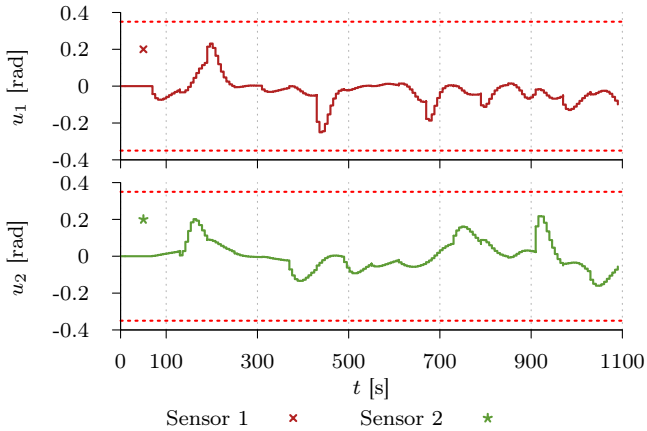


**Figure 3.11** The optimized control inputs of the two vehicles that are used together with the low-fidelity vehicle models to construct the desired paths for the mobile sensors. The inputs are always within the bounded intervals, whose boundaries are indicated by dashed lines.

### Numerical Results

The solution time of each sampling interval was on average 53.48 s with a standard deviation of 28.23 s. Three of the 17 optimization problems spent more than 60 s finding an optimal solution. To mitigate the occasional aircraft circling above an object that was experienced in the previous case, a term penalizing nonzero bank angle was introduced. We see from Figure 3.11 that this led to a more conservative use of the bank angle compared to Figure 3.6. Figure 3.12 illustrates that the Euclidean distance between the mobile sensors always stayed at least 1000 m apart as required by the collision avoidance constraint.

Figure 3.13 illustrates the trajectories of the mobile sensors and the moving objects. As in the previous case, an observation is indicated by a line marker, and a new sampling interval starts at every aircraft marker, that is, each aircraft marker is 60 s apart. The operational region is the shaded trapezoid. If we inspect the trace of the objects' covariances in Figure 3.14, we see that all the objects are visited regularly to avoid huge estimation error covariances, which represent uncertainty.

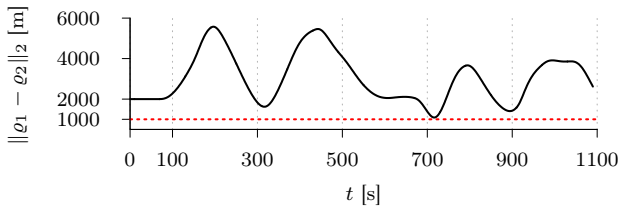


**Figure 3.12** The Euclidean distance between the two mobile sensors. The minimum distance constraint is indicated by the dashed line at 1000 m.

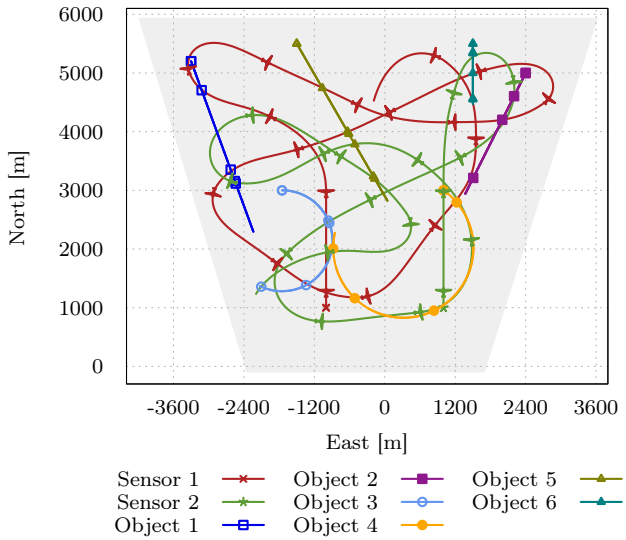


**Figure 3.13** The mobile sensors perform remote sensing of six objects in question. Every aircraft marker represents the instant when a new sampling interval is employed. An object observation is represented with a line marker. The shaded polygon is the admissible region.

## 3.8 Discussion

The solutions to the optimization problems do not guarantee recursive feasibility. For this reason it is easy to construct cases where the optimization problem will fail. This challenge becomes particularly prominent if the admissible region has tight corners such as wedges or if there are many mobile sensors trying to avoid collision in a constricted region. One way to reduce the possibility of infeasibility caused by these challenges is to introduce soft constraints. This is a slippery slope because this may conceive unwelcome behavior such as vehicle collisions and sensors temporarily leaving the admissible region. A more comprehensive solution would be to define terminal constraints that guarantee that an infinite horizon without constraint violations can be constructed. Finding appropriate terminal constraints is not a trivial task and may also adversely affect the monitoring performance and solve times. A third option is to develop infeasibility handling that temporarily suspend the monitoring operation. In our application, the path planning is constricted to

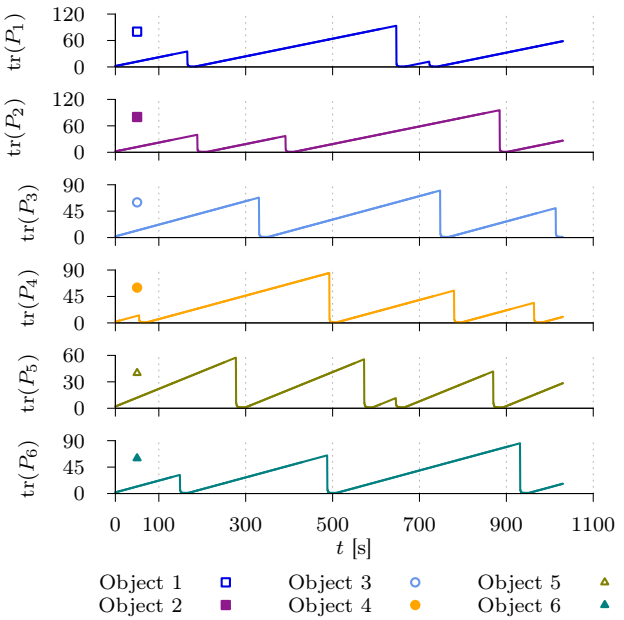


**Figure 3.14** The trace of each object's covariance matrix in the multi-sensor simulation. An object observation is indicated by a significant reduction in the trace magnitude.

planar monitoring, but if the altitude is exploited as a degree of freedom, the problem becomes even less restricted in the sense that primitive emergency behavior can be executed to ensure collision avoidance in the event of e.g. feasibility issues. In practice, infeasibility due to spatial configuration limitations may be less probable when constructing an operational region with sufficient leeway for a small number of mobile sensors.

When the number of mobile sensors or objects increases, the optimization problem grows accordingly. Due to the non-convexity of the optimization problem, it is difficult to beforehand determine the maximal solve time. Occasionally, finding a solution to the optimization problem may not meet the temporal deadline for the next sampling interval. To ensure operational safety, a nominal aircraft behavior that can be reached from a set of mobile sensor configurations may be activated if the deadline is not met. This can for instance be that each aircraft enters distinct regions and remains there until a new sampling interval is ready. This nominal aircraft behavior is related to the above discussed infeasibility handling.

This framework is a centralized solution that has the challenge that it does not scale particularly well with the number of sensors and objects. Therefore, a possible extension in form of a decentralized system is very attractive. Unfortunately, the current problem formulation is inherently centralized, so a decentralized solution is not straightforward. We imagine that an extension still is possible trough region separation and resource allocation. In particular, one may explore the possibility of making a more sophisticated *Supervision* component. This component will be responsible for defining several regions, in which each region has a few mobile sen-

sors that perform the monitoring of a limited number of objects. The monitoring system, which is described in this manuscript, executes decentralized in each region. Sensors and objects may be reallocated during the course of the operation depending on the objects movements between regions and each region's reported performance index or grade of urgency, that is number of objects and size of the region. This approach will still have a centralized management behavior that pulls the strings at a higher logical level than each monitoring team.

The proposed path planning framework includes the assumption that at least rough estimates of all the objects' states and parameters are known beforehand, for instance from satellites. If an object's parameters or initial conditions are far off, the sensor may fail to observe the object altogether. The current framework does not handle such events, but this may be approached by propagating the event to other system components. For instance, one mobile sensor may be allocated to perform a detection strategy (Tisdale et al., 2009), while the remaining mobile sensors continue the object monitoring. One can also imagine extensions that perform both object monitoring and detection simultaneously. If we perform more frequent updates of the sampling intervals, loss of object tracking may be less probable, because the objects' predicted trajectories are updated more frequently by the acquired information.

During the experiment, each sampling interval's corresponding waypoint file was uploaded manually by the flight operator. This procedure involved human interaction and was error-prone because the flight management software is not designed for rapid changing of waypoint files. As a consequence, conservative sampling intervals had to be chosen to ensure proper switching of the intervals. The low-fidelity model was inaccurate in terms of not including wind speeds. This led to temporal drifts in the execution of the planned paths, since the autopilot followed the waypoints with constant desired airspeed. If we either had estimated wind speeds and included them in the low-fidelity vehicle model and/or used an autopilot with variable airspeed, this phenomenon could perhaps have been less prominent.

## 3.9 Conclusion

The path planning algorithm presented in this manuscript provides collision-free vehicle trajectories that seek to minimize the objects' uncertainties. These uncertainties are quantified by the state and parameter estimation error variances of the objects. This approach therefore tries to aid efficient state and parameter estimation of the objects while simultaneously providing feasible vehicle trajectories. The formulated optimal control problem allows flexibility in the description of both vehicle and object dynamics. This includes nonholonomic vehicle dynamics and object dynamics with constant velocity, but could also capture more advanced model descriptions.

Field experiments demonstrate the framework. It would be interesting to see a more involved experiment where real objects were tracked combined with real-time image processing. This should include an aircraft path maneuvering controller that can follow the planned trajectories more closely without any human-in-the-loop during the execution of the monitoring.

# Chapter 4

# Monitoring an Advection-Diffusion Process Using Aerial Mobile Sensors

*The topic of this chapter is to describe a path planning framework for regional surveillance of a planar advection-diffusion process. The goal of the path planning is to produce feasible and collision-free trajectories for a set of aerial mobile sensors that minimize some uncertainty measure of the process under observation. The problem is formulated as a dynamic optimization problem and discretized into a large-scale nonlinear programming (NLP) problem using the Petrov-Galerkin finite element method in space and simultaneous collocation in time. Receding horizon optimization problems are solved in simulations with an advection-dominated ice concentration field. The simulations illustrate the usefulness of the proposed method. This work is submitted to Unmanned Systems, October 2014.*

## 4.1 Introduction

The use of unmanned vehicles in various applications has received increasingly more attention the last decade. Continued technological progress makes both software and hardware solutions more available and affordable to civilian applications. Engineering applications that use unmanned vehicles often also consist of complex components. This complexity has given rise to a new field of study termed *cyber-physical systems (CPSs)* (CPS Steering Group, 2008; Tricaud et al., 2012). In CPS Steering Group (2008), a CPS was loosely defined as "the tight conjoining of and coordination between computational and physical resources". In our context this involves a remotely piloted aircraft system (RPAS) in conjunction with a distributed parameter system (DPS) (Tricaud et al., 2012, Section 1.1.2), which is described with an advection-diffusion partial differential equation (PDE). A particular branch of applications in CPS is environmental monitoring. This includes for instance weather forecasting (Choi et al., 2010), oil-spill estimation (You et al., 2011), soil moisture estimation (Tricaud et al., 2012, Ch. 8), (Kaheil et al., 2008), air pollution (Georges, 2013), and polar remote monitoring (Haugen et al., 2012, 2013a,b, 2014b, 2011; Lubin et al., 2006).

Before the increased use of unmanned vehicles, many of the mentioned problems

utilized satellites, manned vehicles, or even *in situ* measurements. For safety-critical or highly dynamical systems, the traditional approach may not offer sufficiently fine spatiotemporal resolution. Moreover, the use of unmanned observation systems may reduce cost and promote occupational safety and health compared to manned operations.

We are motivated by ice management operations, were, among other things, the ice conditions surrounding a marine operation are of special interest. The marine operation is safety-critical and accurate knowledge about the surrounding environment is important to ensure responsible and efficient execution. In Haugen et al. (2011), the authors argued that unmanned aerial vehicles (UAVs) may serve as a sensor platform as part of a CPS termed *ice observer system*. One important aspect of this system is the monitoring of drifting sea ice concentration (Gürtner et al., 2012), that is, the fraction area of sea ice versus open water. Suppose we want to monitor the ice concentration, which can be modeled as an advection-diffusion process, in a region close to a marine operation. We are interested in estimating the ice concentration, which moves with the sea current. At our disposal we have one or several aerial mobile sensor agents that are capable of remotely sensing the planar advection-diffusion process through appropriate limited-range measuring devices. The main task that we want to solve is how to efficiently estimate the states and parameters of the DPS within the prescribed region. The monitoring task should be autonomous and ensure collision-free and feasible vehicle trajectories within a bounded admissible region of operation.

The above objective is related to the coverage control problem, which is the problem of covering a given domain using sensor networks (Wang et al., 2012). The authors of Wang et al. (ibid.) divide the literature on coverage control problem into three categories: optimal localization of immobile sensing agents (Omatu et al., 1978; Vaidya et al., 2012), redistribution of mobile sensors to an optimal final configuration (Cortés et al., 2005; Georges, 2013), and dynamic cooperative coverage control (Burns et al., 2009; Y. Chen et al., 2004; Choi et al., 2010; Demetriou, 2010; Demetriou et al., 2009; Hussein et al., 2007; Song et al., 2005; Tricaud et al., 2012). The present work falls under the last mentioned category because of several reasons. First, the mobile agents have limited-range sensors, only capable of covering a fraction of the whole domain of interest at any given time. Optimally placing or redistributing the sensors may not ensure sufficient information gathering. Second, the dynamics of fixed-wing aerial sensors have positive airspeed, which exclude them from having a constant spatial configuration. Lastly, the desired information to be gathered evolves in both time and space, so the dynamic behavior of the DPS warrants a tight interaction between the dynamic environment and the path planning.

When executing a coverage control problem, several different monitoring tasks have been considered in the past, including, but not limited to: state estimation (Burns et al., 2009; Y. Chen et al., 2004; Choi et al., 2010; Demetriou, 2010; Demetriou et al., 2009; Song et al., 2005), parameter identification (Y. Chen et al., 2004; Song et al., 2005; Tricaud et al., 2012), and process actuation (Y. Chen et al., 2004; Demetriou, 2010; Tricaud et al., 2009). In most of these publications a centralized and cooperative sensor network strategy is considered, with the exception of (Demetriou, 2010), where they consider both a decentralized and a centralized

coverage control strategy.

Various fundamental approaches and performance measures are used to achieve the different monitoring tasks. For the parameter identification path planning problem, one often wants to achieve a least-squares fit to data of some output operator (Tricaud et al., 2012). The performance index to determine optimal sensor trajectories is often a function of the Fisher information matrix (FIM) (ibid.), which is based on the parameters to be estimated. The problem is formulated as an optimal control problem (OCP) that provides the optimal mobile sensor trajectories subject to the DPS, mobile sensor dynamics, and other relevant constraints (Song et al., 2005; Tricaud et al., 2009; Tricaud et al., 2012). The OCPs seek to minimize a so-called D-optimality reward function (Tricaud et al., 2012, p. 26), which indicates the volume of the parameters' estimation error uncertainty ellipsoid.

The optimal control problem formulation has also been used for state estimation (Burns et al., 2009; Choi et al., 2010). Both a weighted trace (A-optimality) (Burns et al., 2009) and a D-optimality (Choi et al., 2010) performance index (of possibly a subset (ibid.)) of the state estimation variables have been used. In Choi et al. (ibid.), the goal of the path planning was to find optimal paths in a time interval to maximize information reward of verification variables some time in the future. Both Burns et al. (2009) and Choi et al. (2010) have a Riccati matrix differential equation based on the DPS state variables as a constraint in the OCP. For this reason, the corresponding nonlinear programming (NLP) problem quickly becomes huge and computational tractability is a challenge.

Computational efficient alternatives to the distributed state estimation task was pursued in Demetriou (2010); Demetriou et al. (2009); Haugen et al. (2012). They used gradient-based guidance algorithms for mass-spring-damper (Haugen et al., 2012) or massless (Demetriou, 2010; Demetriou et al., 2009) points to minimize either local or idealized global state estimation error of advection-diffusion PDEs. These contributions do not include collision avoidance of the mobile sensor agents or communication constraints, but this was discussed as a straightforward extension.

Herein, we exploit the flexibility of the OCP formulation to easily include vehicle maneuverability constraints and collision avoidance in finding optimal feasible vehicle trajectories for the state estimation task. We are motivated by Burns et al. (2009); Choi et al. (2010); Haugen et al. (2013a, 2014b), which make use of the Riccati differential equation for the estimation error covariance. However, to alleviate some of the computational burden that the Riccati equation represents, we propose a simplified description of the uncertainty time evolution in the OCP.

### 4.1.1 Notation

An n-dimensional column vector of ones is denoted $1_{n\times 1}$. $I_n$ is the $n \times n$ identity matrix. A countable finite index set of positive natural numbers is defined as $\mathbb{I}_n := \{i \in \mathbb{N}^+ : i \leq n\}$ with counting measure $|\mathbb{I}_n| = n$. For the bounded domain $T \subset \mathbb{R}^n$ and $x \in T$, we define $|T| := \int_T dx$. A block diagonal matrix of other matrices $X_{i\in\mathbb{I}_s} \in \mathbb{R}^{m_i\times n_i}$ is defined as $\text{bdiag}_{i\in\mathbb{I}_s}(X_i) := \bigoplus_{i\in\mathbb{I}_s} X_i$, where $\oplus$ is the direct sum. The vertically stacked matrix of other matrices $X_{i\in\mathbb{I}_s} \in \mathbb{R}^{m_i\times n}$ is denoted $\text{col}_{i\in\mathbb{I}_s}(X_i) := \text{bdiag}_{i\in\mathbb{I}_s}(X_i) \cdot (1_{s\times 1} \otimes I_n)$, where $\otimes$ is the Kronecker product. The vertical stacking of the columns of a matrix $X$ is defined as $\text{vec}(X)$. The diagonal

of a column vector $x \in \mathbb{R}^n$ is the block diagonal of its scalar elements $x_i$, $\text{diag}(x) := \text{bdiag}_{i \in \mathbb{I}_n}(x_i)$. The column vector $x \in \mathbb{R}^n$ consisting of the diagonal elements of a matrix $X \in \mathbb{R}^{n \times n}$ is written $x := \text{diag}(X)$. The space of non-zero $n$-dimensional real vectors is denoted $\mathbb{R}^n_{\neq 0}$. Define the set of positive definite real matrices as $\Pi_n := \{A \in \mathbb{R}^{n \times n} : \forall x \in \mathbb{R}^n_{\neq 0}, x^\mathsf{T} A x > 0\}$. The orientation space is defined by $\mathbb{S} := [-\pi, \pi)$. Define the $L^p$-normed n-dimensional metric space $M_p = (\mathbb{R}^n, \|\cdot\|_p)$. The corresponding open ball with origin $\eta \in \mathbb{R}^n$ is $\mathcal{B}_p(\eta; r) := \{x \in M_p : \|\cdot\|_p < r\}$. We denote the support of a function $f : X \to \mathbb{R}$ as the closure of the non-zero codomain of $f$, denoted $\text{supp}(f) := \text{cl}(\{x \in X : f(x) \neq 0\})$.

The first moment of a random vector $x$ is denoted by the expectation operator $\text{E}(x)$. The covariance matrix of two random vectors $x$ and $y$ is defined as $\text{cov}(x, y) := \text{E}[(x - \text{E}(x))(y - \text{E}(y))^\mathsf{T}]$. Non-negative and positive real numbers are defined, respectively, by the sets $\mathbb{R}_{\geq 0}$ and $\mathbb{R}_{>0}$. A zero-mean continuous-time white noise process $w(t)$ of dimension $n$ has the properties $\text{E}(w) = 0$ and $\text{cov}(w(t), w(\tau)) = Q(t)\delta(t - \tau)$, where $Q : \mathbb{R}_{\geq 0} \to \Pi_n$ is the deterministic spectral density and $\delta(t)$ is the dirac delta function. The above mentioned properties of $w(t)$ are written compactly as $w(t) \sim (0, Q(t))$.

Let $\Omega \subset \mathbb{R}^2$. Lebesque spaces are denoted $L^p(\Omega)$. Sobolev spaces are denoted $W^{k,p}(\Omega)$, where $H^k(\Omega) = W^{k,2}(\Omega)$. The inner product in the space $L^2(\Omega)$ is denoted by $\langle \cdot, \cdot \rangle$. A closed interval on the real line (particularly in the context of time) is defined as $\mathbb{T}^b_a := \{x \in \mathbb{R} : a < b, a \leq x \leq b\}$. Bochner spaces are denoted $L^p(\mathbb{T}^b_a; X)$.

## 4.2 Problem Overview

### 4.2.1 Illustrating Example

Suppose we want to monitor the sea ice concentration in a region. We define the sea ice concentration as the area fraction of ice versus water in a unit area. We are particularly interested in estimating the ice that will drift through or close to a verification location $s_v$ some time in the future. At our disposal we have a set of aerial mobile sensors that are capable of measuring the ice concentration, for instance by using optical devices. Suppose the mobile sensors perform monitoring in an annular sector, see Figure 4.1. The objective is to create collision-free trajectories for the mobile sensors such that the ice concentration can be estimated.

### 4.2.2 System Components

We approach the objective by first identifying the three main components in the surveillance system:

**RPAS:** Remotely piloted aircraft system that acts as a mobile sensor network. It provides measurements of the distributed process.

**Estimator:** Processes raw measurements and other inputs to return the most likely model states and parameters of the mobile sensors and the process.

**Path Planner:** Generates guidance inputs of when and where we want the mobile sensors to obtain measurements of the process.

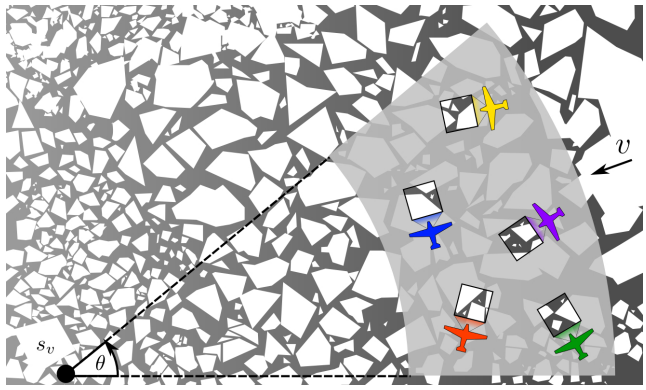


**Figure 4.1** Mobile sensors monitoring ice concentration in an annular sector. $v$ is the uniform ice velocity, $s_v$ is a verification location, and $\theta$ is the sector opening angle.

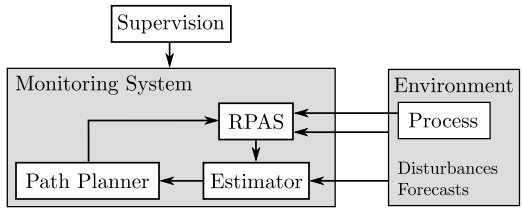


**Figure 4.2** Components of the system under consideration.

The *Supervision* component performs management decisions such as how many mobile sensors to deploy, which region to cover, and other relevant judgment calls. An overview of the system is found in Figure 4.2. In this manuscript we will mainly focus on the *Path Planner* and parts of the *Estimator* component.

The *Estimator* component provides relevant estimates for both the process under observation, as well as the mobile sensor network's variables. In this manuscript we will only consider the former, namely how to estimate the states and parameters of the environmental process. If the state estimates of the mobile sensors are needed (e.g. the planar positions), we assume that they are known with sufficient accuracy. The estimator for the process contains an approximated model of the phenomenon of interest. This model and its spatial discretization are described in general in Section 4.5 and further motivated together with the estimator of choice in Section 4.6.

The *Path Planner* consists of a dynamic optimization problem. We formulate the optimization problem by including appropriate descriptions of the involved ingredients. In particular, we give the mathematical descriptions of the mobile sensor dynamics and its collision avoidance in Section 4.3. We choose an information-driven approach where the objective is to minimize an uncertainty measure of the process of interest. Motivated by Haugen et al. (2014b), we want to use the trace of the state estimation error covariance of the process states as our uncertainty measure. To facilitate computational tractability, we consider a simplified description

of the uncertainty dynamics in the optimization problem. More specifically, we use the model described in Section 4.5 as a starting point for the simplified uncertainty dynamics. In Section 4.7 we elaborate on this simplification and the necessary extensions that describe the mobile sensors' influence on the reduced uncertainty dynamics. The resulting optimization problem and additional considerations are discussed in Section 4.8.

## 4.3 Mobile Sensor Dynamics

For the path-planning purposes we employ low-complexity sensor dynamics. The constant-altitude kinematic model including wind velocity may be considered as a reasonable description (Beard et al., 2012). It should be pointed out that more complex vehicle descriptions are indeed possible with the framework proposed in this paper.

Let $x_N(t)$ and $x_E(t)$ denote the north and east position of the kinematic vehicle model, and $\psi(t) \in \mathbb{S}$ the right-hand screw z-axis rotation of a body-fixed reference frame {b} relative to {ned}. Further, let the bank angle $u_\theta(t)$ be the control input. The dynamics is defined as

$$\dot{x}_N(t) = V_a \cos(\psi) + w_N, \tag{4.1a}$$
$$\dot{x}_E(t) = V_a \sin(\psi) + w_E, \tag{4.1b}$$
$$\dot{\psi}(t) = \frac{g}{V_a} \tan(u_\theta(t)), \tag{4.1c}$$

where $V_a$ is the positive airspeed, $g$ is the standard gravity, and $\vartheta := \mathrm{col}(w_N, w_E)$ is the wind velocity. The trajectories we obtain by solving the above equations should be feasible with respect to the maneuverability constraints of the vehicle if the bank angle is sufficiently restricted. We also restrict the admissible location of the vehicle to remain within a closed convex polygon. For all $t \in \mathbb{R}_{\geq 0}$ and $[u_{\theta,L}, u_{\theta,H}] =: \mathcal{U} \subset \mathbb{S}$ let $u_\theta \in \mathcal{U}$ and define

$$\mathcal{K} := \{y \in \mathbb{R}^2 : Ay \leq b\}, \tag{4.2}$$

where $A$ and $b$ have appropriate dimensions. Let $n_m$ be the number of mobile sensors and define the index set $\mathbb{M} := \mathbb{I}_{n_m}$. As a result, the state vector for sensor $m \in \mathbb{M}$ is defined as $x_m(t) := \mathrm{col}(x_{m,N}, x_{m,E}, \psi_m)$ with input $u_m(t) := u_{m,\theta}(t)$. The parameters $V_a$ and $\vartheta$ for the kinematic vehicle model may differ for different mobile sensors as well as the sets $\mathcal{U}_m$ and $\mathcal{K}_m$. The resulting mobile sensor network is $\forall m \in \mathbb{M}$ and $\forall t \in \mathbb{R}_{\geq 0}$

$$\dot{x}_m(t) = f_m(x_m(t), u_m(t), \vartheta_m), \tag{4.3a}$$
$$x_m(t_0) = x_{m,0}, \tag{4.3b}$$
$$x_m(t) \in \mathcal{K}_m \times \mathbb{S}, \tag{4.3c}$$
$$u_m(t) \in \mathcal{U}_m, \tag{4.3d}$$

where $f_m(x_m, u_m, \vartheta_m)$ is shorthand for the right-hand expressions of the kinematic vehicle dynamics (4.1a)-(4.1c).

### 4.3.1 Collision Avoidance

Collision avoidance is a requirement for enabling multiple mobile sensors to cooperate in the monitoring task. Each sensor has its own exclusion zone. Let $\forall m \in \mathbb{M}$ the vector $\eta_m(t) \in \mathbb{R}^3$ define the body-fixed origin of sensor $m$ relative the stationary reference frame {i}. Each sensor is enclosed by its own open ball $\mathcal{B}_2(\eta_m; r_m) \subset \mathbb{R}^3$ that no other sensor should enter. We formulate the collision avoidance as constraints between each pair of mobile sensors. These constraints can be found by defining a complete graph. The vertices represent mobile sensors and each edge $(i, j)$ is assigned an orientation such that sensor $i$ has a larger exclusion ball than sensor $j$, that is $r_i \geq r_j$. Let $G = (\mathbb{M}, E)$ be the described directed graph, which turns out to be a so-called tournament. Collision avoidance is ensured if $\forall t \in \mathbb{R}_{\geq 0}$ and for each $(i, j) \in E$

$$\eta_j(t) \notin \mathcal{B}_2(\eta_i(t); r_i). \tag{4.4}$$

## 4.4 Measurement Models

A mobile sensor's measurement capability of the process depends on the relative planar position between the sensor and the process being measured. This capability has to be properly described using a so-called *sampling function* (Tricaud et al., 2012). The characteristics of the sampling function are different whether it is used in the *Estimator* or in the *Path Planner*. In particular, we distinguish between a non-smooth and smooth sampling function. The non-smooth sampling function is an accurate description of the measurement capability of a process at a location: either a measurement can be provided or it cannot. This binary property is useful in the *Estimator*. In the *Path Planner*, on the other hand, this switching is not appropriate in the practical implementation of the optimization problem. This is because sufficiently smooth functions are a requirement in the chosen software that seeks the solution to the optimization problem. In the following we present sampling functions that have previously been defined in Haugen et al. (2013a), but restated here for convenience.

We define the family of scalar sampling functions as $\mathbb{W}$ and let $\mathbb{B}$ be the codomain of this family. The sampling function takes as arguments the planar position $\varrho(t)$ and the orientation $\psi(t)$ of a mobile sensor, and the planar position $p(t)$ of the process of interest. Hence, the sampling function is $w_{\mathcal{C}^k}(t, \varrho, p, \psi) : \mathbb{R}_{\geq 0} \times \mathbb{R}^2 \times \mathbb{R}^2 \times \mathbb{S} \to \mathbb{B}_{\mathcal{C}^k}$, where $\mathcal{C}^k$, $k \in \{-1, \infty\} \cup \mathbb{N}$ signifies the continuity of the sampling function.

We will use the two-dimensional rotation matrix, which is defined as

$$R(\psi) = \begin{bmatrix} \cos\psi & -\sin\psi \\ \sin\psi & \cos\psi \end{bmatrix}. \tag{4.5}$$

### 4.4.1 Non-Smooth Sampling Function

A pitch and roll stabilized downward-looking optical device has a limited field of view (FOV); Either it measures a specific location or it does not. This behavior is modeled using a non-smooth sampling function and is well suited as part of fusing measurements of a process with a model description at discrete time instants.

Let $\Delta_{x_i} > 0, i \in \{1, 2\}$ and define $\Delta_x := \mathrm{col}(\Delta_{x_1}, \Delta_{x_2})$. The planar FOV metric is a weighted infinity norm

$$\|x\|_\infty^{\Delta_x} := \max\left(\frac{|x_1|}{\Delta_{x_1}}, \frac{|x_2|}{\Delta_{x_2}}\right). \tag{4.6}$$

Let the codomain of a binary sampling function $w_{\mathcal{C}^{-1}}(t, \varrho, p, \psi)$ be $\mathbb{B}_{\mathcal{C}^{-1}} := \{0, 1\}$, such that the codomain is nonzero only if the coordinate point $p(t)$ of the process is within the convex set formed by a FOV metric. The non-smooth sampling function is thus

$$w_{\mathcal{C}^{-1}}(t, \varrho, p, \psi) := \begin{cases} 1, \left\|R^\mathsf{T}(\psi)(p - \varrho)\right\|_\infty^{\Delta_x} < 1 & \text{(4.7a)} \\ 0, \text{ otherwise.} & \text{(4.7b)} \end{cases}$$

The field of view at the sensor location $\varrho = \mathrm{col}(\varrho_1, \varrho_2)$ with $\psi = 0$ is $[\varrho_1 - \Delta_1, \varrho_1 + \Delta_1] \times [\varrho_2 - \Delta_2, \varrho_2 + \Delta_2]$.

### 4.4.2 Smooth Sampling Function

Smooth sampling functions have continuous derivatives of arbitrary degree. For this reason, these sampling functions are suitable for situations where smooth derivatives of the sampling functions are beneficial. This is the case for solving the optimization problem in our implementation this work. Let $\mathbb{B}_{\mathcal{C}^\infty} := \{w \in \mathbb{R} : 0 \leq w \leq 1\}$ be the codomain of smooth sampling functions

$$w_{\mathcal{C}^\infty}(t, \varrho, p, \psi) : \mathbb{R}_{\geq 0} \times \mathbb{R}^2 \times \mathbb{R}^2 \times \mathbb{S} \to \mathbb{B}_{\mathcal{C}^\infty}, \tag{4.8}$$

which are 1 if $\varrho = p$ and less than 1 otherwise.

**Example 4.1.** Let $K_{i \in \mathbb{I}_n} \in \Pi_2$, and $\tilde{p} = p - \varrho$. A possible smooth sampling function is the linear combination of $n$ two-dimensional Gaussian functions, for instance

$$w_{\mathcal{C}^\infty}(t, \varrho, p, \psi) := \sum_{i \in \mathbb{I}_n} \lambda_i e^{-\tilde{p}^\mathsf{T} R(\psi) K_i R^\mathsf{T}(\psi) \tilde{p}}, \tag{4.9}$$

where $\sum_{i \in \mathbb{I}_n} \lambda_i = 1, \lambda_i \geq 0$. The purpose of having a combination of exponential functions is that it enables smooth approximations. These approximations can resemble a non-smooth sampling surface while still being smooth and having a nonzero image. Figure 4.3 displays an example of such a sampling surface.

## 4.5 The Advection-Diffusion-Reaction Equation

The advection-diffusion-reaction (ADR) equation is a partial differential equation where some variable of interest change over time in three different ways.

**Advection:** The transport of the variable by the field velocity.

**Diffusion:** The movement of the quantity from a highly concentrated region to a location with lower concentration.

**Reaction:** The creation and/or destruction of the quantity.

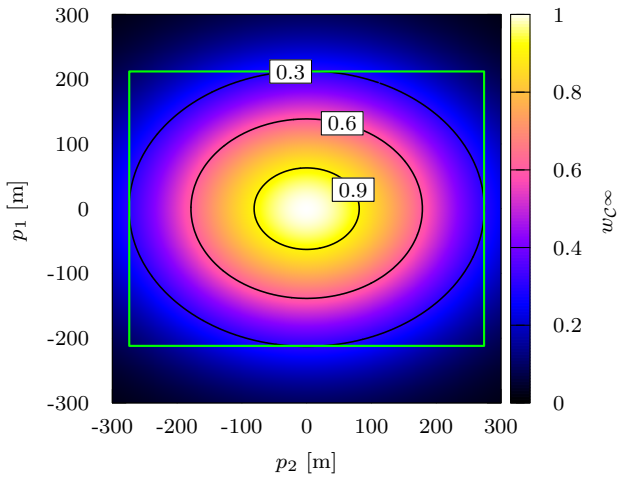


**Figure 4.3** A $\mathcal{C}^\infty$ smooth sampling function. The sensor location $\varrho$ is at the origin and the codomain of the sampling surface is plotted as a function of the process coordinates $p_1$ and $p_2$. The green rectangle indicates the box the sampling function approximates.

We intend to use this equation for the description of both sea ice concentration as well as the dynamics of some uncertainty measure. For this reason we first describe the equation with a general scalar quantity, and then substitute specific variables in Sections 4.6 and 4.7.

Let $\Omega$ be an open bounded domain in $\mathbb{R}^2$. We are interested in a time interval $\mathbb{T}_{t_0}^{t_f}$. The closure of $\Omega$ is $\Gamma = \delta\Omega = \Gamma_D \cup \Gamma_N$, were the disjoint boundary sets $\Gamma_D$ and $\Gamma_N$, represent the Dirichlet and Neumann boundary, respectively. Then, $\overline{\Omega} := \overline{\Omega \cup \Gamma}$ and let $p \in \overline{\Omega}$ be the position of a unit volume. Let $n(p) : \Gamma \to \mathbb{R}^2$ be the unit outward normal at the boundary. We define the boundary sets as

$$\Gamma_D := \{p \in \Gamma : v^\mathsf{T} n \leq 0\}, \tag{4.10a}$$

$$\Gamma_N := \{p \in \Gamma : v^\mathsf{T} n > 0\}, \tag{4.10b}$$

where $v \in L^\infty(\mathbb{T}_{t_0}^{t_f}; W^{1,\infty}(\overline{\Omega}))^2$ is the time-varying velocity field. The Dirichlet boundary is the inlet that supplies the interior with the modeled quantity, whereas the Neumann boundary is the outlet boundary.

Let $\epsilon > 0$ be the constant diffusion coefficient and $\zeta(t, p)$ the scalar quantity of interest. We consider the advection-diffusion-reaction equation

$$\dot{\zeta} + v \cdot \nabla\zeta - \nabla \cdot (\epsilon \nabla\zeta) = s, \quad (t, p) \in \mathbb{T}_{t_0}^{t_f} \times \Omega, \tag{4.11a}$$

where $s(t, p, \zeta) \in L^2(\mathbb{T}_{t_0}^{t_f}; L^2(\Omega))$ is the source/sink and reaction term. The boundary and initial conditions are

$$\zeta(t, p) = f_D(t, p), \quad (t, p) \in \mathbb{T}_{t_0}^{t_f} \times \Gamma_D, \tag{4.11b}$$

$$\nabla\zeta \cdot n = 0, \quad (t, p) \in \mathbb{T}_{t_0}^{t_f} \times \Gamma_N, \tag{4.11c}$$

$$\zeta(t_0, p) = \zeta_0(p), \quad p \in \Omega, \tag{4.11d}$$

where $f_D(t,p)$ is an assumed known function and $\zeta_0(p)$ is the initial surface of the variable of interest.

### 4.5.1 Finite Element Discretization

We seek a weak formulation of (4.11). First, define

$$H_g^k(\Omega) := \{u \in H^k(\Omega) : u = g \text{ on } \Gamma_D\}. \tag{4.12}$$

Given $\zeta_0(p) \in L^2(\Omega)$ and $s(t,p,\zeta) \in L^2(\mathbb{T}_{t_0}^{t_f}; L^2(\Omega))$, find $\zeta(t,p) \in L^2(\mathbb{T}_{t_0}^{t_f}; H_{f_D}^1(\Omega))$ such that

$$\langle \dot{\zeta}, w\rangle + a(\zeta, w) = l(w), \quad \forall w \in L^2(\mathbb{T}_{t_0}^{t_f}; H_0^1(\Omega)), \tag{4.13a}$$

$$\zeta(t_0,p) = \zeta_0(p), \quad \forall p \in \Omega, \tag{4.13b}$$

where $a(\cdot,\cdot)$ and $l(\cdot)$ are bilinear and linear forms, respectively.

In our case the equation is advection-dominated and the usual Galerkin method of discretization is not appropriate due to the requirement of very fine resolution to avoid spurious oscillations (Ern et al., 2004). We choose the popular streamline upwind Petrov-Galerkin (SUPG) method described in Brooks et al. (1982).

**Definition 4.1.** The family of sets $F(\Omega, l) := \{K_i\}_{i\in\mathbb{I}_l}$ is called a *tessellation* of $\Omega$ if $K_i \cap K_j = \emptyset$ for $i \neq j$ and $\bigcup_{i=1}^{l} \overline{K}_i = \overline{\Omega}$.

We tessellate our domain $\Omega$ into $N_l$ control volumes. Define $\mathbb{I}_{N_l} =: \mathbb{E} = \mathbb{E}_D \cup \mathbb{E}_I$ and let $\{K_e\}_{e\in\mathbb{E}}$ be the tessellation of $\Omega$. Further, define two set of points $\mathcal{P}_I = \{p_e\}_{e\in\mathbb{E}_I}, p_e \in \overline{\Omega} \setminus \overline{\Gamma}_D$ and $\mathcal{P}_D = \{p_e\}_{e\in\mathbb{E}_D}, p_e \in \overline{\Gamma}_D$. These points are the vertices of the domain tessellation often called the *mesh*. Let $\mathbb{P}_k(K_e)$ be the set of polynomials of degree at most $k$ on $K_e$. Define

$$V_g^h(\Omega) := \{v \in H_g^1(\Omega) : \forall e \in \mathbb{E}, v|_{K_e} \in \mathbb{P}_1(K_e)\}. \tag{4.14}$$

We seek a semi-discrete finite dimensional approximation $\zeta^h \in L^2(\mathbb{T}_{t_0}^{t_f}; V_{f_D}^h(\Omega))$, with the linear combination of basis functions $\varphi_e$:

$$\zeta^h(t,p) = \sum_{e\in\mathbb{E}} \zeta(t,p)\varphi_e(p), \tag{4.15}$$

where $\varphi_e \in \mathbb{P}_1(K_e)$ with the property

$$\exists\, p_e \in \overline{\Omega} \colon \varphi_e(p_e) = 1, \varphi_e(p_j) = 0,\ \forall j \neq e, p_j \in \overline{\Omega}, \tag{4.16}$$

so that

$$\zeta_i(t) := \zeta^h(t,p_i), \tag{4.17}$$

which is the shorthand notation for the nodal value at the discrete point $p_i$. The weak form is now

$$\langle \dot{\zeta}^h, w\rangle + a(\zeta^h, w) = l(w), \quad \forall w \in L^2(\mathbb{T}_{t_0}^{t_f}; V_0^h(\Omega)), \tag{4.18a}$$

$$\zeta^h(t_0,p) = \zeta_0, \quad \forall p \in \mathcal{P}_I. \tag{4.18b}$$

We proceed by choosing the test function presented in Brooks et al. (ibid.). It is $\tilde{w} = \varphi + \tau(v) v \cdot \nabla\varphi$, where $\tau(v) \in L^\infty(\mathbb{T}_{t_0}^{t_f}; L^\infty(\Omega))$ is called the intrinsic parameter. The second term of $\tilde{w}$ is defined on element interiors only. We use the divergence theorem, integrate by parts, do some reordering, and get the ordinary differential equations for nodal point $\zeta_i(t)$ :

$$\sum_{e\in\mathbb{E}} \left( \int_{K_e} (\varphi_i + \tau_i v_i \cdot \nabla\varphi_i)\varphi_e \, dp \right) \dot{\zeta}_e = \tag{4.19a}$$

$$- \sum_{e\in\mathbb{E}} \left( \int_{K_e} (\varphi_i + \tau_i v_i \cdot \nabla\varphi_i)(v_e \cdot \nabla\varphi_e) \, dp \right) \zeta_e \tag{4.19b}$$

$$- \epsilon \sum_{e\in\mathbb{E}} \left( \int_{K_e} \nabla\varphi_i \cdot \nabla\varphi_e \, dp \right) \zeta_e \tag{4.19c}$$

$$+ \sum_{e\in\mathbb{E}} \int_{K_e} (\varphi_i + \tau_i v_i \cdot \nabla\varphi_i) s_e \, dp, \tag{4.19d}$$

where $v_i = v(t, p_i)$, $\tau_i = \tau(v_i)$, and $s_e(\cdot)$ will be defined later. The piecewise integrals in (4.19) are usually approximated using quadrature rules of sufficient degree. In our application we use n-by-n point Gauss-Legendre quadratures (Dunavant, 1985; Gene H Golub, 1969). For more implementation details on SUPG and the finite element discretization, consult Brooks et al. (1982) and for instance Ern et al. (2004).

**Definition 4.2.** The coordinate system {adr} is the reference frame where the planar domain $\Omega$ is defined.

**Assumption 4.1.** *The velocity field is uniform, so* $v(t,p) = v(t) = \mathrm{col}_{\ell\in\mathbb{I}_1^2}(v_\ell(t))$, *where* $v_\ell(t)$ *is the flux speed along the standard basis* $e_\ell$ *of the Euclidean space* $\mathbb{R}^2$ *in* $\{adr\}$.

Define $\chi(t) := \mathrm{col}_{e\in\mathbb{E}_I}(\zeta_e(t)) \in \mathbb{R}^{|\mathbb{E}_I|}$, and $\chi_{\Gamma_D}(t) := \mathrm{col}_{e\in\mathbb{E}_D}(\zeta_e(t)) \in \mathbb{R}^{|\mathbb{E}_D|}$. We obtain the following ordinary differential equation (ODE) and initial condition:

$$M(v(t))\dot{\chi}(t) = (A(v(t)) - \epsilon D)\,\chi(t) + B(v(t))\chi_{\Gamma_D}(t) + r(\cdot), \tag{4.20a}$$

$$\chi(t_0) = \mathrm{col}_{e\in\mathbb{E}_I}(\zeta_0(p_e)), \quad \forall p_e \in \mathcal{P}_I, \tag{4.20b}$$

where $r(\cdot)$ is the source/sink and reaction term with incomplete argument list to be determined depending on the application of the equation.

## 4.6 Estimator for Sea Ice Concentration

To be able to estimate the sea ice concentration we need a dynamic model that can describe the drift of the sea ice. The physics of sea ice is described in Leppäranta (2011). This description includes the dynamic sea ice model, which consists of two elements: *conservation of momentum* and *conservation of ice*. These elements describe in detail how the ice interact with the water, the surrounding ice, et cetera. In our application we argue that a low-fidelity description is more appropriate

because we consider a relatively small spatial scale (kilometers) and short time horizon. We assume that the velocity field of the water are known and that ice floes are carried in steady-state with the water, that is, without velocity relative to the water current. Hence, the conservation of momentum is not necessary to include in our sea ice description. The remaining element *conservation of ice* is modeled by the ADR equation, which we presented in the previous section.

Let $\phi(t,p)$ be the ice concentration to model for $p \in \overline{\Omega}$ with the tessellation $F(\Omega_\phi, N_\phi)$ and $p_e \in \mathcal{P}_I^\phi \cup \mathcal{P}_D^\phi$. We abuse notation and write the analogous discrete counterparts $\phi(t) : \mathbb{T}_{t_0}^{t_f} \to \mathbb{R}^{|\mathbb{E}_I^\phi|}$ and $\phi_{\Gamma_D}(t) : \mathbb{T}_{t_0}^{t_f} \to \mathbb{R}^{|\mathbb{E}_D^\phi|}$. The concentration is taken as the area fraction of ice in a control area with the dimensionless unit $\mathrm{m}^2\,\mathrm{m}^{-2}$. There is a process noise source and some minimal diffusion. The resulting differential equation is

$$M(v)\dot{\phi}(t) = (A(v) - \epsilon_\phi D)\phi(t) + B(v)\phi_{\Gamma_D}(t) + w(t), \tag{4.21a}$$

$$\phi(t_0) = \phi_0, \tag{4.21b}$$

where $v(t)$ is the ice drift velocity and $w(t) \sim (0, Q(t))$ is process noise.

### 4.6.1 Batch-Sequential Kalman Filter

We are interested in performing state and parameter estimation of (4.21) using a Kalman filter. Define the state and parameter estimates $\mathrm{E}(\phi(t)) = \hat{\phi}(t)$ and $\mathrm{E}(\phi_{\Gamma_D}(t)) = \hat{\phi}_{\Gamma_D}(t)$. The corresponding estimation errors are

$$\tilde{\phi}(t) = \phi(t) - \hat{\phi}(t), \tag{4.22a}$$

$$\tilde{\phi}_{\Gamma_D}(t) = \phi_{\Gamma_D}(t) - \hat{\phi}_{\Gamma_D}(t), \tag{4.22b}$$

Define the augmented state vector $z(t) := \mathrm{col}(\phi, \phi_{\Gamma_D})$, $\tilde{z}(t) = z(t) - \hat{z}(t)$, and the estimation error covariance

$$P(t) = \mathrm{cov}(\tilde{z}(t), \tilde{z}(t)), \tag{4.22c}$$

where we note that the covariance $P_\phi(t)$ of $\tilde{\phi}(t)$ is part of $P(t)$ (for later utilization).

The matrices in (4.21) are sparse. The inverse of $M$ may be dense, so we refrain from inverting the matrix to keep the sparse structure. We assume that $\phi_{\Gamma_D}(t)$ is constant or slowly-varying and write the augmented system matrices

$$\overline{M}(v) = \mathrm{bdiag}(M(v), I_{|\mathbb{E}_D^\phi|}), \tag{4.23a}$$

$$\overline{A}(v) = \begin{bmatrix} A(v) - \epsilon_\phi D & B(v) \\ 0_{|\mathbb{E}_D^\phi| \times |\mathbb{E}_I^\phi|} & 0_{|\mathbb{E}_D^\phi| \times |\mathbb{E}_D^\phi|} \end{bmatrix}. \tag{4.23b}$$

The augmented state dynamics along the predicted profiles $\hat{\phi}(t)$ and $\hat{\phi}_{\Gamma_D}$ is

$$\overline{M}(v)\dot{\hat{z}}(t) = \overline{A}(v)\hat{z}. \tag{4.23c}$$

The Riccati differential equation of the augmented system (4.23c), which is used in the hybrid Kalman filter (see for instance Simon (2006)), can be written without inverting $\overline{M}(v)$ as

$$\overline{M}\dot{P}(t)\overline{M}^\mathsf{T} = \overline{A}P(t)\overline{M}^\mathsf{T} + \overline{M}P(t)\overline{A}^\mathsf{T} + \overline{M}Q_z(t)\overline{M}^\mathsf{T}, \tag{4.24a}$$

where we have omitted the arguments of $\overline{M}(v)$ and $\overline{A}(v)$, and

$$Q_z(t) = \mathrm{bdiag}(Q(t), Q_{\phi_{\Gamma_D}}(t))$$

is the augmented spectral density. The above matrix differential equation, which is equipped with an appropriate initial condition

$$P(t_k|t_k) = P_{t_k}, \tag{4.24b}$$

has to be solved between measurement instants. This can for instance be achieved by formulating the initial value problem (IVP) as an implicit equation using collocation in time. Then, solving the implicit equation for the collocated $P$ gives the covariance state trajectory (see e.g. Biegler (2010) for details on collocation).

**Remark 4.1.** If the ice drift velocity and the process noise covariance are both constant, we get time-invariant covariance dynamics. We rewrite (4.24a) into explicit linear form as follows. First, invert $\overline{M}$. Next, exploit the properties defined in e.g. Horn et al. (1994): $\mathrm{vec}(AXB) = (B^\mathsf{T} \otimes A)\,\mathrm{vec}\,X$ and $I_a \otimes A + B \otimes I_b = A \oplus B$, where $\otimes$ and $\oplus$ are the Kronecker product and sum. This results in the linear time-invariant system

$$\mathrm{vec}\,\dot{P} = \left(\overline{M}^{-1}\overline{A} \oplus \overline{M}^{-1}\overline{A}\right)\mathrm{vec}\,P + \mathrm{vec}\,Q_z, \tag{4.25}$$

which can be solved exactly between measurement instants by utilizing the matrix exponential function $e^A$ as described in for instance C.-T. Chen (1999).

**Remark 4.2.** It is well known that the Kalman filter quickly becomes a computational burden for large-scale systems and for instance an ensemble Kalman filter (Evensen, 1994) may be preferable with respect to computational speed. Nevertheless, we stick to the computational inferior choice and proceed with the understanding that we must operate with a moderate number of states.

Let $C_{m,-1}(t, v, \varrho_m(t), \psi_m(t))$ be the $|\mathbb{E}_I^\phi| \times |\mathbb{E}_I^\phi|$ measurement matrix for sensor $m$ created with non-smooth sampling functions. Since a mobile sensor is unable to measure all the states at a given time instant, the measurement matrix will have rows with only zeros. To more efficiently calculate the Kalman gain, we propose to select the submatrix without zero-rows and the corresponding rows and columns of the measurement spectral density matrix $R_m(t)$. This action can be justified by acknowledging that the measurement noise is infinity for states that are not measured. Let $C_{m,\subset}(t)$ and $R_{m,\subset}(t)$ denote the resulting submatrices. It is worth pointing out that these matrices may change dimensions from one measurement to the next, but since measurements are received at discrete time instants $t_{k+1}$ and employed accordingly, this fact does not affect the a posteriori Kalman filter updating.

Different mobile sensors may measure the same state variables at the same time. This occurrence complicates the state estimate and covariance update step of the Kalman filter. We use an approach that we call *batch-sequential* Kalman filter, where the estimates are updated sequentially, one measurement vector at

the time, similar to the method described in Simon (2006, Section 6.1). Define the initial estimate and covariance in the sequential filter as the a priori estimates

$$\hat{z}_0(t_{k+1}) = \hat{z}(t_{k+1}|t_k), \tag{4.26a}$$
$$P_0(t_{k+1}) = P(t_{k+1}|t_k). \tag{4.26b}$$

Let the augmented measurement matrix for sensor $m$ be

$$\overline{C}_{m,\subset}(t) = \begin{bmatrix} C_{m,\subset}(t) & 0 \end{bmatrix}, \tag{4.27}$$

so that it is consistent with the augmented state vector. When measurements are received at time $t_{k+1}$ we calculate for each $m \in \mathbb{M}$

$$K_m = P_{m-1}\overline{C}_{m,\subset}^{\mathsf{T}}(\overline{C}_{m,\subset}P_{m-1}\overline{C}_{m,\subset}^{\mathsf{T}} + R_{m,\subset})^{-1}, \tag{4.28a}$$
$$\hat{z}_m = \hat{z}_{m-1} + K_m(y_m(t_{k+1}) - \overline{C}_{m,\subset}\hat{z}_{m-1}), \tag{4.28b}$$
$$P_m = (I - K_m\overline{C}_{m,\subset})P_{m-1}(I - K_m\overline{C}_{m,\subset})^{\mathsf{T}} + K_m R_{m,\subset}K_m^{\mathsf{T}}, \tag{4.28c}$$

where $y_m(t_{k+1})$ is the measurement vector from sensor $m$. The a posteriori estimates are

$$\hat{z}(t_{k+1}|t_{k+1}) = \max(0_{N_\phi \times 1}, \min(\hat{z}_{|\mathbb{M}|}, 1_{N_\phi \times 1})), \tag{4.29a}$$
$$P(t_{k+1}|t_{k+1}) = P_{|\mathbb{M}|}. \tag{4.29b}$$

where the state estimates are clipped to be within $[0, 1]$. We do this to avoid unphysical concentration estimates. For a single sensor the batch-sequential Kalman filter is identical to a standard Kalman filter.

**Remark 4.3.** In the case where the measurement supports of the sensors are disjoint, there is no need to perform sequential updates of the estimates and the estimation error covariance; All measurements can be collected into a single measurement vector with corresponding measurement matrix and then proceed as in a standard Kalman filter update.

### 4.6.2 Downsampling High-Resolution Measurements

When fusing measurements $y(t)$ with the model, the measurements have to be represented at the discretized locations. Often, measurements have finer spatial resolution than the set of nodes that constitute the discretized representation. For instance, sea ice images from aerial mobile sensors have much finer resolution than the ODE describing the concentration. We can treat the image as a continuum and use quadratures similar to the method in Section 4.5.1. In cases where the image exhibits rapid variation of the measured quantity, very high degree quadratures for each $K_e$ are needed to get a good approximation. We propose to use a different approach where the quantity in a region surrounding the node $p_e \in \Omega$ is represented in a single value. Downsampling using pixel averaging is a common image processing technique that we intend to use. More sophisticated image processing techniques for ice concentration can be found in Zhang et al. (2012).

We assume that the input images have been pre-processed into a binary image (i.e. $\{\text{water} = 0, \text{ice} = 1\}$) and transformed into the $\{\text{adr}\}$ coordinate system. Let the image function provided by mobile sensor $m$ be

$$\mathcal{I}_m(t,p) : \mathbb{T}_{t_0}^{t_f} \times \text{supp}(w_{\mathcal{C}^{-1}}(t, \varrho_m, p, \psi_m)) \to \{0,1\}. \tag{4.30}$$

**Definition 4.3** ((Du et al., 1999))**.** Given a set of points $\{z_i\}_{i=1}^r : z_i \in \overline{\Omega}$, called generators, the *Voronoi tessellation* of $\Omega$ is defined by the family of sets $F_V(\Omega, r) = \{V_i\}_{i\in\mathbb{I}_r}$ where region $V_i$ belonging to $z_i$ is defined as

$$V_i := \{x \in \Omega : \forall j \in \mathbb{I}_r, j \neq i,\ \|x - z_i\|_2 < \|x - z_j\|_2\}. \tag{4.31}$$

We can see that all points in a Voronoi cell $V_i$ is closer to $z_i$ than any other point $z_j$. Hence, $V_i$ is a sensible region to find an averaged concentration value for the point $z_i$.

We use the points $p_e \in \mathcal{P}_I^\phi \cup \mathcal{P}_D^\phi$ as generators for the Voronoi tessellation $F_V(\Omega_\phi, N_\phi)$. Define the measurement support of the mobile sensor $m$ at $t = t_{k+1}$ as

$$\Omega_{m,\text{FOV}} := \{x \in \Omega : x \in \text{supp}(w_{\mathcal{C}^{-1}}(t_{k+1}, \varrho_m, x, \psi_m))\}. \tag{4.32}$$

Let $\mathbb{E}_{m,\text{FOV}} := \{e \in \mathbb{I}_{N_\phi} : \exists p_e \in \mathcal{P}_I^\phi, p_e \in \Omega_{m,\text{FOV}}\}$ be the indices of the nodes contained in the field of view of sensor $m$. We denote $\forall i \in \mathbb{E}_{m,\text{FOV}}$

$$V_i^{m,\text{FOV}} = V_i \cap (\Omega_{m,\text{FOV}}), \tag{4.33}$$

as the corresponding (possibly clipped) Voronoi cells.

The average intensity in a clipped cell is the measured concentration. For the ordered pair $(i,j)$ with $i \in \mathbb{E}_{m,\text{FOV}}$ and $j \in \mathbb{I}_{|\mathbb{E}_{m,\text{FOV}}|}$ we write the $j$th element of the measurement vector $y_m(t_{k+1}) \in \mathbb{R}^{|\mathbb{E}_{m,\text{FOV}}|}$ as

$$y_{m,j}(t_{k+1}) = \frac{1}{|V_i^{m,\text{FOV}}|} \int_{V_i^{m,\text{FOV}}} \mathcal{I}_m(t_{k+1}, p)\, dp. \tag{4.34}$$

The measurement vector now contains averaged ice concentration fractions in the range $[0,1]$ for all the discrete points covered by the field of view of the corresponding mobile sensor. $y_m(t_{k+1})$ is used in the correction step (4.28b). Figure 4.4a displays a Delaunay tessellation of an annular sector including the Voronoi cells for each node point. In Figure 4.4b we can see the results of pixel averaging of an ice field over each of the Voronoi cells. The same figure also displays the field of view of a sensor including the measured cells. In this particular example the measurement vector returns five measurements.

## 4.7 Reduced Uncertainty Dynamics

In Haugen et al. (2014b) the trace of the estimation error covariance matrix was used as a performance measure in the path planning optimization problem. The objects being monitored were independent, so the resulting Riccati differential equations had limited dimensions and could be solved without much difficulty as part

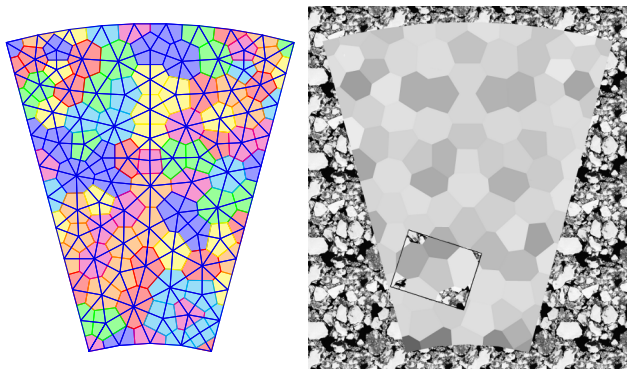

**(a)** **(b)**

**Figure 4.4** (a) A Delaunay tessellation of an annular sector and the corresponding Voronoi cells; (b) An ice field downsampled over the Voronoi cells with pixel averaging. The field of view of a sensor and the corresponding measured cells are also shown.

of the optimization problem. In this manuscript, however, the Riccati differential equation (4.24a) has many more states and quickly becomes a computational burden if included in the optimization problem. To overcome this issue, we propose a simplified description of the uncertainty dynamics when performing the path planning. In particular, we apply the ADR equation from Section 4.5 as a drifting quantity of uncertainty that can be influenced by the mobile sensor network. This simplification is motivated by our intuition that the uncertainty moves together with the ice and if a mobile sensor visits a region, the uncertainty reduces in that region.

### 4.7.1 The Source/Sink and Reaction Term

In order to describe the reduced uncertainty dynamics, we further extend the ADR equation of Section 4.5 by introducing two new terms:

(i) Stabilizing reaction.
(ii) Vehicle-dependent source.

The stabilizing reaction mimics the behavior of reducing the uncertainty of regions the mobile sensors visit. The vehicle-dependent source accommodate the increasing uncertainty of regions not being visited. This term also has a limited influence on distant regions for the mobile sensors. The latter property is desired because our implementation of the optimization problem benefits from it. A very similar property was more thoroughly discussed and motivated in Haugen et al. (2014b).

**Assumption 4.2.** *To simplify exposition, the reference frames* $\{adr\}$ *and* $\{ned\}$ *are identical, so there is no need for transforming between coordinate systems.*

**Stabilizing Reaction**

Suppose we are interested in controlling our quantity to a desired level $\zeta_d(p) \in L^2(\Omega)$. In this context our mobile sensors act as mobile actuators with the field of view as actuator support. Define $\tilde{\zeta}(t,p) = \zeta(t,p) - \zeta_d(p)$. For sensor $m$ with position $\varrho_m(t)$ and orientation $\psi_m(t)$, consider $\forall p \in \Omega$

$$s_{m,1}(t, \varrho_m, p, \psi_m, \zeta) = -\gamma_m(p) w_{\mathcal{C}^\infty}(t, \varrho_m, p, \psi_m)\tilde{\zeta}(t,p), \tag{4.35}$$

where $\gamma_m(p) \in L^2(\Omega)$ is positive and $w_{\mathcal{C}^\infty}$ is the $\mathcal{C}^\infty$ sampling function defined in Section 4.4.2. This reaction drives $\zeta(t,p)$ toward $\zeta_d(p)$ for all unit volumes within the support $\text{supp}(w_{\mathcal{C}^\infty})$ of the sensor. The magnitude of the reaction depends on both $\gamma_m$ and the weight $w_{\mathcal{C}^\infty}$, for which the latter approaches zero as the distance between a unit volume and the sensor increases.

Let $\chi_d := \text{col}_{e\in\mathbb{E}_I}(\zeta_d(p_e))$, $\forall p_e \in \mathcal{P}_I$, so that $\tilde{\chi}(t) = \chi(t) - \chi_d$. Define $q(t) := \text{col}_{m\in\mathbb{M}}(\varrho_m(t))$ and $\Psi(t) := \text{col}_{m\in\mathbb{M}}(\psi_m(t))$. The weak form of (4.35) can be obtained by substituting $s_{m,1}$ for $s_e$ in (4.19d). We do this for all sensors $m \in \mathbb{M}$ and obtain the expression

$$r_1(t, v, \chi, q, \Psi) = -\sum_{m\in\mathbb{M}} \mathcal{L}_m C_{m,\infty}(t, v, \varrho_m, \psi_m)\tilde{\chi}(t), \tag{4.36}$$

where in this case $\mathcal{L}_m \in \Pi_{|\mathbb{E}_I|}$ is a design matrix that depends on $\gamma_m$.

**Vehicle-Dependent Source**

Define a source $\sigma(t,p) \in L^\infty(\mathbb{T}_{t_0}^{t_f}; L^\infty(\Omega))$ that covers the whole domain $\Omega$. We seek to make the source dependent on the location of the sensor. In particular, the mobile sensors influence the creation rate of the quantity at a unit volume $p \in \Omega$ even if it is located such that reaction presented in the previous section is negligible. We construct the source such that the closer a mobile sensor is to a location, the weaker the source. We get $\forall m \in \mathbb{M}$

$$s_2(t, q, p, \Psi) = \frac{1}{|\mathbb{M}|} \sum_{m\in\mathbb{M}} \left(1 - w_{\mathcal{C}^\infty}(t, \varrho_m, p, \psi_m)\right) \sigma(t,p). \tag{4.37}$$

Let $\chi_\sigma(t) := \text{col}_{e\in\mathbb{E}_I}(\sigma(t,p_e)$, $\forall p_e \in \mathcal{P}_I$. The corresponding discretized weak form is

$$r_2(t, v, q, \Psi; \chi_\sigma) = \frac{1}{|\mathbb{M}|} \sum_{m\in\mathbb{M}} W_{m,\infty}(t, v, \varrho_m, \psi_m)\chi_\sigma(t), \tag{4.38}$$

where we see that in the case of a single sensor the source magnitude vanish at a unit volume when the sensor is sufficiently close to it.

### 4.7.2 Reduced Uncertainty Dynamics

The quantity of interest is $\nu(t,p)$, which is the approximated variance of the ice concentration at the unit volume $p \in \Omega_\cap$. Again, by abusing notation we write the

discretized variance as $\nu(t) : \mathbb{T}_{t_0}^{t_f} \to \mathbb{R}^{|\mathbb{E}_I^\nu|}$. To facilitate computational tractability, $\nu(t)$ is discretized into much fewer states than $\phi(t)$, with the coarser tessellation $F(\Omega_\cap, |\mathbb{E}_I^\nu| + |\mathbb{E}_D^\nu|)$, so the nodes in $\mathcal{P}_I^\nu$ generally do not coincide with any points in $\mathcal{P}_I^\phi$.

We employ the previously defined reaction and source terms (4.36) and (4.38) with appropriate dimensions and get the discretized uncertainty ADR equation

$$\begin{aligned} M_\nu(v)\dot{\nu}(t) &= (A_\nu(v) - \epsilon_\nu D_\nu)\nu(t) + B_\nu(v)\nu_{\Gamma_D} \\ &\quad + r_1(t, v, \nu, q, \Psi) + r_2(t, v, q, \Psi; \nu_\sigma), \qquad (4.39a) \\ \nu(t_0) &= \nu_0, \qquad (4.39b) \end{aligned}$$

where $\nu_{\Gamma_D} \in \mathbb{R}_{\geq 0}^{|\mathbb{E}_D^\nu|}$ is a provided inlet uncertainty, $\tilde{\nu} = \nu$, and $\nu_0$ is sampled from the variance estimation error of the Kalman filter (4.28c). Let $\nu_\phi(t) := \mathrm{diag}(P_\phi(t))$ and recall from (4.15) that a quantity at an arbitrary location can be sampled from a linear combination of the finite dimensional approximation. Since we are downsampling, local maxima may be lost if we only sample at the coarse locations $\mathcal{P}_I^\nu$. To avoid loss of maxima, we assign the variance at each coarse node point as the local maximum. The local maximum is set to the maximum variance of all fine nodes points within the Voronoi cell that belongs to the corresponding coarse point. More precisely, use $p_e \in \mathcal{P}_I^\nu \cup \mathcal{P}_D^\nu$ as generators for the coarse Voronoi tessellation $F_\nu^\cap(\Omega_\cap, |\mathbb{E}_I^\nu| + |\mathbb{E}_D^\nu|)$ with the Voronoi cells $V_i^\cap$ belonging to the $i$th state variable $\nu_{0,i}$. Further, we define the index set of points from the fine tessellation within $V_i^\cap$ as $\mathbb{E}_i^\cap := \{e \in \mathbb{I}_{N_\phi} : \exists p_e \in \mathcal{P}_I^\phi, p_e \in V_i^\cap\}$. Then for each $i \in \mathbb{I}_{|\mathbb{E}_I^\nu|}$ we have

$$\nu_{0,i} = \max_{e \in \mathbb{E}_i^\cap}(\nu_{\phi,e}), \qquad (4.40)$$

where $\nu_{\phi,e}$ is the $e$th row of $\nu_\phi$.

## 4.8 Path Planning

### 4.8.1 Dynamic Optimization Problem

The optimization problem is to minimize $\nu(t)$ using the mobile sensor network. We choose an appropriate region $\Omega_\cap$ and formulate the regional surveillance as a Bolza-type OCP. Let $\mathbb{T}_{t_0}^{t_f}$ denote the horizon of interest. The decision variables are $\forall m \in \mathbb{M}$ the control inputs $u_m(t)$. Define $u(t) := \mathrm{col}_{m\in\mathbb{M}}(u_m(t))$, $\Lambda(t) := \mathrm{bdiag}_{m\in\mathbb{M}}(\Lambda_m(t))$, and $\Xi(t) := \mathrm{bdiag}_{m\in\mathbb{M}}(\Xi_m(t))$, where $\Lambda(t) \in \Pi_{|\mathbb{M}|}$ and $\Xi(t) \in \Pi_{|\mathbb{M}|}$ are time-varying design matrices. Define the Lagrange term as

$$\Phi_L(t, u) = \int_{t_0}^{t_f} \nu^\mathsf{T}(t) G_L(t) \nu(t) + \frac{du}{dt}^\mathsf{T} \Lambda(t) \frac{du}{dt} + u^\mathsf{T} \Xi(t) u \, dt, \qquad (4.41a)$$

where $G_L(t) \in \Pi_{n_\nu}$ is a user-defined matrix.

We define the Mayer term as

$$\nu^\mathsf{T}(t_f) G_M \nu(t_f), \qquad (4.41b)$$

where $G_M \in \Pi_{n_\nu}$ is a design matrix.

The optimization problem is to minimize (4.41) constrained by the mobile sensor network, its collision avoidance, and the simplified uncertainty dynamics. That is, $\forall t \in \mathbb{T}_{t_0}^{t_f}$, $\forall (i,j) \in E, \forall m \in \mathbb{M}$:

$$\min_{u} \quad \Phi_L(t,u) + \Phi_M(t_f) \tag{4.42a}$$

$$\text{s. t.} \quad (4.3), (4.4), (4.39). \tag{4.42b}$$

The solution to (4.42) provides us with optimal mobile sensor trajectories, denoted for each $m \in \mathbb{M}$ as

$$x_m^\star(t) \in \mathcal{K}_m \times \mathbb{S},\ t \in \mathbb{T}_{t_0}^{t_f}. \tag{4.43}$$

### 4.8.2 Receding Horizon

For a real-world operation with some duration, the optimization problem (4.42) quickly becomes computationally intractable. To remedy this challenge, we solve the optimization problem using a receding horizon. This design decision comes with two added benefits; The modeling inaccuracies of the approximated drifting uncertainty field are removed at every re-optimization, and changes in ambient conditions may be promoted through adaptive behavior in the formulation of the optimization problem. In particular, updating parameters such as drift velocity and changing monitoring region $\Omega_\cap$ are straightforward.

Let $\mathbb{T} := [t_0, T]$ be the interval in which the objective of estimating the ice concentration finds place. We partition the time line into $k_t \in \mathbb{N}^+$ strictly overlapping intervals, where $\mathbb{T}_k := [t_{0,k}, t_{f,k}]$ is the $k$th interval. The interval of interest is contained within the overlapping intervals: $\mathbb{T} \subset \bigcup_{k \in \mathbb{I}_{k_t}} \mathbb{T}_k$. Two consecutive intervals overlap such that $t_{0,k} < t_{0,k+1} < t_{f,k}$. The non-overlapping part $\mathbb{T}_k \setminus \mathbb{T}_{k+1}$ is considered the utilization interval of the $k$th iteration. By this we mean the time interval in which we utilize the planned path found from the $k$th optimization problem.

The mechanism of an iteration can be divided into a three-step procedure of *collecting, optimizing*, and *utilizing*. Consider the $k$th iteration. The *collecting* step is performed by mobile sensors and provided to the *Estimator* for state and parameter estimation. At time $t_{0,k-1}$ all the collected measurements are used in finding the best estimates of the drifting field and mobile sensor states of interest. An open-loop prediction forward in time is executed to accommodate the formulation of the $k$th optimization problem. This open-loop prediction consists of finding the expected closed-loop behavior of the mobile sensors and its expected influence on the low-fidelity uncertainty field (4.39) in the interval $[t_{0,k-1}, t_{0,k}]$. The goal is to determine relevant initial conditions at $t_{0,k}$. Details on how to do this are provided in Haugen et al. (2014b). The *optimizing* step is executed by the *Path Planner* component and involves formulating and solving (4.42) to provide the desired trajectories (4.43). The final step is to deliver the desired paths (4.43) to the RPAS, so that it can be *utilized* in collecting more information.

The three steps of the procedure execute concurrently with earlier and later time steps: when the monitoring system is optimizing for the $k$th iteration, it is collecting for iteration $k+1$, and utilizing iteration $k-1$. Figure 4.5 illustrates the three-step procedure.

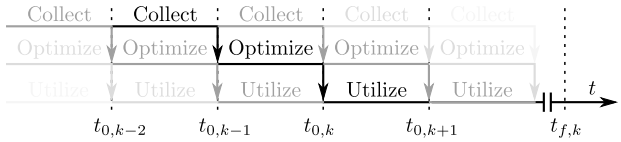


**Figure 4.5** The monitoring systems consists of a three-step procedure of collecting, optimizing, and utilizing.

### 4.8.3 Implementation

To efficiently solve the OCP (4.42), we choose a direct transcription approach where both the state and control variables are discretized into a finite-dimensional NLP problem. The simultaneous collocation of finite elements is used to obtain Lagrange interpolation polynomial descriptions of the state variables. The control input is piecewise constant, whereas the states are described using K-point Radau collocation, for details consult Biegler (2010).

The resulting large-scale NLP formulation benefits from being sparse and having structure. These properties can be exploited using an efficient NLP solver. We formulate the problem in the symbolic framework CasADi (Andersson et al., 2012), which provides the necessary derivative information required by the NLP solver. The CasADi library contains an interface for the primal-dual interior-point NLP solver IPOPT (Wächter et al., 2006). IPOPT is compiled with OpenBLAS (Xianyi et al., 2012) and the linear algebra sparse direct solver MA57 (HSL, 2011).

Tessellation of region geometries were performed using Gmsh (Geuzaine et al., 2009), where we used Delaunay triangulation. Image processing such as pixel averaging, translation, and image masking were performed with the aid of OpenCV (Bradski, 2000).

Initial desired paths are provided a priori because paths need to be available when the first optimization is running. We provide control inputs that ensure collision avoidance and feasible execution within the constrained region. The performance of the discretized optimization problem benefits from good initial conditions. We initialize the uncertainty field variables by solving the matching IVPs with expected closed-loop behaviors of the sensors given their respective initial conditions. Since a new optimization horizon goes beyond the previous, we use the previous iterations final control input as extrapolation.

## 4.9 Case Study

### 4.9.1 Setup

We are interested in performing estimation of ice concentration in an annular sector. As our real-world simulator we construct an artificial ice field using the image displayed in Figure 4.6a. The ice texture is repeated horizontally and vertically sufficiently many times to allow a periodic, but seamless ice field. The ice field is equipped with a constant north-to-south uniform drift velocity $v = \mathrm{col}(-1.5, 0)$ m. The field exhibits no diffusion, only transport of ice concentration. Figure 4.6b is the same field the after binary thresholding used in the image processing part

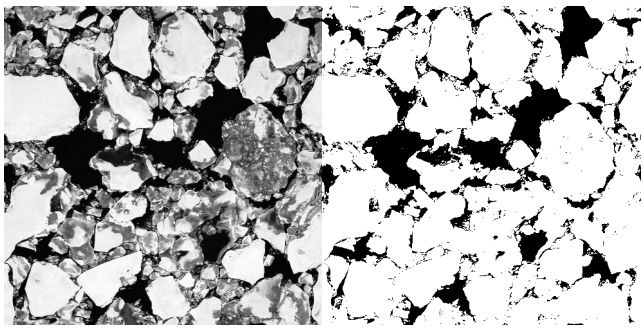

**(a)** **(b)**

**Figure 4.6** (a) 8-bit grayscale ice image of $800 \times 800$ pixels used in the case study. The image has manually been turned into a seamlessly tiled texture by blending edges in a photo editing software; (b) Same image with binary thresholding with cutoff at normalized intensity 0.157.

of the simulation. The real-world ice field is simulated by simply translating the image given its drift velocity and the ground sample distance of a pixel.

We let all the mobile sensors operate at the same altitude of 400 m and simulate that they are equipped with pitch and roll stabilized downward-looking optical devices. In particular, the mobile sensors have measurement capability similar to FLIR's thermal infrared camera Tau 2 (FLIR, 2013) with a 9 mm lens and a detector pitch of 17 µm and a $640 \times 512$ detector array. This gives a field of view of 550 m$\times$ 425 m at the specified altitude and an average ground sample distance of 0.86 m.

**Remark 4.4.** Our ice field simulator has fixed pixel orientation and geometry. The pixels are aligned with the detector when obtaining ice images using the mentioned optical device. Since we only use the field of view of the camera when sampling from our simulator, the pixels do not have truly realistic orientation or geometry.

The annular sectors we are interested in can be described by the circle center, minor and major radii, sector midpoint angle, and sector opening angle. The major circular arc is the inlet (Dirichlet) boundary, whereas the remaining boundaries are outlet (Neumann) boundaries. A benefit of using an annular sector is that ice drift velocity has an orientation range robustness equal to the opening angle without having to deal with time-varying boundary condition sets.

We distinguish between the finely and coarsely tessellated annular geometries. The former is used in the estimator and the latter in the optimization problem. The number of tessellation volumes is determined by adjusting the characteristic length $\ell$ in the Delaunay triangulation algorithm. The parameters defining the geometries and the tessellations are given in Table 4.1, with corresponding tessellations shown in Figure 4.7. The coarse geometry has a slightly larger major radius, so that the vertices of the fine tessellation are contained by the coarse one.

We define a single operational region $\mathcal{K}$ for all the mobile sensors. This region contains the annular sector and is indicated in the coming north-east plots.

**Table 4.1** Parameter values for the tessellated geometries. Recall that {adr} is aligned with {ned}.

**(a)** Fine tessellation.

| Parameter | Value |
|---|---|
| Circle center [km] | $[-1.6, 0]^\mathsf{T}$ |
| Minor radius | 1700 m |
| Major radius | 4000 m |
| Sector opening | 30° |
| Sector midpoint | 0° |
| $\ell_\phi$ | 210 m |
| Triangles | 163 |
| $\lvert\mathbb{E}_I^\phi\rvert$ | 89 |
| $\lvert\mathbb{E}_D^\phi\rvert$ | 10 |
| Quadrature degree | 2-by-2 |

**(b)** Coarse tessellation.

| Parameter | Value |
|---|---|
| Circle center [km] | $[-1.6, 0]^\mathsf{T}$ |
| Minor radius | 1700 m |
| Major radius | 4100 m |
| Sector opening | 30° |
| Sector midpoint | 0° |
| $\ell_\nu$ | 550 m |
| Triangles | 24 |
| $\lvert\mathbb{E}_I^\nu\rvert$ | 15 |
| $\lvert\mathbb{E}_D^\nu\rvert$ | 4 |
| Quadrature degree | 2-by-2 |

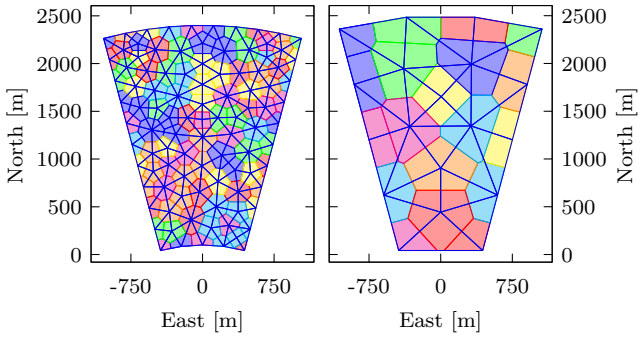


**(a)** Finely tessellated. **(b)** Coarsely tessellated.

**Figure 4.7** Tessellated annular sectors including their belonging Voronoi cells.

The mobile sensor network consists of identical mobile sensors with bounded bank angle $u_{m\in\mathbb{M}}(t) \in \mathcal{U} = [-0.35, 0.35]$. The initial conditions are $x_1(t_0) = \mathrm{col}(0, -500, 0)$ and $x_2(t_0) = \mathrm{col}(0, 500, 0)$, with $t_0 = 0\,\mathrm{s}$. Collision avoidance is required to be enforced with exclusion balls that have radii 500 m. The standard gravity $g$ was set to $9.81\,\mathrm{m\,s^{-2}}$, vehicle airspeeds $V_a = 10\,\mathrm{m\,s^{-1}}$, and the wind speeds to zero. The field of view of the mobile sensors are dictated by the assumed optical devices, and using the notation in (4.6) we have $\Delta_{x_1} = 212.5\,\mathrm{m}$ and $\Delta_{x_2} = 275\,\mathrm{m}$.

The ice drift estimation is model as described by (4.23) with $\epsilon_\phi = 10^{-4}$ and $\tau = 0$. The initial state and boundary estimates for the ice concentration are $\hat{\phi}(t_0) = 0.3 \times 1_{|\mathbb{E}_I^\phi|\times 1}$ and $\hat{\phi}_{\Gamma_D}(t_0) = 0.3 \times 1_{|\mathbb{E}_D^\phi|\times 1}$. The estimation error covariance is set to $P(t_0|t_0) = \mathrm{bdiag}(10I_{|\mathbb{E}_I^\phi|}, 10I_{|\mathbb{E}_D^\phi|})$. We set the process noise matrix to

$Q_z = \text{bdiag}(0.05I_{|\mathbb{E}_I^\phi|}, 0.05I_{|\mathbb{E}_D^\phi|})$. We assume that the measurements arrive in an orderly manner every 3.5 s. The measurement noise matrices are assumed to be diagonal with the same variance whenever available, that is $R_{jj} = 5 \times 10^{-5}$.

The uncertainty field is initialized as described in Section 4.8.2 with the additional modification that $\nu_{\Gamma_D} \equiv 1_{|\mathbb{E}_D^\nu| \times 1}$ and

$$\bar{\nu} = \frac{\nu}{\max_{i \in |\mathbb{E}_I^\nu|}(\nu_i)}, \tag{4.44}$$

which is the scaled uncertainty used in initializing the open-loop prediction. This scaling ensures that the uncertainty in the optimization problem has a bounded magnitude regardless of the variance magnitude in the estimator. The stabilizing gain is $\gamma = 0.1$, the source magnitude $\sigma(t,p) = \times 10^{-3}$, $\epsilon_\nu = 10^{-4}$, and $\tau = 183.33$. The measurement model for $r_1(\cdot)$ in (4.39) is as described in Example 4.1 with $n = 1$ and $K_1 = 5.1 \times 10^{-5} I_2$. Moreover, $r_2(\cdot)$ in (4.39) is also similar with $n = 1$ and $K_1 = 5.2 \times 10^{-7} I_2$.

Each optimization problem is formulated with 2-point Radau over a horizon of 91 s. There are totally 26 finite elements with input blocking over two elements, so the control inputs are piecewise constant divided over 13 elements. The realization duration is 35 s. The monitoring is scheduled to run for 20 optimization horizons.

The uncertainty states close to the boundary outlet at the minor circular arc are considered more important than the upstream states. We reflect this prioritization in the optimization problem by increasing the penalization of uncertainty magnitude close to this boundary outlet compared to upstream states. In particular, we define time-invariant inclined planes $f_{i \in \{L,M\}}(p) : \Omega_\cap \to \mathbb{R}_{>0}$, which are, respectively, the diagonal Lagrange and Mayer weighting at the position $p$. With these definitions, for each ordered pair $(i,e) : i \in \mathbb{I}_{|\mathbb{E}_I^\nu|}, e \in \mathbb{E}_I^\nu$ and $p_e \in \mathcal{P}_I^\nu$, the $i$th diagonal terms are $G_{L,ii} = f_L(p_e)$ and $G_{M,ii} = f_M(p_e)$. Let $f_L(p) = \text{col}(-1/120, 0) \cdot p + 143/6$ and $f_M(p) = \text{col}(-1/160, 0) \cdot p + 245/8$. The remaining parameters for the objective function are $\Lambda = 10 I_{|\mathbb{M}|}$ and $\Xi = 7.5 I_{|\mathbb{M}|}$.

## 4.10 Numerical Results

The same objective were solved in two different cases:

**Case 1.** *With a singular mobile sensor.*

**Case 2.** *With a two-sensor network.*

### 4.10.1 Case 1 Single Sensor

The optimization problems had 1435 variables each. All the sampling intervals solved in due time on a laptop computer. The utilization time is effectively the deadline of each optimization problem and we can see in Figure 4.8 that they solved well within the deadline. None of the commanded control inputs exceeded the required bounds (see Figure 4.9), so the resulting paths are feasible with respect to the prescribed maneuverability constraints of the mobile sensor.

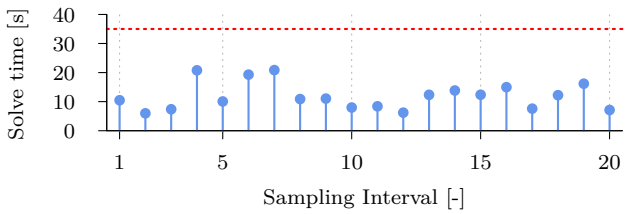


**Figure 4.8** The solve time of each optimization problem is less that the utilization time (i.e. deadline), which is indicated by the dashed line.

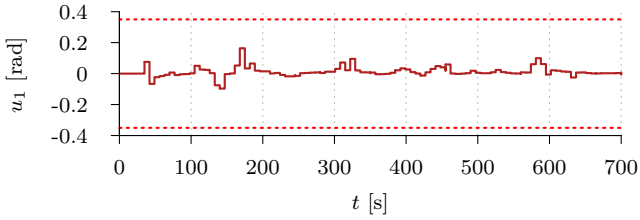


**Figure 4.9** The optimized control input that is used to construct the desired paths for the mobile sensor. The input remains within the upper and lower constraint, which are indicated by dashed lines.

The optimization problems seek to minimize the magnitude of an uncertainty field. The two first optimization horizons together with their respective terminal uncertainty surface snapshots are displayed in Figure 4.10. The aircraft markers indicate the end of the utilization of that particular sampling interval. We can see that the uncertainty decreased wherever the mobile sensor traveled.

Figure 4.11 shows that the 2-normed estimation error $\|\tilde{z}(t)\|_2$ decreased steadily the first 500 s before stabilizing at around $\|\tilde{z}\| \approx 2$. Likewise, the trace of the covariance $\mathrm{tr}(P(t))$ stopped increasing at the same time. In Figure 4.12 we can see snapshots of the estimation error surface together with the executed trajectories. We can clearly see that the estimation error decreases between the three first snapshots. Moreover, the mobile sensor never leaves the operational region.

### 4.10.2 Case 2 Sensor Network

The optimization problems had 1685 variables each. Again, all the optimization problems found optimal solutions, however only 12 of the 20 iterations found a solution in due time, see Figure 4.13. Figure 4.14 indicates that the commanded control inputs respect the upper and lower constraints. The Euclidean distance between the two mobile sensors is never less than 500 m (Figure 4.15), so collision avoidance is enforced.

If we compare the data in Figure 4.11 and Figure 4.16 we see that the estimation error $\|\tilde{z}(t)\|_2$ decreases more rapidly with the use of two mobile sensors. We can also see that the $\mathrm{tr}(P(t))$ never attains the same magnitude as the first case with the use of two mobile sensors. This performance increase is further illustrated in

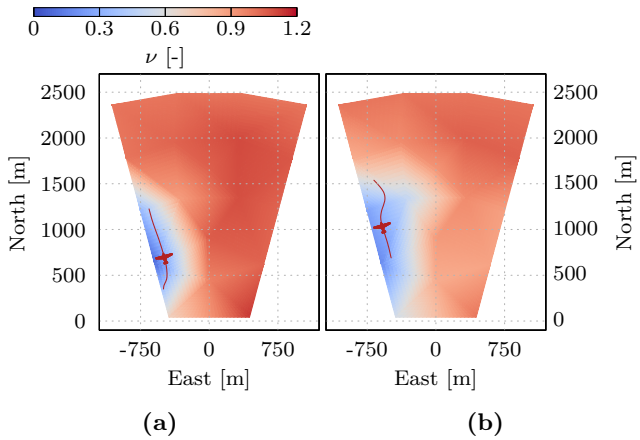


**Figure 4.10** Uncertainty surface snapshots at $t_{f,k}$ resulting from the optimization problems. They include optimized sensor trajectories with duration 91 s. The airplane markers indicate the end of the utilization of the sampling interval ($t_{0,k} + 35$ s): (a) $t_{f,1} = 126$ s; and, (b) $t_{f,2} = 161$ s.

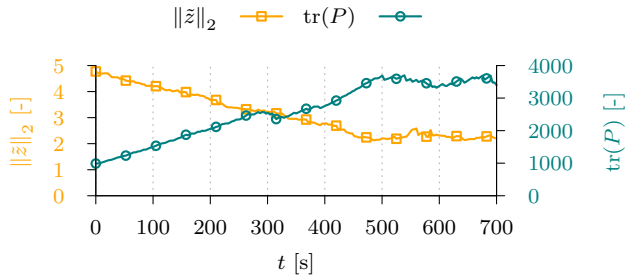


**Figure 4.11** Time series of the 2-normed estimation error $\|\tilde{z}\|_2$ and the trace of the covariance tr($P$) in the case of a single mobile sensor.

Figure 4.17. In particular, the two mobile sensors quickly cover the whole annular sector. We can also see that the mobile sensors never collide or leave the admissible region.

## 4.11 Discussion

The two simulation cases support the expected improved performance of increasing the number of mobile sensors. This improved performance comes at the cost of increased solve times for the optimization problems, and even cases where the optimization problem failed to find a solution in due time. There are several things we can do to deal with this issue. It is helpful to provide good initial guesses for the optimization problems. Regardless of the mechanisms employed, the optimization problems do not have a fixed maximum solve time. For this reason a fail-safe

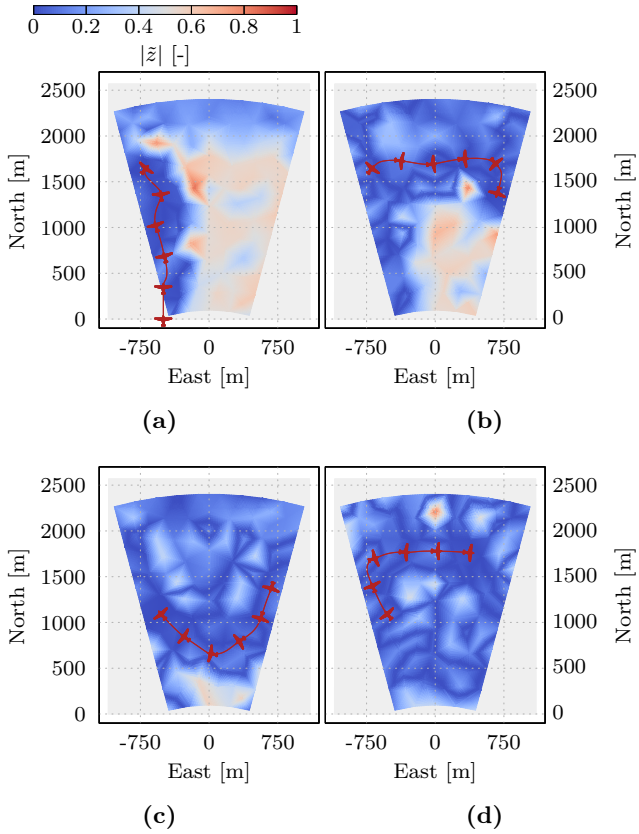


**Figure 4.12** Estimation error surface snapshots with sensor trajectories. The airplane markers indicate the switching of sampling intervals (every 35 s). The gray box is the admissible region:
(a) Trajectory interval $[0, 175]$ s with $|\tilde{z}|$ surface snapshot at 175 s;
(b) Trajectory interval $[175, 350]$ s with $|\tilde{z}|$ surface snapshot at 350 s;
(c) Trajectory interval $[350, 525]$ s with $|\tilde{z}|$ surface snapshot at 525 s; and,
(d) Trajectory interval $[525, 700]$ s with $|\tilde{z}|$ surface snapshot at 700 s.

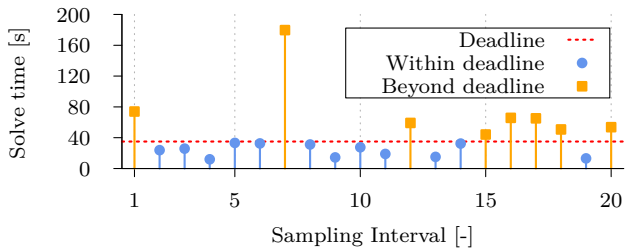


**Figure 4.13** The solve time of each optimization problem. The dashed line is the deadline. 8 optimization problems spent too much time finding the optimal solution.

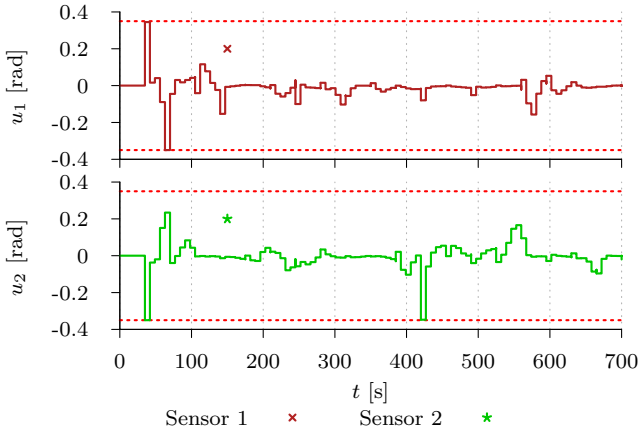


**Figure 4.14** The optimized control inputs that are used to construct the desired paths for the mobile sensors. The inputs remain within the upper and lower constraint, which are indicated by dashed lines.

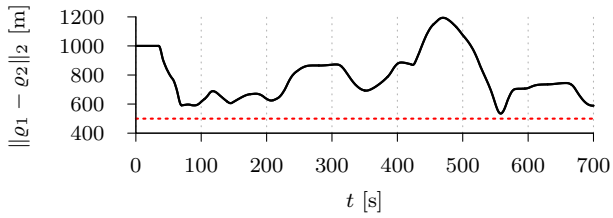


**Figure 4.15** The Euclidean distance between the two mobile sensors. The minimum distance constraint is indicated by the dashed line at 500 m.

mechanism should initialize in the case of failure to find a solution in time. One possible mechanism can for instance be that each aircraft switches to a nominal trajectory that are in distinct regions, e.g. circular paths. The mobile sensors remain in this state until new trajectories are available. This mechanism and recursive

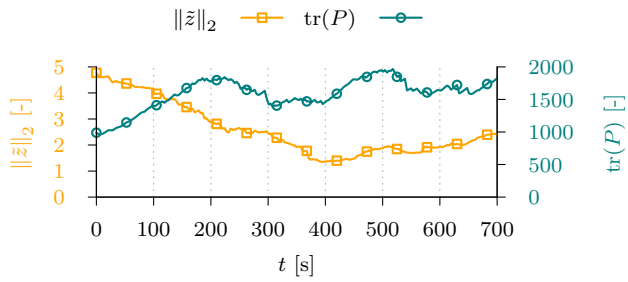


**Figure 4.16** Time series of the 2-normed estimation error $\|\tilde{z}\|_2$ and the trace of the covariance tr$(P)$ in the case of two mobile sensors.

feasibility have briefly been discussed in Haugen et al. (2014b).

Our simulation region suffers from being a bit on the small side in terms of being a realistic case. The region could not be made much larger before the optimization problem became too demanding with respect to the available hardware specifications on the laptop computer. Still, we argue that the results display a proof-of-concept simulation. It is also worth pointing out that the optimization horizon length, which also affects the problem size, has an impact on the generated trajectories. A too short horizon is quicker to solve, but gives more greedy trajectories than a long horizon. Finding an appropriate horizon length is one of several tuning challenges in this framework. Other tuning challenges include finding reasonable parameters for the sampling functions and relative weighting between the various terms of the objective function.

The proposed path planning framework is to a large extent dictated by the coarsely tessellated geometry; the generated trajectories tend to move between the coarse vertices. If the tessellation is too coarse in comparison to the field of view of each sensor, some regions may remain uncovered for all times. This is not necessarily a deal-breaker, but will indeed degrade the performance of the estimation. Nevertheless, care must be taken when defining the coarse tessellation. Trying to cover a too large region at the time with too fine tessellation will result in a huge optimization problem. Conversely, for a too small region, the problem is almost trivial in nature. If the estimated region $\Omega$ is too large for the optimization region $\Omega_\cap$, one should consider extensions of the currently proposed framework. We imagine the possibility of a time-varying observation region where between each re-planning the $\Omega_\cap$ may change by translating and rotating the coordinate system $\{\text{adr}\}$. Another possibility is to use independent teams of sensors each focusing on their own region of interest. These teams then form optimization problems that can be solved independently. This is a step toward a decentralized observation system and may be a beneficial approach to alleviate the scaling issue of the currently proposed approach.

The ice concentration estimation performance presented in this manuscript does not provide satisfying results. In our opinion the main reason for this inefficiency is the challenge of accurately discretizing advection-dominated transport equations. As mentioned earlier, the process of discretizing one such hyperbolic partial differential equation is particularly difficult with coarse spatial tessellation. Using a

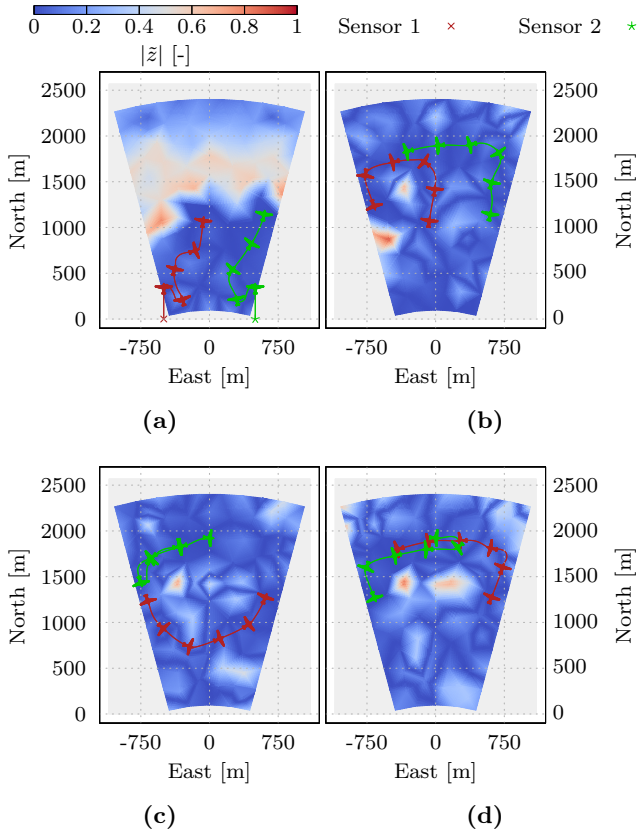


**Figure 4.17** Estimation error surface snapshots with sensor trajectories. The airplane markers indicate the switching of sampling intervals (every 35 s). The gray box is the admissible region:
(a) Trajectory interval $[0, 175]$ s with $|\tilde{z}|$ surface snapshot at 175 s;
(b) Trajectory interval $[175, 350]$ s with $|\tilde{z}|$ surface snapshot at 350 s;
(c) Trajectory interval $[350, 525]$ s with $|\tilde{z}|$ surface snapshot at 525 s; and,
(d) Trajectory interval $[525, 700]$ s with $|\tilde{z}|$ surface snapshot at 700 s.

naive approach with the Galerkin method will most definitely cause spurious oscillations. We used the Galerkin method for the ice drift in the Kalman filter and spurious oscillations readily occur (see e.g. the isolated peaks in Figure 4.17d). The SUPG method used for the drifting uncertainty does not sufficiently suppress the oscillations when an unstructured mesh is employed (John et al., 2008). We have increased the diffusion coefficient $\epsilon$ to avoid excessive oscillations at the cost of degraded ice concentration estimates over time. There is a vast body of literature dealing with methods for improving the numerical solution of the advection equation (see John et al. (2007) for a comprehensive comparison of methods). Many of these methods are complicated and do not easily fit into our optimization framework. Improving the ice concentration model and its estimation by choosing an appropriate method is considered future work.

## 4.12 Conclusion

This chapter presented a monitoring system that minimized a simplified description of a distributed parameter system's state uncertainty. The purpose of the monitoring system was to create feasible and collision-free paths for a set of mobile sensors. The objective was to efficiently perform state and parameter estimation of an advection-dominated transport equation. The problem was formulated as an optimal control problem that used planar kinematic vehicle descriptions and finite element discretization of a uniformly drifting sea ice concentration field.

The planned paths were employed in simulations on a sensor network that monitored a drifting sea ice field. The measurements were fused with a model description of the sea ice using a *batch-sequential* Kalman filter. The simulation results demonstrated a potential for the path planning network. We would like to see an extension of this framework where the scaling issue has been dealt with, as well as an improved estimation performance of the distributed parameter system.

# Chapter 5

# State Estimation of Ice Thickness Distribution Using Mobile Sensors

*This chapter considers the problem of guiding a mobile sensor network in a distributed parameter system. The ice thickness distribution of sea ice is an example of such a system. The objective is to improve the convergence of the state estimation error, compared to a nominal sensor network, by employing a gradient-based guidance scheme. The ice thickness is modeled as a continuity equation and the sensor dynamics as fully actuated 2-input-2-output mass-spring-damper systems. The approach builds on Lyapunov functions to construct the guidance law that achieves, under certain assumptions, a uniformly globally asymptotically stable system. A numerical example illustrates the approach. This work was published in Haugen et al. (2012).*

## 5.1 Introduction

KNOWLEDGE about the surrounding ice conditions, that is, detection, tracking, and forecasting of sea ice, ice ridges, and icebergs (Eik, 2008) is vital for the safety of marine operations in ice-infested regions. A system performing this task could be termed an *ice observer system* (Haugen et al., 2011), which consists of several sensor platforms that solves the task in a collaborated effort.

As stated in Haugen et al. (ibid.), unmanned vehicles are considered to become an important tool for the information gathering in an ice observer system. An unmanned vehicle can operate in harsh environments, the well-known *dirty, dull, dangerous*, in a safe and cost-effective manner. Motion spaces such as sub sea, on the surface, and in the air are all relevant in an ice observer system. We can choose the most suited subset of sensor platforms depending on the spatial scale that we want to estimate relevant ice features and ice properties.

Level ice is among the ice features of interest in an ice-monitoring setting. The physics of level ice dynamics is complex and consists of four elements (Leppäranta, 2011):

(i) Conservation of momentum; the forces acting are external forcing from air and water, internal stresses, Coriolis force, etc.

(ii) Conservation of ice; ice thickness redistribution, ice growth and decay.
(iii) Constitutive law; ice rheology, which relates stress to strength and deformation.
(iv) Ice states; parameters affecting ice strength and pressure, such as thickness and floe size distribution.

For illustration purposes, we will use a somewhat simple, but distributed ice model in this study. When employing a simple model in an ice observer structure, the complexity is manageable, whereas continuous updates from measurements are needed to keep the error drifts at bay. A major objective, which can be accomplished with estimation techniques, is to optimally combine models and measurements.

### 5.1.1 Previous Work

As far as the authors are aware, there exist no published results on a mobile sensor network for state estimation of level sea ice thickness. However, the more general problem of mobile sensors in distributed parameter systems is addressed in literature. Several different approaches have been investigated depending on the specific objectives and constraints posed on the problem.

Optimization-based approaches use some kind of uncertainty measure of the states in a region of interest to find efficient trajectories for the sensing devices. These sensors reduce the uncertainty of the state estimates (see Choi et al. (2010); Daescu et al. (2004); Majumdar et al. (2002); Palmer et al. (1998) and references therein).

A drawback of optimization-based methods is the computational cost. For this reason, several authors have investigated more computationally efficient algorithms that are based on nonlinear control theory (see Burns et al. (2009); Demetriou (2010); Demetriou et al. (2009, 2011) and references therein). In Demetriou et al. (2011) state estimation of a spatially distributed process on a one dimensional domain was illustrated using a Luenberger observer. A Lyapunov-based guidance law steered mobile sensor agents, which had mass-spring-damper models, to reduce the estimation error while simultaneously avoiding collisions. Lyapunov analysis showed stability of the error dynamics.

### 5.1.2 Contributions

This paper establishes necessary assumptions for a spatially discretized continuity equation, which describes level ice drift, to be applicable for the framework outlined in Demetriou et al. (ibid.). Furthermore, it demonstrates that fully actuated mass-spring-damper mobile sensors can be used to reduce the state estimation error. Uniform global asymptotic stability of the overall system is shown.

## 5.2 Problem Formulation

### 5.2.1 Continuum Model

Suppose we have an open, connected set of interest $\Omega \subset \mathbb{R}^2$. Let $\partial\Omega$ form the closure of $\Omega$, such that we have a closed set $\bar{\Omega} := \Omega \cup \partial\Omega$. The entity $p = [x, y]^\mathsf{T} \in \bar{\Omega}$ is

the position of a unit volume, and $u(t,p) : \mathbb{R}_{\geq 0} \times \bar{\Omega} \to \mathbb{R}^2$ is the flux field of the ice thickness $h(t,p) : \mathbb{R}_{\geq 0} \times \bar{\Omega} \to \mathbb{R}$, both dependent on the location $p$ and time $t$. The level ice may be described by the continuity equation

$$\frac{\partial h}{\partial t} + \nabla \cdot (uh) = S_h(t,p,h), \tag{5.1}$$

where $S_h : \mathbb{R}_{\geq 0} \times \bar{\Omega} \times \mathbb{R} \to \mathbb{R}$ is a source/sink term describing the generation/destruction rate of the ice thickness. Assume that the velocity flux field $u(t,p)$ is known, which is a significant simplification, as the extra complexity of the momentum equation and the constitutive law is avoided.

Since we wish to simulate ice drift and the domain $\bar{\Omega}$ is a subset of the whole ice floe, we propose to use mixed boundary conditions of Dirichlet and Neumann to allow a realistic representation of the ice drift. Concretely, the Neumann boundary conditions establish the possibility of ice to exit the domain, whereas the Dirichlet boundary conditions supply the domain with new ice. Define two distinct sets $\Sigma_1, \Sigma_2 \subseteq \partial\Omega$ such that $\Sigma_1 \cup \Sigma_2 = \partial\Omega$ holds. The set $\Sigma_1$ contains the Neumann boundary conditions and $\Sigma_2$ is the set with Dirichlet boundary conditions. We want to have Neumann conditions whenever the flux field at the boundary has a component in the same direction as the outward normal $n : \partial\Omega \to \mathbb{R}^2$ of the boundary. The inner product $u^\mathsf{T}(t,p)n(p)$ is used to determine the set where we have Neumann boundary conditions as

$$\Sigma_1 := \{p \in \partial\Omega : u^\mathsf{T}(t,p)n(p) > 0\}, \tag{5.2}$$

since $u(p,t)$ and $n(p)$ are column vectors. Then, $\forall p \in \Sigma_1$ we have the normal derivative

$$\frac{\partial h}{\partial n}(t,p) = \nabla h(t,p) \cdot n(p) = \kappa(p), \tag{5.3}$$

where $\kappa(p)$ is a function describing the outward derivative. In the following we set $\kappa(p) = 0$, which means that $h(t,p) : p \in \Omega$ is unaffected by $h(t,p) : p \in \Sigma_1$. To let $\Sigma_1$ and $\Sigma_2$ describe the whole set $\partial\Omega$, we define the set where we have Dirichlet boundary conditions as

$$\Sigma_2 := \{p \in \partial\Omega : u^\mathsf{T}(t,p)n(p) \leq 0\}. \tag{5.4}$$

For the Dirichlet condition, $h(t,p)$ is defined $\forall p \in \Sigma_2$ as

$$h(t,p) = \wp(p), \tag{5.5}$$

where $\wp(p)$ is a known function. An interesting property of this choice of mixed boundary conditions is that we have time-varying sets, since the flux field $u(t,p)$ is time dependent and may change the sign of the inner product defining the two sets $\Sigma_1$ and $\Sigma_2$.

Equation (5.1) can be written as an ordinary differential equation by using spatial discretization

$$\dot{\chi}(t) = f(t,\chi,\mathcal{U}) + g(t,\chi_{\partial\Omega},\mathcal{U}), \tag{5.6}$$

where $\chi(t)$ consists of spatially discretized values of $h(t,p)$, $\chi_{\partial\Omega}(t)$ is the boundary values of $h$, and $\mathcal{U}(t)$ is a matrix function of corresponding velocities.

We assume that the ice is (slowly) melting and use a simplified model for the melting rate (Leppäranta, 1993)

$$S_h(h) = -a_1 \frac{1}{h + a_2} - a_3, \tag{5.7}$$

where $a_1, a_2, a_3 > 0$. The melting rate is slow compared to the time horizon we plan to investigate. Hence, (5.7) can be linearized such that (5.6) becomes a linear time-varying system

$$\dot{\chi}(t) = A(t)\chi + B(t)\chi_{\partial\Omega}, \tag{5.8}$$

where $\mathcal{U}$ is incorporated through $t$.

For simplicity, we assume that $\bar{\Omega} = [0, L_x] \times [0, L_y]$ with spatial discretization step size $d_{xy}$ in both directions. With a carefully chosen domain size, we get $r, c \in \mathbb{N}$ interior grid points in $x$ and $y$ direction, respectively, in the Cartesian coordinate system. The thickness $h(t, p)$ at the location $p_{m,n} = [md_{xy},\, nd_{xy}]$ is denoted $\chi_{m,n}$. The state vector is thus $\chi \in \mathbb{R}^{rc}$ with the discrete thicknesses $\chi_{m,n}$ arranged in a suitable ordering, for instance *natural ordering* (Kincaid et al., 2009).

### 5.2.2 Measurement Model for the Mobile Sensors

Measurements of the state variables $\chi$ are obtained using mobile sensor devices. Let $q_i = [x_i,\, y_i]^\mathsf{T} \in \mathbb{R}^2$ be the time-varying position of a sensor. The measurement operator for this sensor is defined as $C_i : \mathbb{R}^2 \to \mathbb{R}^{4 \times rc}$. If we have $N$ mobile sensors and let $q(t) = [q_1(t)^\mathsf{T}, \cdots, q_N(t)^\mathsf{T}]^\mathsf{T}$, the measurement vector can be written as

$$y(q(t)) = C(q)\chi(t) = \begin{bmatrix} C_1(q_1(t)) \\ \vdots \\ C_N(q_N(t)) \end{bmatrix} \chi(t). \tag{5.9}$$

Since the model uses spatially discretized grid points in $\Omega \subset \mathbb{R}^2$, whereas the sensors move continuously in $\mathbb{R}^2$, we choose to use weighting functions that describe how the sensors measure the discretized process variables. The grid points may be coarsely distributed, so the vehicles may spend considerable time relatively far away from the grid points. We require the measurement operator $C(q)$ to output weighted pointwise measurements of the grid points in a neighborhood of the sensor positions. The operator therefore consists of bounded weighting surfaces $w_{m,n} \in \mathcal{C}^2(\mathbb{R}^2, \mathbb{R})$ for grid point $(m, n) \in \mathbb{I}_1^r \times \mathcal{I}_1^c$, where

$$\mathbb{I}_a^b := \{a, a+1, \cdots, b\}, \quad a, b \in \mathbb{Z}, \tag{5.10}$$

and $\mathcal{C}^2(\mathbb{R}^2, \mathbb{R})$ denotes the space of twice continuously differentiable functions with domain $\mathbb{R}^2$ and codomain $\mathbb{R}$.

Let $x_m = md_{xy}$, $y_n = nd_{xy}$, and $q_{m,n} = [x_m,\, y_n]^\mathsf{T}$. We require for a given position $q_i \in \Omega$ that $\forall (m, n) \in \mathbb{I}_1^r \times \mathbb{I}_1^c$

$$w_{m,n}(q_i) > 0 \iff \|q_i - q_{m,n}\|_\infty < d_{xy}. \tag{5.11}$$

A consequence of this property is that a measurement at the location $q_i$ will influence at most the four closest discretized ice thickness grid points. Suppose $q_i$ is

contained in the box formed by the grid points $(p_{v,w}, p_{v+1,w}, p_{v+1,w+1}, p_{v,w+1})$. Let $[a]_{i,j}$ be an all-zero matrix with appropriate dimensions, except at index $(i,j)$ where the element is $a$. The measurement matrix $C_i(q_i) \in \mathbb{R}^{4\times rc}$ can then be written as

$$\begin{aligned} C_i(q_i) = [w_{v,w}(q_i)]_{1,(w-1)r+v} + [w_{v+1,w}(q_i)]_{2,(w-1)r+v+1} \\ + [w_{v,w+1}(q_i)]_{3,wr+v} + [w_{v+1,w+1}(q_i)]_{4,wr+v+1}, \end{aligned} \tag{5.12}$$

where the weighting functions are indexed in correspondence with the ordering of the state vector, namely natural ordering.

Since the weighting surfaces are bounded and of class $\mathcal{C}^2$, we have the following properties for the measurement operator $C_i(q_i)$:

$$C_i(q_i) \in \mathcal{C}^2(\mathbb{R}^2, \mathbb{R}^{4\times rc}), \tag{5.13a}$$

$$\|C_i(q_i)\| \leq c_w. \tag{5.13b}$$

### 5.2.3 Problem Statement

The objective is to propose a state estimation scheme with a guidance law for the mobile sensors such that the ice thickness estimates converge faster than a *nominal sensor network*[1]. This problem is an application of the framework reported in Demetriou et al. (2011) with some simplifications and modifications.

## 5.3 State Estimation with a Mobile Sensor Network

The state estimation and mobile guidance objectives can be approached using a Lyapunov-based analysis of the closed-loop dynamics. We make the following assumption:

**Assumption 5.1.** *The system $\dot{\chi}(t) = A(t)\chi$ with a continuous and bounded $A(t)$ is globally exponentially stable.*

Let $Q(t)$ be a continuous, bounded, positive definite, symmetric matrix, that is, $\forall t \geq 0$

$$0 < c_1 I \leq Q(t) \leq c_2 I. \tag{5.14}$$

Then, as a consequence of Assumption 5.1, the following properties hold (Khalil, 2002, Theorem 4.12):

**Property 5.1.** *(i) There exists an $L > 0$ such that $\forall t \geq 0$*

$$\|A(t)\| \leq L. \tag{5.15}$$

*(ii) There exists a continuously differentiable, positive definite symmetric matrix $P(t)$ with*

$$0 < c_3 I \leq P(t) \leq c_4 I \tag{5.16}$$

*that satisfies the matrix differential equation*

$$\dot{P}(t) + P(t)A(t) + A^{\mathsf{T}}(t)P(t) = -Q(t). \tag{5.17}$$

[1] We denote a nominal sensor network as sensors following predefined trajectories.

### 5.3.1 Sensor Dynamics

Let $q_i \in \mathbb{R}^2$ be the position of sensor $i$. The sensor dynamics of a single sensor can be written as the 2-input-2-output system

$$\dot{q}_i(t) = r_i, \tag{5.18a}$$
$$\dot{r}_i(t) = M_i^{-1}(-D_i(r_i)r_i - K_i(q_i)q_i + u_i), \tag{5.18b}$$

where $i \in \mathbb{I}_1^N$, $r_i \in \mathbb{R}^2$, and $u_i \in \mathbb{R}^2$. $M_i$ is a bounded, positive definite symmetric matrix. Moreover, $D_i(r_i)$ and $K_i(q_i)$ are all bounded, positive semidefinite symmetric matrices. The sensors are decoupled from each other, so we write the sensor system compactly as

$$\dot{q}(t) = r, \tag{5.19a}$$
$$\dot{r}(t) = M^{-1}(-D(r)r - K(q)q + u), \tag{5.19b}$$

where the state vectors are $q = \mathrm{col}[q_1, \cdots, q_N]$, $r = \mathrm{col}[r_1, \cdots, r_N]$, and the system matrices are block diagonal: $M = \mathrm{bdiag}_{i\in\mathbb{I}_1^N}(M_i)$, $D(r) = \mathrm{bdiag}_{i\in\mathbb{I}_1^N}(D_i(r_i))$, and $\mathrm{bdiag}_{i\in\mathbb{I}_1^N}(K_i(q_i))$.

We want the mobile sensors to follow the reference trajectories defined $\forall i \in \mathbb{I}_1^N$ by $q_{r,i}(t)$, written compactly as $q_r(t) = \mathrm{col}[q_{r,1}(t), \cdots, q_{r,N}(t)]$. In addition, we assume that these trajectories are sufficiently smooth, such that $\max\{\|q_r\|, \|\dot{q}_r = r_r\|, \|\ddot{q}_r = \dot{r}_r\|\} \leq \beta_d$. We define the error coordinates

$$\tilde{q}(t) = q(t) - q_r(t), \tag{5.20a}$$
$$\tilde{r}(t) = r(t) - r_r(t). \tag{5.20b}$$

**Lemma 5.1.** *The control law*

$$u = M\dot{r}_r + D(r)r_r + K(q)q - K_p\tilde{q} - K_d\tilde{r} + \tilde{u}(e, \tilde{q}), \tag{5.21}$$

*where $K_p, K_d \in \mathbb{R}^{2N\times 2N}$ are user-defined, bounded, and positive definite symmetric matrices, gives the closed-loop dynamics*

$$\dot{\tilde{q}}(t) = \tilde{r}, \tag{5.22a}$$
$$\dot{\tilde{r}}(t) = M^{-1}(-D(r)\tilde{r} - K_p\tilde{q} - K_d\tilde{r} + \tilde{u}(e, \tilde{q})). \tag{5.22b}$$

*Moreover, the control law renders the system* (5.22) *uniformly globally stable when* $\tilde{u}(e, \tilde{q}) = 0$.

*Proof.* Choose the energy-based Lyapunov function

$$V_q(t, \tilde{q}, \tilde{r}) = \frac{1}{2}(\tilde{r}^\mathsf{T} M\tilde{r} + \tilde{q}^\mathsf{T} K_p\tilde{q}), \tag{5.23}$$

which is positive definite, decrescent, and radially unbounded. The derivative of $V_q$ along the trajectories of the sensor system is given by

$$\dot{V}_q = \langle\tilde{r}, M\dot{\tilde{r}}\rangle + \langle\tilde{q}, K_p\tilde{r}\rangle \tag{5.24}$$
$$= -\langle\tilde{r}, D(r)\tilde{r} + K_p\tilde{q} + K_d\tilde{r} - \tilde{u}\rangle + \langle\tilde{q}, K_p\tilde{r}\rangle \tag{5.25}$$
$$= -\tilde{r}^\mathsf{T}(D(r) + K_d)\tilde{r} + \tilde{r}^\mathsf{T}\tilde{u}(e, \tilde{q}). \tag{5.26}$$

If we let the perturbing signal be $\tilde{u}(e, \tilde{q}) \equiv 0$, the last term disappears and we get

$$\dot{V}_q(t, \tilde{q}, \tilde{r}) = -\tilde{r}^\mathsf{T}(D(r) + K_d)\tilde{r} \leq 0, \tag{5.27}$$

and the conclusion follows. □

**Remark 5.1.** Stronger results can be obtained by invoking Barbălat's Lemma (Loría et al., 2005), but this is not relevant at this point.

To accommodate the error coordinates in the measurement operator $C(q)$, we define a similar operator such that

$$\bar{C}(\tilde{q}) = C(q). \tag{5.28}$$

For simplicity we write $\bar{C}(\tilde{q})$ as $C(\tilde{q})$ in the following analysis.

The boundedness and positive definiteness of the sensor matrices provide us with the following properties that will be relevant later in this chapter.

**Property 5.2.** *The upper and lower bounds of the system matrices are*

*(i)* $0 < c_5 I \leq M \leq c_6 I$,

*(ii)* $0 \leq c_7 I \leq D(r) \leq c_8 I$,

*(iii)* $0 \leq c_9 I \leq K(q) \leq c_{10} I$,

*(iv)* $0 < c_{11} I \leq K_p \leq c_{12} I$,

*(v)* $0 < c_{13} I \leq K_d \leq c_{14} I$.

### 5.3.2 State Estimator

Let the state estimator be a Luenberger observer:

$$\dot{\hat{\chi}}(t) = (A(t) - L(\tilde{q})C(\tilde{q}))\hat{\chi}(t) + B(t)\hat{\chi}_{\partial\Omega}(t) + L(\tilde{q})y(\tilde{q}), \tag{5.29a}$$

$$\hat{\chi}(0) = \hat{\chi}_0 \neq \chi(0), \tag{5.29b}$$

with filter gain similar to the one proposed in Demetriou et al. (2011):

$$L(\tilde{q}) = C^\mathsf{T}(\tilde{q})\Gamma, \tag{5.30}$$

where $\Gamma$ is a user-defined, bounded $4N \times 4N$ positive definite symmetric matrix. This matrix can be used as a weighting of how fast the model states should converge to the measurements.

**Assumption 5.2.** *The boundary function is perfectly known, that is,* $\forall t \in \mathbb{R}_{\geq 0}$ *we have*

$$\hat{\chi}_{\partial\Omega}(t) = \chi_{\partial\Omega}(t). \tag{5.31}$$

Define $e(t) = \chi(t) - \hat{\chi}(t)$ as the estimation error of the state estimator. The error dynamics becomes

$$\dot{e}(t) = A_{cl}(t, \tilde{q})e, \quad e(0) \neq 0, \tag{5.32}$$

where $A_{cl}(t, \tilde{q}) = A(t) - C^\mathsf{T}(\tilde{q})\Gamma C(\tilde{q})$.

**Remark 5.2.** We consider neither the error dynamics, nor the measurements to be contaminated by noise. This is a significant simplification and in reality they are both noisy due to modeling inaccuracies. In the case of white, zero mean, and uncorrelated Gaussian process and measurement noise that are additive, the Luenberger observer yields unbiased estimates (Demetriou et al., 2009; Simon, 2006).

**Property 5.3.** *We have* $\|\Gamma\| < c_\Gamma$ *and from* (5.13b) *that* $\|C_i(\tilde{q}_i)\| \leq c_w$*, so we know that for some* $c_{15} > 0$

$$0 \leq C^\mathsf{T}(\tilde{q})\Gamma C(\tilde{q}) \leq c_{15} I. \tag{5.33}$$

The output estimation error is defined as

$$\epsilon(t) = \begin{bmatrix} \epsilon_1(t) \\ \vdots \\ \epsilon_N(t) \end{bmatrix} = \begin{bmatrix} C_1(\tilde{q}_1)e(t) \\ \vdots \\ C_N(\tilde{q}_N)e(t) \end{bmatrix}. \tag{5.34}$$

### 5.3.3 Lyapunov-based Guidance Law

When constructing a guidance law for the state estimation problem, we consider a Lyapunov function that consists of two terms

$$V(t, e, \tilde{q}, \tilde{r}) = V_e(t, e, \tilde{q}) + k_\gamma k_q V_q(t, \tilde{q}, \tilde{r}), \tag{5.35}$$

where $k_\gamma, k_q > 0$. Consider

$$V_e(t, e, \tilde{q}) = \frac{1}{2} e^\mathsf{T} P(t) e - \frac{k_\gamma}{2} \underbrace{e^\mathsf{T} C(\tilde{q})^\mathsf{T}}_{\epsilon^\mathsf{T}(t)} \Gamma \underbrace{C(\tilde{q}) e}_{\epsilon(t)} \tag{5.36}$$

as the composite Lyapunov function for the error dynamics. The motivation for using this Lyapunov function is that the estimation error will be introduced in the guidance law for the mobile sensors. Without loss of generality we assume that the sensor dynamics is homogeneous, that is, each vehicle has the same dynamics. This allows us to extract the scaling $k_q$ from the Lyapunov function and simplifies the analysis. As we will see, this tunable gain accommodates an appropriate response in the guidance law.

**Lemma 5.2.** $V_e(t, e, \tilde{q})$ *is positive definite, decrescent and radially unbounded in* $e$*.*

*Proof.* Use (5.16) and (5.33) and choose $k_\gamma = \frac{c_3 - \gamma}{c_{15}}$, where $c_3$ and $c_{15}$ are defined in the mentioned equations, and $0 < \gamma < c_{15}$. The Lyapunov function satisfies

$$V_e(t, e, \tilde{q}) = \frac{1}{2} e^\mathsf{T} P(t) e - \frac{k_\gamma}{2} e^\mathsf{T} C(\tilde{q})^\mathsf{T} \Gamma C(\tilde{q}) e \tag{5.37}$$

$$\geq \frac{1}{2} c_3 \|e\|_2^2 - \frac{k_\gamma}{2} c_{15} \|e\|_2^2 \tag{5.38}$$

$$= \frac{\gamma}{2} \|e\|_2^2 > 0, \tag{5.39}$$

which confirms that $V_e(t, e, \tilde{q})$ is positive definite in $e$ and radially unbounded in $e$. To show that it also is decrescent, use (5.16) and (5.33) once more to verify

$$V_e(t, e, \tilde{q}) \leq \frac{1}{2} c_4 \|e\|_2^2 - 0, \tag{5.40}$$

which concludes the proof. □

**Remark 5.3.** Even though $\tilde{q}$ is part of the Lyapunov function, we do not require $V(t, e, \tilde{q})$ to be positive definite for this variable at this point. Hence, we use the terminology 'positive definite in $e$'.

**Lemma 5.3.** *The time derivative of $V_e(t, e, \tilde{q})$ along the trajectories of the estimation error* (5.32) *is*

$$\dot{V}_e(t, e, \tilde{q}) = -\frac{1}{2} e^\mathsf{T} Q(t) e - e^\mathsf{T} P(t) C^\mathsf{T}(\tilde{q}) \Gamma C(\tilde{q}) e - k_\gamma \epsilon^\mathsf{T} \Gamma \frac{\partial \epsilon}{\partial \tilde{q}} \tilde{r}. \tag{5.41}$$

*Proof.* See Appendix. □

**Lemma 5.4.** *The perturbing guidance law*

$$\tilde{u}(e, \tilde{q}) = \frac{1}{k_q} \frac{\partial \epsilon^\mathsf{T}(t)}{\partial \tilde{q}} \Gamma \epsilon(t), \tag{5.42}$$

*which is Lipschitz continuous, renders the time derivative of the Lyapunov candidate function $V(t, e, \tilde{q}, \tilde{r})$ negative semidefinite.*

*Proof.* Lipschitz continuity follows from (5.13a). The time derivative of the Lyapunov function $V(t, e, \tilde{q}, \tilde{r})$ is

$$\dot{V}(t, e, \tilde{q}, \tilde{r}) = \dot{V}_e(t, e, \tilde{q}) + k_\gamma k_q \dot{V}_q(t, \tilde{q}, \tilde{r}). \tag{5.43}$$

Lemmas 5.1 and 5.3 are used to get

$$\begin{aligned}
\dot{V} &= \dot{V}_e + k_\gamma k_q \dot{V}_q && (5.44)\\
&= -\frac{1}{2} e^\mathsf{T} Q(t) e - e^\mathsf{T} P(t) C^\mathsf{T} \Gamma C e - k_\gamma \epsilon^\mathsf{T} \Gamma \frac{\partial \epsilon}{\partial \tilde{q}} \tilde{r} \\
&\quad - k_\gamma k_q \left( \tilde{r}^\mathsf{T} (D(r) + K_d) \tilde{r} - \tilde{u}^\mathsf{T} \tilde{r} \right) && (5.45)\\
&= -\frac{1}{2} e^\mathsf{T} Q(t) e - e^\mathsf{T} P(t) C(\tilde{q})^\mathsf{T} \Gamma C(\tilde{q}) e \\
&\quad - k_\gamma k_q \tilde{r}^\mathsf{T} (D(r) + K_d) \tilde{r} + k_\gamma \left( -\epsilon^\mathsf{T} \Gamma \frac{\partial \epsilon}{\partial \tilde{q}} + k_q \tilde{u}^\mathsf{T} \right) \tilde{r}. && (5.46)
\end{aligned}$$

Inserting the perturbing guidance law (5.42) into the above equation cancels the last term and we get

$$\dot{V} = -\frac{1}{2} e^\mathsf{T} Q(t) e - e^\mathsf{T} P(t) C(\tilde{q})^\mathsf{T} \Gamma C(\tilde{q}) e - k_\gamma k_q \tilde{r}^\mathsf{T} (D(r) + K_d) \tilde{r} \leq 0, \tag{5.47}$$

and the conclusion follows. □

The perturbing guidance law makes the mobile sensors move away from the reference trajectories in the steepest ascent direction of the output estimation error.

**Theorem 5.1.** *The closed-loop dynamics of the system* (5.22) *and* (5.32) *with the perturbing guidance law of Lemma 5.4 is uniformly globally asymptotically stable.*

*Proof.* In the following, we refer to the necessary conditions of Matrosov's theorem, which is stated in Paden et al. (1988, Theorem 1). Relevant bounds $c_i$ can be found in (5.14), Properties 5.1, 5.2, and 5.3. Condition 1 is satisfied since $V(t, e, \tilde{q}, \tilde{r})$ is a radially unbounded, positive definite and decrescent Lyapunov function.

Define $V^*(e, \tilde{q}, \tilde{r}) : \mathbb{R}^{rc} \times \mathbb{R}^{2N} \times \mathbb{R}^{2N} \to \mathbb{R}$ as

$$V^*(e, \tilde{q}, \tilde{r}) = -\frac{c_1}{2}\|e\|_2^2 - k_\gamma k_q(c_7 + c_{13})\|\tilde{r}\|_2^2 \leq 0. \tag{5.48}$$

Since

$$\dot{V}(t, e, \tilde{q}, \tilde{r}) \leq V^*(e, \tilde{q}, \tilde{r}), \tag{5.49}$$

we conclude that Condition 2 is satisfied. Conditions 1 and 2 actually state that the origin of the system is uniformly globally stable (UGS).

We propose the auxiliary function

$$W(t, e, \tilde{q}, \tilde{r}) = \tilde{q}^\mathsf{T} M \tilde{r}. \tag{5.50}$$

Since the system is UGS, $\tilde{q}$ and $\tilde{r}$ are bounded. Furthermore, by Property 5.2 we have that $\|M\| \leq c_6$, so $\|W(t, e, \tilde{q}, \tilde{r})\|$ is bounded and Condition 3 is fulfilled.

The time derivative of $W(t, e, \tilde{q}, \tilde{r})$ is

$$\dot{W} = \tilde{r}^\mathsf{T} M \tilde{r} + \tilde{q}^\mathsf{T}(-D(r)\tilde{r} - K_p\tilde{q} - K_d\tilde{r} + \tilde{u}(e, \tilde{q})) \tag{5.51}$$

$$= \tilde{r}^\mathsf{T} M \tilde{r} - \tilde{q}^\mathsf{T} K_p \tilde{q} - \tilde{r}^\mathsf{T}(D(r) + K_d)\tilde{q} + \tilde{q}^\mathsf{T}\tilde{u}(e, \tilde{q}). \tag{5.52}$$

Once again, since the system is UGS and the system matrices are continuously bounded, and by recalling that $\tilde{u}(e, \tilde{q})$ is Lipschitz continuous, we conclude that $\dot{W}(t, e, \tilde{q}, \tilde{r})$ is continuous in all arguments and does not depend on $t$ explicitly. Hence, Condition 4'(a) is satisfied.

Define the set where $V^*(e, \tilde{q}, \tilde{r}) = 0$ as

$$S = \{(e, \tilde{q}, \tilde{r}) \in \mathbb{R}^{rc} \times \mathbb{R}^{2N} \times \mathbb{R}^{2N} : V^*(e, \tilde{q}, \tilde{r}) = 0\}. \tag{5.53}$$

We observe that in this set $e \equiv 0$, $\tilde{r} \equiv 0$, and $\tilde{q} \in \mathbb{R}^{2N}$. There exists a class $\mathcal{K}$ function $k(\|\operatorname{col}(e, \tilde{q}, \tilde{r})\|)$ such that $\forall (t, \operatorname{col}(e, \tilde{q}, \tilde{r})) \in \mathbb{R}_{\geq 0} \times S$ we have

$$|\dot{W}(t, e, \tilde{q}, \tilde{r})| \geq k(\|\operatorname{col}(e, \tilde{q}, \tilde{r})\|). \tag{5.54}$$

More specifically, we choose

$$k(\|\operatorname{col}(e, \tilde{q}, \tilde{r})\|) = c_{11}\|\tilde{q}\|_2^2 + \|e\|_2^2 + \|\tilde{r}\|_2^2, \tag{5.55}$$

and can conclude that Condition 4'(b) holds.

Finally, by Property 5.1i) and the boundedness of the states and system matrices, Condition 5 holds. All conditions of Matrosov's theorem are satisfied and since these conditions hold globally, we conclude that the origin is uniformly globally asymptotically stable. □

## 5.4 Calculation of the Gradient

The gradient $\frac{\partial \epsilon(t)}{\partial \tilde{q}}$ is the Jacobian of the output estimation error and can be written as

$$\frac{\partial \epsilon(t)}{\partial \tilde{q}} = \begin{bmatrix} \frac{\partial \epsilon_1}{\partial \tilde{x}_1} & \frac{\partial \epsilon_1}{\partial \tilde{y}_1} & \cdots & \frac{\partial \epsilon_1}{\partial \tilde{x}_N} & \frac{\partial \epsilon_1}{\partial \tilde{y}_N} \\ \frac{\partial \epsilon_2}{\partial \tilde{x}_2} & \frac{\partial \epsilon_2}{\partial \tilde{y}_2} & \cdots & \frac{\partial \epsilon_2}{\partial \tilde{x}_N} & \frac{\partial \epsilon_2}{\partial \tilde{y}_N} \\ \vdots & & \cdots & \vdots & \vdots \\ \frac{\partial \epsilon_N}{\partial \tilde{x}_N} & \frac{\partial \epsilon_N}{\partial \tilde{y}_N} & \cdots & \frac{\partial \epsilon_N}{\partial \tilde{x}_N} & \frac{\partial \epsilon_N}{\partial \tilde{y}_N} \end{bmatrix}. \tag{5.56}$$

Unfortunately, this Jacobian is not immediately available because it depends on the actual system that is being estimated. The authors of Demetriou et al. (2011) state that "*each sensing device only uses its own sensor to estimate its own output estimation error*". We adopt this assumption and consequently, we have that for each sensor $i \in \mathbb{I}_1^N$

$$\frac{\partial \epsilon_i}{\partial \tilde{q}_i} = \begin{bmatrix} \frac{\partial \epsilon_i}{\partial \tilde{x}_i} & \frac{\partial \epsilon_i}{\partial \tilde{y}_i} \end{bmatrix} \in \mathbb{R}^{4\times 2}. \tag{5.57}$$

Hence, the Jacobian is an upper block diagonal matrix

$$\frac{\partial \epsilon(t)}{\partial \tilde{q}} = \text{bdiag}\left[ \frac{\partial \epsilon_1}{\partial \tilde{q}_1}, \quad \frac{\partial \epsilon_2}{\partial \tilde{q}_2}, \quad \cdots, \quad \frac{\partial \epsilon_N}{\partial \tilde{q}_N} \right]. \tag{5.58}$$

Ideally, the gradient matrix $\frac{\partial \epsilon_i}{\partial \tilde{q}_i}$ consists of a gradient vector for each of the four closest output estimation error grid points for that particular vehicle. Approximations of these output estimation error gradient vectors can be calculated using a four-pronged probe (Demetriou, 2007; Demetriou et al., 2011). This basically means that each sensing vehicle provides four distinct measurements at any time, that is, $\forall j \in \mathbb{I}_1^4$ we have $p_j \in \mathbb{R}^2$ and the measurements $C(p_j)\chi(t)$. Let $\mathbf{1}_a \in \mathbb{R}^a$ be a $a$-dimensional column vector of ones. We choose to estimate (5.57) with the steepest ascent direction of the spatial estimation error surface at the sensor positions, that is, $\forall i \in \mathbb{I}_1^N$ we have

$$\frac{\partial \epsilon_i(t)}{\partial \tilde{q}_i} = \mathbf{1}_4 \otimes \left. \frac{\partial \tilde{h}(t,p)}{\partial p} \right|_{p=q_i}, \tag{5.59}$$

where $p = [x,\, y]^\mathsf{T} \in \mathbb{R}^2$ is the spatial coordinate vector, $\tilde{h}(t,p) = h(t,p) - \hat{h}(t,p)$ is the spatially continuous error surface, and $\otimes$ is the Kronecker product.

The linear combination of the four measurement values provided by each probe constitutes a value for that particular probe location. A spatial gradient vector is approximated using the finite central difference in the $x$ and $y$ direction for these probe values. We can write

$$\frac{\partial \epsilon_i}{\partial \tilde{q}_i} \approx \mathbf{1}_4 \otimes \frac{1}{4} \begin{bmatrix} \mathbf{1}_4 \cdot \frac{(C(q_i+\Delta x)-C(q_i-\Delta x))e(t)}{2\|\Delta x\|} \\ \mathbf{1}_4 \cdot \frac{(C(q_i+\Delta y)-C(q_i-\Delta y))e(t)}{2\|\Delta y\|} \end{bmatrix}^\mathsf{T}, \tag{5.60}$$

where $\Delta x = [\delta x,\, 0]^\mathsf{T}$ and $\Delta y = [0,\, \delta y]^\mathsf{T}$ with constants $\delta x, \delta y > 0$.

**Remark 5.4.** Recall that the state estimator uses a measurement located at $q_i$ for vehicle $i$. Since $q_i$ is the centroid of the four probe locations, it can be approximated by these probe measurements. Alternatively, each vehicle provides yet another measurement at this location.

## 5.5 Numerical Example

### 5.5.1 Setup

We consider the region $\bar{\Omega} = [0,\, 600] \times [0, 300]\ \mathrm{m}^2$ with a spatial discretization step size $d_{xy} = 50\,\mathrm{m}$, such that $r = 11$ and $c = 5$. Define a constant, uniform velocity flux field $u(t,p) = [0,\, 1]^\mathsf{T}\ \mathrm{m\,s^{-1}}$. Following (5.2), we have Neumann boundary conditions $\forall p \in \mathbb{R}^2 : p = [x,\, 300]^\mathsf{T}$ m, and otherwise Dirichlet boundary conditions, that is, $\forall p \in \Sigma_2$ we let $\wp(p) = 1\,\mathrm{m}$. By introducing a different Dirichlet boundary function $\hat{\wp}(p) = 0.8\,\mathrm{m}$ in the observer, the process will be introduced to a continuous inflow of estimation error $\tilde{\chi}_{\partial\Omega} = 0.2\,\mathrm{m}$, and the error dynamics becomes

$$\dot{e}(t) = A_{cl}(q)e(t) + B(t)(\underbrace{\chi_{\partial\Omega}(t) - \hat{\chi}_{\partial\Omega}(t)}_{\tilde{\chi}_{\partial\Omega}(t)}). \tag{5.61}$$

Suppose the initial discretized ice thickness state vector is

$$\chi(0) = \mathbf{1}_{rc} + v, \tag{5.62}$$

where $v \sim \mathcal{N}(0, \frac{1}{100}\,\mathrm{diag}(\mathbf{1}_{rc}))$ is a vector of independent zero mean Gaussian random variables. Further, let $\hat{\chi}(0) = 0.8 \cdot \mathbf{1}_{rc}$ m. We choose a uniform and linear sink term $S_h(h) = -10^{-7}h\ \mathrm{m\,s^{-1}}$.

#### Measurement Model

We implement the weighting surfaces $w_{m,n} \in \mathcal{C}^2(\mathbb{R}^2, \mathbb{R})$ for all $(m,n) \in \mathbb{I}_1^r \times \mathbb{I}_1^c$ as bilinear interpolations. Define the values

$$w_{m,n}(q_{m,n}) = 1, \tag{5.63a}$$
$$w_{m,n}(q_{m\pm1,n\pm1}) = 0, \tag{5.63b}$$

such that $w_{m,n}(p)$ becomes

$$w_{m,n}(p) = \begin{cases} \frac{(x-x_{m-1})(y-y_{n-1})}{(x_m-x_{m-1})(y_n-y_{n-1})}, (x,y) \in [x_{m-1}, x_m] \times [y_{n-1}, y_n] \\ \frac{(x-x_m)(y_n-y)}{(x_{m+1}-x_m)(y_n-y_{n-1})}, (x,y) \in [x_m, x_{m+1}] \times [y_{n-1}, y_n] \\ \frac{(x_m-x)(y-y_n)}{(x_m-x_{m-1})(y_{n+1}-y_n)}, (x,y) \in [x_{m-1}, x_m] \times [y_n, y_{n+1}] \\ \frac{(x_{m+1}-x)(y_{n+1}-y)}{(x_{m+1}-x_m)(y_{n+1}-y_n)}, (x,y) \in [x_m, x_{m+1}] \times [y_n, y_{n+1}] \\ 0 \quad , \quad \text{otherwise.} \end{cases} \tag{5.63c}$$

This weighting surface is basically a square pyramid with apex at the grid point $(m,n)$. To illustrate, consider a cross section through a sensor's position $q_i = [q_x,\, w \cdot d_{xy}]^\mathsf{T}$ along the x-axis. Fig. 5.1 depicts the weighting of the neighboring

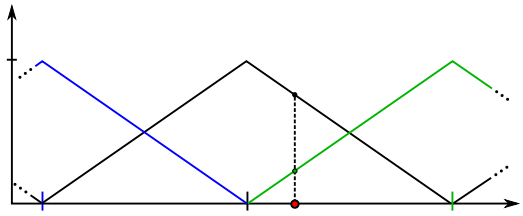

**Figure 5.1** The neighboring grid points of the vehicle are measured with the specified weights.

grid points. The chosen weighting surface does not satisfy the twice continuously differentiable requirement. Therefore, the perturbing guidance law is not Lipschitz continuous. This is more a technical problem than it is practical, as it is most likely possible to construct a sufficiently smooth weighting surface that is almost identical to the one chosen here.

### Mobile Sensor Dynamics

We choose a homogeneous sensor network consisting of $N = 2$ sensors. The sensors are modeled as two independent mass-spring-damper systems in $x$ and $y$ direction, respectively. The closed-loop dynamics of sensor $i$ is thus

$$\dot{\tilde{q}}_i = \tilde{r}_i, \tag{5.64a}$$

$$\dot{\tilde{r}}_i = -\begin{bmatrix} \frac{k}{m} & 0 \\ 0 & \frac{k}{m} \end{bmatrix} \tilde{q}_i - \begin{bmatrix} \frac{d}{m} & 0 \\ 0 & \frac{d}{m} \end{bmatrix} \tilde{r}_i + M^{-1}\tilde{u}_i(e, \tilde{q}). \tag{5.64b}$$

The input $\tilde{u}_i$ is part of the perturbing guidance law of Theorem 5.1. If we let $\tilde{u}_i = 0$, we get the nominal sensor network, that is, the guidance law depends only on a predefined trajectory. We choose elliptic reference trajectories

$$q_{r,i}(t) = \begin{bmatrix} p_{x,i} + R_x \cos(\omega t) \\ p_{y,i} - R_y \sin(\omega t) \end{bmatrix}, \tag{5.65}$$

where relevant parameters are given in Table 5.1. The estimator gain matrix $\Gamma$ is chosen as

$$\Gamma = \operatorname{diag}(\mathbf{1}_{4N}). \tag{5.66}$$

## 5.5.2 Results

The system was simulated for 300 s in Matlab® using the *ode15s* solver. The simulation was performed using both gradient-based and nominal guidance laws. Fig. 5.2 displays snapshots of the state estimation error in the simulated region at the times $t = \{0, 100, 300\}$ s for the case of gradient-based guidance law. In addition, the figures show the traveled paths of the moving sensors. In Fig. 5.3 it can be observed that the state estimation error norm $\|\chi(t) - \tilde{\chi}(t)\|_2$ becomes smaller in the case of gradient-based guidance compared to the case of nominal trajectories.

**Table 5.1** Parameters for mobile sensors.

| Parameter | Value | Unit |
|---|---|---|
| $m$ | 30 | kg |
| $p_{x,1}$, $p_{y,1}$ | 150, 150 | m |
| $p_{x,2}$, $p_{y,2}$ | 450, 150 | m |
| $R_x$ | 100 | m |
| $R_y$ | 50 | m |

| Parameter | Value | Unit |
|---|---|---|
| $\omega$ | $\frac{\pi}{50}$ | $\mathrm{rad\,s^{-1}}$ |
| $k$ | $\frac{2\pi^2}{15}$ | $\mathrm{kg\,m^{-2}}$ |
| $d$ | $2\pi$ | $\mathrm{kg\,s^{-1}}$ |
| $\delta x$ | $\frac{100}{3}$ | m |
| $\delta y$ | $\frac{100}{3}$ | m |
| $k_q$ | $7 \cdot 10^{-7}$ | - |

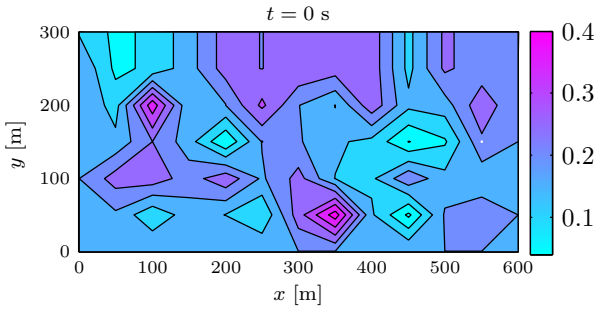


**(a)** $|\chi(0) - \hat{\chi}(0)|$.

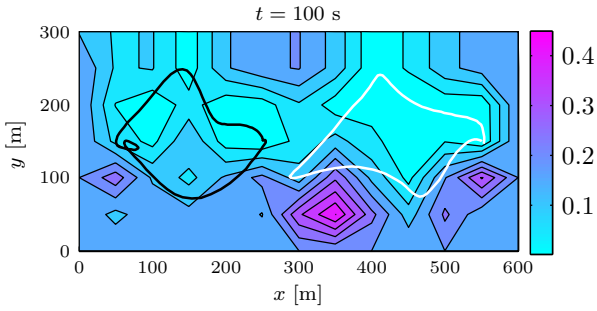


**(b)** $|\chi(100) - \hat{\chi}(100)|$.

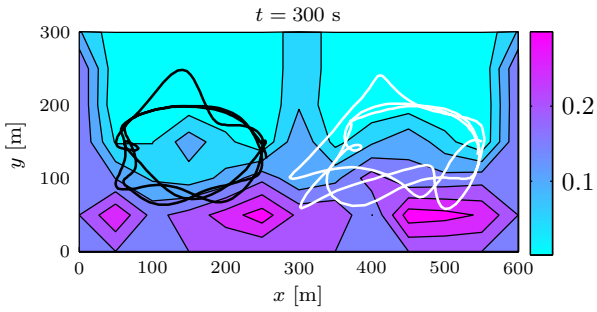


**(c)** $|\chi(300) - \hat{\chi}(300)|$.

**Figure 5.2** Snapshots of the state estimation error surface including executed trajectories.

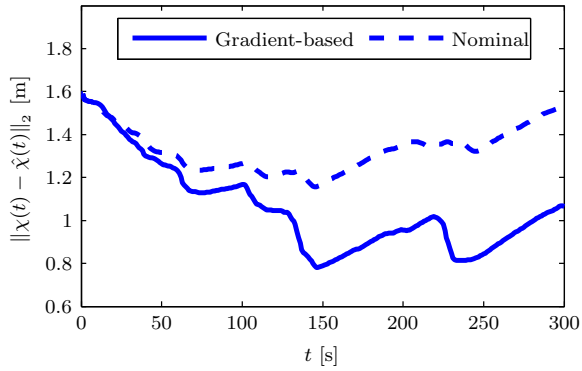


**Figure 5.3** The norm of all the discrete state estimation error values as a function of time. The reason why the error norm fails to converge to zero is due to the error in the boundary conditions, which is not assumed in the analysis.

## 5.6 Discussion

The guidance law of Theorem 5.1 consists of a term guiding the vehicles in the direction of increasing estimation error. Since the grid points of the discretized process have a coarse resolution, the length scales of the probe measurements need to be sufficiently large in order to get an appropriate response. This introduces the additional complication of determining appropriate length scales to obtain good approximations of the error gradients. Recent work on this problem is reported in Court et al. (2012).

The analysis proves uniformly globally asymptotically stable error dynamics. To make an illustrative relevant example, an error is introduced through an underestimated boundary vector $\hat{\chi}_{\partial\Omega}$. Thus, $\tilde{\chi}_{\partial\Omega} \neq 0$, which was assumed zero in the analysis. Furthermore, the melting process also contributes to the convergence. This process is very slow compared to the speed of the flux field in relation to the simulated region. Consequently, convergence to zero of the state estimation error is not achieved within the region of interest.

Even though the gradient-based estimation scheme displays better performance compared to the case of nominal trajectories, more sophisticated paths can most likely be constructed such that it results in a smaller state estimation error. This is especially true if knowledge about the flux field is utilized in the path planning.

A weakness in the proposed approach is that certain states may remain unvisited. The guidance law only guides the mobile sensors using the local error gradients. In general, the error surface is non-convex, so error regions might not be visited. Also, the spring forces of the mass-spring-damper system may dominate the gradient-based force when the mobile sensors are far from their reference trajectories.

A collision-free operation is not guaranteed. One advantage of the Lyapunov-based guidance law is that it can be extended with additional objectives. More concretely, as reported in Demetriou et al. (2011), by introducing yet other energy-like signals in the Lyapunov function, the sensors can repel each other and thereby avoid collision. However, adding too many simultaneous objectives may result in

responses that counteract the individual objectives.

In real-world applications wireless mobile sensor networks do experience loss of communication, delay and corruption in measurements, et cetera. The proposed approach is computationally efficient and can probably be implemented in a partly decentralized manner. This may reduce the need for continuous communication between the individual sensing agents. Still, this challenge is of major concern with respect to the robustness and safety of the estimation scheme.

## 5.7 Conclusion

We have investigated a scheme for estimating the ice thickness distribution of an ice cover. The mobile sensor network was controlled using a gradient-like guidance law that steers the mobile sensors in the direction of increasing state estimation error. Numerical simulations demonstrated an improved performance compared to a nominal sensor network.

Simulations also show that the underestimated boundary conditions significantly impact the estimation performance. By extending this estimation scheme to also estimate the boundary parameters, an improved estimation performance is predicted. This topic is considered as an interesting extension to the presented result.

## 5.A Proof of Lemma 5.3

*Proof.* For simplicity, we omit the arguments of the states and operators. The time derivative of the Lyapunov function $V_e(t, e, \tilde{q})$ is

$$\dot{V}_e = \frac{1}{2}\left\{\langle \dot{e}, Pe\rangle + \langle e, \dot{P}e\rangle + \langle e, P\dot{e}\rangle - 2k_\gamma\langle \dot{\epsilon}, \Gamma\epsilon\rangle\right\}. \tag{5.67}$$

We use the matrix differential equation in Property 5.1ii and (5.32) to get

$$\dot{V}_e = \frac{1}{2}\left\{\langle A_{cl}e, Pe\rangle + \langle e, -(PA + A^\mathsf{T}P + Q)e\rangle + \langle e, PA_{cl}e\rangle - 2k_\gamma\langle \frac{\partial \epsilon}{\partial \tilde{q}}\dot{\tilde{q}}, \Gamma\epsilon\rangle\right\}. \tag{5.68}$$

Recall that $A_{cl}(t, \tilde{q}) = A(t) - C(\tilde{q})^\mathsf{T}\Gamma C(\tilde{q})$. By appreciating that $P(t)$ is symmetric, we can write

$$\langle C^\mathsf{T}\Gamma Ce, Pe\rangle = \langle e, PC^\mathsf{T}\Gamma Ce\rangle. \tag{5.69}$$

Moreover, we observe that some terms cancel, so the time derivative of $V_e$ simplifies to

$$\dot{V}_e = -\frac{1}{2}\langle e, Qe\rangle - \langle e, PC^\mathsf{T}\Gamma Ce\rangle - k_\gamma\langle \frac{\partial \epsilon}{\partial \tilde{q}}\dot{\tilde{q}}, \Gamma\epsilon\rangle, \tag{5.70}$$

or equivalently (using $\dot{\tilde{q}} = \tilde{r}$)

$$\dot{V}_e(t, e, \tilde{q}) = -\frac{1}{2}e^\mathsf{T}(t)Q(t)e - e^\mathsf{T}P(t)C^\mathsf{T}(\tilde{q})\Gamma C(\tilde{q})e - k_\gamma\epsilon^\mathsf{T}\Gamma\frac{\partial \epsilon}{\partial \tilde{q}}\tilde{r}. \tag{5.71}$$

□

# Conclusion

In this thesis, we have acknowledged the possible benefit of aerial ice observation as a supporting activity in cold regions offshore operations. In Chapter 1, we identified two different ice monitoring tasks, which were solved as *target tracking* and *dynamic coverage control* problems in later chapters. We have investigated the viability of using unmanned aerial vehicles as remote mobile sensors for various ice features in Chapter 2, and concluded that useful instrumentation for small aircraft is possible. The theoretical contributions include path planning designs with practical applications and experimental results.

In Chapter 3, the aerial monitoring of moving surface objects was formulated as a *target tracking* problem. A nonlinear programming approach used each object's state and parameter estimation error covariance dynamics as a basis for some information measure when minimizing the object system's uncertainty. The resulting paths were collision-free, feasible with respect to given maneuverability constraints, and remained within a convex mission domain. A hybrid field experiment successfully demonstrated the functionality of the path planning design.

Regional monitoring of a spatially distributed process has been analyzed in Chapters 4 and 5. The tasks were identified as *dynamic coverage control* problems and approached in two different ways: the nonlinear programming approach in the former chapter, and control theory design in the latter. The nonlinear programming approach enjoyed the same benefits as when solving the target tracking problem: respecting vehicle maneuverability constraints, staying inside a convex mission domain, and planning paths according to some spatial information reward dynamics.

With the control theory design approach we were able to show uniform global asymptotic stability (under some restricting conditions) of the combined mobile sensors path tracking and distributed parameter system under observation. The approach used gradient-based guidance signals that were based on local state estimation errors. These perturbing signals may give infeasible commanded behavior and are not designed for nonholonomic vehicle dynamics. This approach relied on predefined paths that were subsequently perturbed, but collision avoidance and mission domain compliance were not included in the formulation. Future work in this direction include removing the above limitations in the guidance law. It may also be interesting to relax the restricting conditions, namely adding parameter estimation of the boundary conditions and not assuming an asymptotically stable distributed parameter system. Dynamically changing the predefined paths is also expected to improve the monitoring performance.

The path planning designs show promise as sophisticated approaches in solving the defined monitoring tasks. Nevertheless, as briefly mentioned in Chapter 1.2, there are numerous challenges that need to be addressed before any commercial product even think of employing the designs in any monitoring system. The nonlinear programming approach suffer from the curse of dimensionality, so simplifying measures have been initiated to retain real-time solutions. The receding horizon approach help in creating optimization problems that solve in timely manners. The length of the optimization time interval can be adjusted to give a trade-off between solve times and greediness of the resulting paths. More specifically, the longer the horizons, the less greedy the planned paths are in general. A terminal constraint is commonly introduced to mitigate the greedy behavior. In our problems, however, we have not been successful in robustly and sufficiently reducing greediness for short horizons. Besides, when either the number of sensors or the size of the environment under surveillance increases, the optimization problem size grows accordingly. At some point it is very difficult to produce real-time paths with desired behavior and necessary frequency of re-planning. Future work may include mitigating these issues by somehow reformulating the problem, perhaps by decomposing the problem into smaller ones that can be solved in parallel.

### Possible Future Research Directions for Aerial Ice Observation

This thesis only considered a small part of the collective activity of *aerial ice observation*. Numerical solutions to the proposed path planning designs indicate that real-time capability may be displayed, but only if the size of the monitored environment and number of unmanned vehicles both are kept relatively small. Thus, to fully enjoy the capabilities of the developed algorithms, they must be implemented with care. This includes providing the path planners with deliberately designed tasks that take the limitations into consideration. This restriction may indicate that a higher-level intelligent activity should be responsible for assigning tailored tasks. This activity is part of *dynamic mission planning*, which was defined in Chapter 1. In general, dynamic mission planning involves human operators that are responsible for allocating top-level missions and monitoring the results. An interesting future research activity may be on an intermediate level: given a complex mission that consists of many different tasks, how can these tasks be partitioned into smaller objectives and distributed among available resources, for instance a limited pool of unmanned aerial vehicles. In this setting, the intermediate logic is responsible for dynamically manipulating the lower-level path planning activity, like those presented herein, so that the complex mission completes successfully. Rowaihy et al. (2007) may serve as a starting point for this activity.

# Bibliography


Acevo-Herrera, R., Aguasca, A., Bosch-Lluis, X., Camps, A., Martínez-Fernández, J., Sánchez-Martín, N., and Pérez-Gutiérrez, C. (June 2010). "Design and First Results of an UAV-Borne L-Band Radiometer for Multiple Monitoring Purposes". In: *Remote Sensing* 2.7, pp. 1662–1679. ISSN: 2072-4292. DOI: 10.3390/rs2071662.

Akyildiz, I. F., Pompili, D., and Melodia, T. (May 2005). "Underwater acoustic sensor networks: research challenges". In: *Ad Hoc Networks* 3.3, pp. 257–279. ISSN: 1570-8705. DOI: 10.1016/j.adhoc.2005.01.004.

AMOS (July 29, 2014). *Center for Autonomous Marine Operations and Systems*. URL: http://www.ntnu.edu/amos/centre-for-autonomous-marine-operations-and-systems.

Andersson, J., Åkesson, J., and Diehl, M. (2012). "CasADi: A Symbolic Package for Automatic Differentiation and Optimal Control". In: *Recent Advances in Algorithmic Differentiation*. Ed. by Forth, S., Hovland, P., Phipps, E., Utke, J., and Walther, A. Vol. 87. Lecture Notes in Computational Science and Engineering. Berlin Heidelberg, Germany: Springer-Verlag, pp. 297–307. ISBN: 978-3-642-30022-6. DOI: 10.1007/978-3-642-30023-3_27.

Arctic Marine Solutions (July 21, 2014). URL: www.arcticmarinesolutions.se.

Asmus, K. W., Koonar, A., and MacDonald, S. (May 13–15, 1996). "Ice-Vu: an integrated data communications and image analysis system". In: *Proceedings of the Fifth International Conference on Satellite Systems for Mobile Communications and Navigation*. Orlando, FL, USA, pp. 191–194. ISBN: 978-0-852-96658-7. DOI: 10.1049/cp:19960438.

Beard, R. W. and McLain, T. W. (2012). *Small Unmanned Aircraft*. Princeton, NJ, USA: Princeton University Press. ISBN: 978-0-691-14921-9.

Beaven, S. G., Gogineni, S., and Carsey, F. D. (Sept. 1996). "Fusion of Satellite Active and Passive Microwave Data for Sea Ice Type Concentration Estimates". In: *IEEE Transactions on Geoscience and Remote Sensing* 34.5, pp. 1172–1183. ISSN: 0196-2892. DOI: 10.1109/36.536534.

Betts, J. T. (2010). *Practical Methods for Optimal Control and Estimation Using Nonlinear Programming*. 2nd ed. Philadelphia, PA, USA: Society for Industrial

and Applied Mathematics. ISBN: 978-0-898-71688-7. DOI: 10.1137/1.9780898718577.

Biegler, L. T. (Mar. 1984). "Solution of dynamic optimization problems by successive quadratic programming and orthogonal collocation". In: *Computers and Chemical Engineering* 8.3–4, pp. 243–248. ISSN: 0098-1354. DOI: 10.1016/0098-1354(84)87012-X.

— (2010). *Nonlinear Programming: Concepts, Algorithms & Applications to Chemical Processes*. Philadelphia, PA, USA: Society for Industrial and Applied Mathematics. ISBN: 978-0-898-71702-0. DOI: 10.1137/1.9780898719383.

Bigg, G. R., Wadley, M. R., Stevens, D. P., and Johnson, J. A. (Oct. 1997). "Modelling the dynamics and thermodynamics of icebergs". In: *Cold Regions Science and Technology* 26.2, pp. 113–135. ISSN: 0165-232X. DOI: 10.1016/S0165-232X(97)00012-8.

Bogdanov, A. V., Sandven, S., Johannessen, O. M., Alexandrov, V. Y., and Bobylev, L. P. (July 2005). "Multisensor Approach to Automated Classification of Sea Ice Image Data". In: *IEEE Transactions on Geoscience and Remote Sensing* 43.7, pp. 1648–1664. ISSN: 0196-2892. DOI: 10.1109/TGRS.2005.846882.

Bradski, G. (Nov. 1, 2000). "The OpenCV Library". In: *Dr. Dobb's Journal of Software Tools*. URL: http://www.drdobbs.com/open-source/the-opencv-library/184404319#.

Brooks, A. N. and Hughes, T. J. R. (Sept. 1982). "Streamline upwind/Petrov-Galerkin formulations for convection dominated flows with particular emphasis on the incompressible Navier-Stokes equations". In: *Computer Methods in Applied Mechanics and Engineering* 32.1–3, pp. 199–259. ISSN: 0045-7825. DOI: 10.1016/0045-7825(82)90071-8.

Burns, J. A., Cliff, E. M., and Rautenberg, C. (June 24–26, 2009). "A Distributed Parameter Control Approach to Optimal Filtering and Smoothing with Mobile Sensor Networks". In: *Proceedings of the 17th Mediterranean Conference on Control & Automation, MED '09*. Thessaloniki, Greece, pp. 181–186. ISBN: 978-1-424-44685-8. DOI: 10.1109/MED.2009.5164536.

CAA–Norway (July 29, 2014). *Civil Aviation Authority – Norway, RPAS-FAQ*. URL: www.luftfartstilsynet.no/selvbetjening/allmennfly/RPAS-FAQ/.

Chen, C.-T. (1999). *Linear System Theory and Design*. 3rd ed. New York, NY, USA: Oxford University Press. ISBN: 0-19-511777-8.

Chen, Y., Moore, K. L., and Song, Z. (Apr. 12, 2004). "Diffusion boundary determination and zone control via mobile actuator-sensor networks (MAS-net): challenges and opportunities". In: *Proceedings of the SPIE 5421, Intelligent Computing: Theory and Applications II, 102*. Orlando, FL, USA, pp. 102–113. ISBN: 978-0-819-45344-0. DOI: 10.1117/12.543814.

Choi, H. and How, J. P. (Aug. 2010). "Continuous trajectory planning of mobile sensors for informative forecasting". In: *Automatica* 46.8, pp. 1266–1275. ISSN: 0005-1098. DOI: 10.1016/j.automatica.2010.05.004.

Cloud Cap Technology (Sept. 14, 2013). URL: http://www.cloudcaptech.com.

Comiso, J. C., Grenfell, T. C., Bell, D. L., Lange, M. A., and Ackley, S. F. (Aug. 1989). "Passive microwave in situ observations of winter Weddell sea ice". In: *Journal of Geophysical Research* 94.C8, pp. 10891–10905. ISSN: 2169-9291. DOI: 10.1029/JC094iC08p10891.

Cortés, J., Martínez, S., and Bullo, F. (Oct. 2005). "Spatially-distributed coverage optimization and control with limited-range interations". In: *ESAIM: Control, Optimisation and Calculus of Variations* 11.4, pp. 691–719. ISSN: 1292-8119. DOI: 10.1051/cocv:2005024.

Cosmo-SkyMed (Feb. 11, 2011). URL: http://www.cosmo-skymed.it/en/.

Court, J., Demetriou, M. A., and Gatsonis, N. (June 27–29, 2012). "Spatial Gradient Measurement through Length Scale Estimation for the Tracking of a Gaseous Source". In: *Proceedings of the American Control Conference, ACC '12*. Elizabeth, Montréal, Canada, pp. 2984–2989. ISBN: 978-1-457-71095-7. DOI: 10.1109/ACC.2012.6315192.

CPS Steering Group (May 6, 2008). *Cyber-Physical Systems*. URL: http://varma.ece.cmu.edu/summit/CPS-Executive-Summary.pdf.

Crowe, W., Davis, K. D., la Cour-Harbo, A., Vihma, T., Lesenkov, S., Eppi, R., Weatherhead, E. C., Liu, P., Raustein, M., Abrahamsson, M., Johansen, K.-S., and Marshall, D. (Dec. 2012). *Enabling Science use of Unmanned Aircraft Systems for Arctic Environmental Monitoring*. Tech. rep. 6. Oslo, Norway: Arctic Monitoring and Assessment Programme (AMAP). EPRINT: http://amap.no/documents/download/938.

Daescu, D. N. and Navon, I. M. (Feb. 2004). "Adaptive observations in the context of 4D-var data assimilation". In: *Meteorology and Atmospheric Physics* 85.111, pp. 205–226. ISSN: 1436-5065. DOI: 10.1007/s00703-003-0011-5.

Death, R., Siegert, M. J., Bigg, G. R., and Wadley, M. R. (June 2006). "Modelling iceberg trajectories, sedimentation rates and meltwater input to the ocean from the Eurasian Ice Sheet at the Last Glacial Maximum". In: *Palaeogeography, Palaeoclimatology, Palaeoecology* 236.1–2, pp. 135–150. ISSN: 0031-0182. DOI: 10.1016/j.palaeo.2005.11.040.

Demetriou, M. A. (July 9–12, 2007). "Process estimation and moving source detection in 2-D diffusion processes by scheduling of sensor networks". In: *Proceedings of the American Control Conference, ACC '07*. New York, NY, USA, pp. 3432–3437. ISBN: 1-4244-0989-6. DOI: 10.1109/ACC.2007.4282247.

— (July 2010). "Guidance of Mobile Actuator-Plus-Sensor Networks for Improved Control and Estimation of Distributed Parameter Systems". In: *IEEE Transactions on Automatic Control* 55.7, pp. 1570–1584. ISSN: 0018-9286. DOI: 10.1109/TAC.2010.2042229.

Demetriou, M. A. and Hussein, I. I. (Feb. 2009). "Estimation of Spatially Distributed Processes Using Mobile Spatially Distributed Sensor Network". In:

*SIAM Journal on Control and Optimization* 48.1, pp. 266–291. ISSN: 1095-7138. DOI: 10.1137/060677884.

Demetriou, M. A. and Ucinski, D. (June 29–1, 2011). "State estimation of spatially distributed processes using mobile sensing agents". In: *Proceedings of the American Control Conference, ACC '11*. San Francisco, CA, USA, pp. 1770–1776. ISBN: 978-1-457-70081-1. DOI: 10.1109/ACC.2011.5991065.

Dunavant, D. A. (June 1985). "High degree efficient symmetrical Gaussian quadrature rules for the triangle". In: *International Journal for Numerical Methods in Engineering* 21.6, pp. 1129–1148. ISSN: 1097-0207. DOI: 10.1002/nme.1620210612.

Du, Q., Faber, V., and Gunzburger, M. (Jan. 1999). "Centroidal Voronoi Tessellations: Applications and Algorithms". In: *SIAM Review* 41.4, pp. 637–676. ISSN: 0036-1445. DOI: 10.1137/S0036144599352836.

Edmond, C., Liferov, P., and Metge, M. (Feb. 7–9, 2011). "Ice and Iceberg Management Plans for Shtokman Field". In: *Proceedings of the OTC Arctic Technology Conference 2011*. Houston, TX, USA, pp. 1–9. ISBN: 978-1-613-99172-5. DOI: 10.4043/22103-MS.

Eicken, H., Gradinger, R., Salganek, M., K., S., Perovich, D., and Leppäranta, eds. (2009). *Field Techniques for Sea Ice Research*. Fairbanks, AK, USA: University of Alaska Press. ISBN: 1-6022-3059-5.

Eik, K. (Oct. 2008). "Review of Experiences within Ice and Iceberg Management". In: *Journal of Navigation* 61.4, pp. 557–572. ISSN: 0373-4633. DOI: 10.1017/S0373463308004839.

— (Feb. 2009). "Iceberg drift modelling and validation of applied metocean hindcast data". In: *Cold Regions Science and Technology* 57.2–3, pp. 67–90. ISSN: 0165-232X. DOI: 10.1016/j.coldregions.2009.02.009.

— (2010). "Ice Management in Arctic Offshore Operations and Field Developments". PhD thesis. Trondheim, Norway: Norwegian University of Science and Technology, p. 214. ISBN: 978-8-247-12403-1. EPRINT: http://www.diva-portal.org/smash/get/diva2:403006/FULLTEXT02.

— (Feb. 2011). "Sea-ice management and its impact on the design of offshore structures". In: *Cold Regions Science and Technology* 65.2, pp. 172–183. ISSN: 0165-232X. DOI: 10.1016/j.coldregions.2010.10.009.

Eik, K. and Løset, S. (May 31–5, 2009). "Specification for a Subsurface Ice Intelligence System". In: *Proceedings of the ASME 2009 28th International Conference on Ocean, Offshore and Arctic Engineering, OMAE2009*. Honolulu, Hawaii, USA, pp. 103–109. ISBN: 978-0-791-83844-0. DOI: 10.1115/OMAE2009-79606.

Elachi, C. and van Zyl, J. J. (2006). *Introduction to the Physics and Techniques of Remote Sensing*. 2nd ed. Hoboken, NJ, USA: John Wiley & Sons Inc. ISBN: 978-0-471-47569-9.

Ern, A. and Guermond, J.-L. (2004). *Theory and Practice of Finite Elements*. New York, NY, USA: Springer-Verlag. ISBN: 0-3872-0574-8.

Evensen, G. (May 1994). "Sequential data assimilation with a nonlinear quasi-geostrophic model using Monte Carlo methods to forecast error statistics". In: *Journal of Geophysical Research* 99.C5, pp. 10143–10162. ISSN: 2169-9291. DOI: 10.1029/94JC00572.

Evensen, G. (Nov. 2003). "The Ensemble Kalman Filter: theoretical formulation and practical implementation". In: *Ocean Dynamics* 53.4, pp. 343–367. ISSN: 1616-7228. DOI: 0.1007/s10236-003-0036-9.

Flett, D. G. (Sept. 8–12, 2003). "Operational use of SAR at the Canadian Ice Service: Present operations and a look to the future". In: *Proceedings of the Second Workshop on Coastal and Marine Applications of SAR*. Svalbard, Norway, pp. 183–198. ISBN: 9-2909-2876-X. EPRINT: http://earth.esa.int/workshops/cmasar_2003/papers/E20flet.pdf.

FLIR (Feb. 14, 2011). *FLIR Photon 640*. URL: http://www.flir.com.
— (May 2, 2013). *FLIR Tau 2*. URL: http://www.flir.com.

Fossen, T. I. (2011). *Handbook of Marine Craft Hydrodynamics and Motion Control*. Hoboken, NJ, USA: John Wiley & Sons Inc. ISBN: 978-1-119-99149-6.

Frew, E. W. and Brown, T. X. (Mar. 2009). "Networking Issues for Small Unmanned Aircraft Systems". In: *Journal of Intelligent and Robotic Systems* 54.1–3, pp. 21–37. ISSN: 1573-0409. DOI: 10.1007/s10846-008-9253-2.

Gautier, D. L., Bird1, K. J., Charpentier, R. R., Grantz, A., Houseknecht, D. W., Klett, T. R., Moore, T. E., Pitman, J. K., Schenk, C. J., Schuenemeyer, J. H., Sørensen, K., Tennyson, M. E., Valin, Z. C., and Wandrey, C. J. (May 2009). "Assessment of Undiscovered Oil and Gas in the Arctic". In: *Science* 324.5931, pp. 1175–1179. DOI: 10.1126/science.1169467.

Geiger, B. (2009). "Unmanned Aerial Vehicle Trajectory Planning with Direct Methods". PhD thesis. Bellefonte, PA, USA: Department of Aerospace Engineering, The Pennsylvania State University, p. 155.

Gene H Golub, J. H. W. (Apr. 1969). "Calculation of Gauss Quadrature Rules". In: *Mathematics of Computation* 23.106, pp. 221–230. ISSN: 1088-6842. EPRINT: http://www.jstor.org/stable/2004418.

Georges, D. (July 17–19, 2013). "Optimal Location of Mobile Sensors for Environmental Monitoring". In: *Proceedings of 2013 European Control Conference (ECC)*. Zurich, Switzerland, pp. 1280–1285. ISBN: 978-3-033-03962-9. EPRINT: http://ieeexplore.ieee.org/stamp/stamp.jsp?tp=&arnumber=6669302.

Geuzaine, C. and Remacle, J. (Sept. 2009). "Gmsh: A 3-D finite element mesh generator witch built-in pre- and post-processing facilities". In: *International Journal for Numerical Methods in Engineering* 79.11, pp. 1309–1331. ISSN: 1097-0207. DOI: 10.1002/nme.2579.

Gürtner, A., Baardson, B. H. H., Kaasa, G.-O., and Lundin, E. (July 1–6, 2012). "Aspects of Importance Related to Arctic DP Operations". In: *Proceedings of the ASME 2012 31th International Conference on Ocean, Offshore and Arctic*

*Engineering, OMAE2012*. Rio de Janeiro, Brazil, pp. 617–623. ISBN: 978-0-791-84493-9. DOI: 10.1115/OMAE2012-84226.

Hamilton, J., Holub, C., Blunt, J., Mitchell, D., and Kokkinis, T. (Feb. 7–9, 2011). "Ice Management for Support of Arctic Floating Operations". In: *Proceedings of the OTC Arctic Technology Conference 2011*. Houston, TX, USA, pp. 1–12. ISBN: 978-1-613-99172-5. DOI: 10.4043/22105-MS.

Haugen, J., Grøtli, E. I., and Imsland, L. (Oct. 3–5, 2012). "State Estimation of Ice Thickness Distribution Using Mobile Sensors". In: *Proceedings of 2012 IEEE Multi-Conference on Systems and Control*. Dubrovnik, Croatia, pp. 336–343. ISBN: 978-1-467-34505-3. DOI: 10.1109/CCA.2012.6402649.

Haugen, J. and Imsland, L. (July 17–19, 2013a). "Optimization-Based Autonomous Remote Sensing of Surface Objects Using an Unmanned Aerial Vehicle". In: *Proceedings of 2013 European Control Conference (ECC)*. Zurich, Switzerland, pp. 1242–1249. ISBN: 978-3-033-03962-9. EPRINT: http://ieeexplore.ieee.org/stamp/stamp.jsp?tp=&arnumber=6669610.

— (Nov. 20–22, 2013b). "UAV Path Planning for Multitarget Tracking with Experiments". In: *Proceedings of the 2nd IFAC Workshop on Research, Development and Education of Unmanned Aerial Systems (2013)*. Compiègne, France, pp. 316–323. ISBN: 978-3-302-82357-1. DOI: 10.3182/20131120-3-FR-4045.00061.

— (Oct. 2014a). "Monitoring an Advection-Diffusion Process Using Aerial Mobile Sensors". In: *Unmanned Systems*. Submitted. ISSN: 2301-3850.

— (2014b). "Monitoring Moving Objects Using Aerial Mobile Sensors". In: *IEEE Transaction on Control Systems Technology*. Accepted. ISSN: 1063-6536.

Haugen, J., Imsland, L., Løset, S., and Skjetne, R. (June 19–24, 2011). "Ice Observer System for Ice Management Operations". In: *Proceedings of the Twenty-first (2011) International Offshore and Polar Engineering Conference*. Maui, HI, USA, pp. 1120–1127. ISBN: 978-1-880-65396-8.

Heil, P., Fowler, C. W., Maslanik, J. A., Emery, W. J., and Allison, I. (Jan. 2001). "A comparison of East Antarctic sea-ice motion derived using drifting buoys and remote sensing". In: *Annals of Glaciology* 33.1, pp. 139–144. ISSN: 1727-5644. DOI: 10.3189/172756401781818374.

Hendricks, S., Haas, C., Göbell, S., and Haapala, J. (2006). "Laser and radar (LaRa) Surface Elevation Retrieval and EM Sea Ice Thickness Measurements in the Baltic Sea". In: *European Geosciences Union - General Assembly*. Vienna, Austria. DOI: 10013/epic.33193.d001.

Hindmarsh, A. C., Brown, P. N., Grant, K. E., Lee, S. L., Serban, R., Shumaker, D. E., and Woodward, C. S. (Sept. 2005). "SUNDIALS : Suite of Nonlinear and Differential / Algebraic Equation Solvers". In: *ACM Transactions on Mathematical Software* 31.3, pp. 363–396. ISSN: 1557-7295. DOI: 10.1145/1089014.1089020.

Horn, R. A. and Johnson, C. R. (1994). *Topics in Matrix Analysis*. Cambridge, UK: Cambridge University Press. ISBN: 0-5214-6716-6.

HSL (2011). *A collection of Fortran codes for large scale scientific computation.* URL: http://www.hsl.rl.ac.uk.

Hussein, I. I. and Stipanović, D. M. (July 2007). "Effective Coverage Control for Mobile Sensor Networks with Guaranteed Collision Avoidance". In: *IEEE Transaction on Control Systems Technology* 15.4, pp. 642–657. ISSN: 1063-6536. DOI: 10.1109/TCST.2007.899155.

ICEMON (Feb. 1, 2011). *ICEMON - Sea ice monitoring in the polar regions.* URL: http://www.icemon.org/.

IEEE (1984). *IEEE Standard Letter Designations for Radar-Frequency Bands.* IEEE Std 521-1984.

ImSAR (Feb. 14, 2011). *ImSAR NanoSAR B.* URL: http://www.imsar.com.

Iserles, A. (1996). *A First Course in the Numerical Analysis of Differential Equations.* Cambridge, UK: Cambridge University Press. ISBN: 0-5215-5655-4.

ISRO (Feb. 12, 2011). *Indian Space Research Organization. Miniature Synthetic Aperture Radar (Mini-SAR).* URL: http://www.isro.org/chandrayaan/htmls/minisar_nasa.htm.

Jenssen, N. A., Muddesitti, S., Phillips, D., and Backstrom, K. (Oct. 13–14, 2009). "DP In Ice Conditions". In: *Proceedings of the Dynamic Positioning Conference 2009.* Houston, TX, USA, pp. 1–10. ISBN: 978-1-617-38903-0. EPRINT: http://www.dynamic-positioning.com/dp2009/arctic_jenssen.pdf.

Johannessen, O. M., Alexandrov, V. Y., Frolov, I. Y., Sandven, S., Pettersson, L. H., Bobylev, L. P., Kloster, K., Smirnov, V. G., Mironov, Y. U., and Babich, N. G. (2007). "Remote Sensing of Sea Ice in the Northern Sea Route". In: Chichester, UK: Springer-Verlag. Chap. History of the Northern Sea Route. ISBN: 3-5402-4448-4.

Johannessen, O. M., Sandven, S., Pettersson, L. H., Kloster, K., Hamre, T., Solhaug, J., Volkov, A. M., Asmus, V., Milekhin, O. E., Krovotyntsev, V. A., Grischenko, V. D., Smirnov, V. G., Bobylev, L. P., Melentyev, V. V., and Alexandrov, V. (Aug. 3–8, 1997). "ICEWATCH-real-time sea ice monitoring of the Northern Sea Route using satellite radar technology". In: *Proceedings of 1997 IEEE International Geoscience and Remote Sensing Symposium, Remote Sensing - A Scientific Vision for Sustainable Development, IGARSS '97.* Vol. 4, pp. 1681–1685. ISBN: 0-7803-3836-7. DOI: 10.1109/IGARSS.1997.609022.

John, V. and Knobloch, P. (Mar. 2007). "On spurious oscillations at layers diminishing (SOLD) methods for convection–diffusion equations: Part I – A review". In: *Computer Methods in Applied Mechanics and Engineering* 196.17–20, pp. 2197–2215. ISSN: 0045-7825. DOI: 10.1016/j.cma.2006.11.013.

John, V. and Schmeyer, E. (Dec. 2008). "Finite element methods for time-dependent convection-diffusion-reaction equations with small diffusion". In: *Computer Methods in Applied Mechanics and Engineering* 198.3–4, pp. 475–494. ISSN: 0045-7825. DOI: 10.1016/j.cma.2008.08.016.

Kaheil, Y. H., Gill, M. K., McKee, M., Bastidas, L. A., and Rosero, E. (May 2008). "Downscaling and Assimilation of Surface Soil Moistrue Using Ground Truth Measurements". In: *IEEE Transactions on Geoscience and Remote Sensing* 46.5, pp. 1375–1384. ISSN: 0196-2892. DOI: 10.1109/TGRS.2008.916086.

Keghouche, I., Bertino, L., and Lisæter, K. (Oct. 2009). "Parameterization of an Iceberg Drift Model in the Barents Sea". In: *Journal of Atmospheric and Oceanic Technology* 26.10, pp. 2216–2227. ISSN: 1520-0426. DOI: 10.1175/2009JTECHO678.1.

Keinonen, A. J. (May 5–8, 2008). "Ice Management for Ice Offshore Operations". In: *Proceedings of the OTC Arctic Technology Conference 2008*. Houston, TX, USA, pp. 1–15. ISBN: 978-1-555-63224-3. DOI: 10.4043/19275-MS.

Khalil, H. K. (2002). *Nonlinear Systems*. 3rd ed. Upper Saddle River, NJ, USA: Prentice-Hall Inc. ISBN: 0-1306-7389-7.

Kincaid, D. and Cheney, W. (2009). *Numerical Analysis*. 3rd ed. Providence, RI, USA: American Mathematical Society. ISBN: 978-0-821-84788-6.

Klesh, A. T., Kabamba, P. T., and Girard, A. R. (June 10–12, 2009). "Optimal Path Planning for Uncertain Exploration". In: *Proceedings of the American Control Conference, ACC '09*. St. Louis, MO, pp. 2421–2426. ISBN: 978-1-424-44523-3. DOI: 10.1109/ACC.2009.5160286.

Kubat, I., Collins, A., and Timco, G. W. (June 27–30, 2007a). "Year-round Shipping in the Canadian Arctic: Ice Conditions and Regulatory Requirements". In: *Proceedings of the 19th International Conference on Port and Ocean Engineering under Arctic Conditions (POAC'07)*. Dalian, China, pp. 446–456. ISBN: 978-7-561-13631-7.

Kubat, I., Sayed, M., Savage, S. B., and Carriers, T. (June 2005). "An Operational Model of Iceberg Drift". In: *International Journal of Offshore and Polar Engineering* 15.2, pp. 125–131. ISSN: 1053-5381.

Kubat, I., Sayed, M., Savage, S. B., Carriers, T., and Crocker, G. (July 1–6, 2007b). "An Operational Iceberg Deterioration Model". In: *Proceedings of the Seventeenth (2007) International Offshore and Polar Engineering Conference*. Lisbon, Portugal, pp. 652–657. ISBN: 978-1-880-65368-5.

Kuehnlein, W. L. (May 4–7, 2009). "Philosophies for Dynamic Positioning in Ice-Covered Waters". In: *Proceedings of the OTC Arctic Technology Conference 2009*. Houston, TX, USA, pp. 1–7. ISBN: 978-1-555-63224-1. DOI: 10.4043/20019-MS.

Leachtenauer, J. C. and Driggers, R. G. (2001). *Surveillance and Reconnaissance Imaging Systems: Modeling and Performance Prediction*. Norwood, MA, USA: Artech House. ISBN: 978-1-580-53132-0.

Leppäranta, M. (Jan. 1993). "A review of analytical models of sea-ice growth". In: *Atmosphere-Ocean* 31.1, pp. 123–138. ISSN: 0705-5900. DOI: 10.1080/07055900.1993.9649465.

— (2005). *The Drift of Sea Ice*. 1st ed. Chichester, UK: Springer-Verlag. ISBN: 978-3-540-40881-9.
— (2011). *The Drift of Sea Ice*. 2nd ed. Chichester, UK: Springer-Verlag. ISBN: 978-3-642-04683-4.

Looker, J. R. (Dec. 2008). *Minimum Paths to Interception of a Moving Target when Constrained by Turning Radius*. Tech. rep. DSTO-TR-2227. Canberra, Australia: Defence Science and Technology Organisation. EPRINT: `http://dspace.dsto.defence.gov.au/dspace/bitstream/1947/9741/1/DSTO-TR-2227PR.pdf`.

Loría, A., Panteley, E., Popovíc, D., and Teel, A. R. (Feb. 2005). "A Nested Matrosov Theorem and Persistency of Excitation for Uniform Convergence in Stable Nonautonomous Systems". In: *IEEE Transactions on Automatic Control* 50.2, pp. 183–198. ISSN: 0018-9286. DOI: `10.1109/TAC.2004.841939`.

Løset, S., Shkhinek, K. N., Gudmestad, O. T., and Høyland, K. V. (2006). *Actions From Ice on Arctic Offshore and Coastal Structures*. St. Petersburg, Russia: LAN. ISBN: 5-8114-0703-3.

Løset, S. (1993). "Some aspects of floating ice related sea surface operations in the Barents Sea". PhD thesis. Trondheim, Norway: Norwegian University of Science and Technology.

Lubin, D. and Massom, R. (2006). *Polar Remote Sensing, Volume I: Atmosphere and Oceans*. Berlin Heidelberg, Germany: Springer-Verlag. ISBN: 3-5404-3097-0.

Maijala, P., Moore, J. C., Hjelt, S. E., Pälli, A., and Sinisalo, A. (May 27–30, 1998). "GPR investigations of glaciers and sea ice in the Scandinavian Arctic". In: *Proceedings of the 7th International Conference on Ground-Penetrating Radar, GPR98*. Lawrence, Kansas, USA, pp. 143–148. ISBN: 0-9363-5216-7.

Majumdar, S. J., Bishop, C. H., Etherton, B. J., and Toth, Z. (Mar. 2002). "Adaptive Sampling with the Ensemble Transform Kalman Filter. Part II: Field Programming Implementation". In: *Monthly Weather Review* 130.3, pp. 1356–1369. ISSN: 1520-0493. DOI: `10.1175/1520-0493(2002)130<1356:ASWTET>2.0.CO;2`.

Maritime Robotics (Sept. 13, 2013). URL: `http://www.maritimerobotics.com`.

McClintock, J., McKenna, R., and Woodworth-Lynas, C. (May 2007). *Grand Banks Iceberg Management. PERD/CHC Report 20-84*. Tech. rep. AMEC Earth & Environment, St. John's, NL, R.F McKenna & Associates, Wakefield, QC, and PETRA International Ltd., Cupids, NL. EPRINT: `ftp://ftp2.chc.nrc.ca/CRTreports/GB_Iceberg_Manage_Overview_07.pdf`.

MDL (Feb. 14, 2011). *MDL LasarAce ILM R300*. URL: `http://www.mdl.co.uk`.

Metrikin, I., Løset, S., Jenssen, N. A., and Kerkeni, S. (Mar. 2013). "Numerical Simulation of Dynamic Positioning in Ice". In: *Marine Technology Society Journal* 47.2, pp. 14–30. ISSN: 0025-3324. DOI: `10.4031/MTSJ.47.2.2`.

Moran, K., Backman, J., and Farrell, J. W. (Mar. 7, 2006). "Deepwater drilling in the Arctic Ocean's permanent sea ice". In: *Proceedings of IODP, 302*. Ed. by

Backman, J., Moran, K., McInroy, D. B., Mayer, L. A., and the Expedition 302 Scientists. Edinburgh, UK: Integraded Ocean Drilling Program Management Int., Inc., pp. 1–13. DOI: 10.2204/iodp.proc.302.106.2006.

Moran, M. S., Inoue, Y., and Barnes, E. M. (Sept. 1997). "Opportunities and Limitations for Image-Based Remote Sensing in Precision Crop Management". In: *Remote Sensing of Environment* 61.3, pp. 319–346. ISSN: 0034-4257. DOI: 10.1016/S0034-4257(97)00045-X.

Morbidi, F. and Mariottini, G. L. (Sept. 2013). "Active Target Tracking and Cooperative Localization for Teams of Aerial Vehicles". In: *IEEE Transaction on Control Systems Technology* 21.5, pp. 1694–1707. ISSN: 1063-6536. DOI: 10.1109/TCST.2012.2221092.

Mountain, D. G. (Feb. 1980). "On predicting iceberg drift". In: *Cold Regions Science and Technology* 1.3–4, pp. 273–282. ISSN: 0165-232X. DOI: 10.1016/0165-232X(80)90055-5.

Napoleoni, J. P. (Aug. 1979). "The dynamics of iceberg drift". MA thesis. Vancouver, Canada: The University of British Columbia. DOI: 2429/22707.

Netzband, M., Stefanov, W. L., and Redman, C., eds. (2007). *Applied Remote Sensing for Urban Planning, Governance and Sustainability*. Berlin Heidelberg, Germany: Springer-Verlag. ISBN: 978-3-540-25546-8.

Nikon (Feb. 14, 2011). *Nikon D300s*. URL: http://www.nikon.com.

Norut (May 13, 2014). *Norut UAV remote sensing*. URL: http://norut.no/en/satelitter-fjernmaling-og-ubemannede-fly.

O'Connell, B. J. (2008). *Marine Radar for Improved Ice Detection*. Tech. rep. Ottawa, Ontario, Canada: Canadian Coast Guard. EPRINT: http://www.dfo-mpo.gc.ca/Library/343421.pdf.

Omatu, S., Koide, S., and Soeda, T. (Aug. 1978). "Optimal Sensor Location Problem for a Linear Distributed Parameter System". In: *IEEE Transactions on Automatic Control* 24.4, pp. 665–673. ISSN: 0018-9286. DOI: 10.1109/TAC.1978.1101826.

Paden, B. and Panja, R. (June 1988). "Globally asymptotically stable PD+ controller for robot manipulators". In: *International Journal of Control* 47.6, pp. 1697–1712. ISSN: 1366-5820. DOI: 10.1080/00207178808906130.

Palmer, T. N., Gelaro, R., Barkmeijer, J., and Buizza, R. (Feb. 1998). "Singular Vectors, Metrics and Adaptive Observations". In: *Journal of the Atmospheric Sciences* 55.4, pp. 633–653. ISSN: 1520-0469. DOI: 10.1175/1520-0469(1998)055<0633:SVMAAO>2.0.CO;2.

Parker, L. E. (Jan. 1999). "Cooperative Robotics for Multi-Target Observation". In: *Intelligent Automation and Soft Computing* 5.1, pp. 5–19. ISSN: 2326-005X. DOI: 10.1080/10798587.1999.10750747.

Partington, K. C. (July 2000). "A Data Fusion Algorithm for Mapping Sea-Ice Concentrations from Special Sensor Microwave/Imager Data". In: *IEEE Transac-*

*tions on Geoscience and Remote Sensing* 38.4, pp. 1947–1958. ISSN: 0196-1958. DOI: 10.1109/36.851776.

Patel, R. B. and Goulart, P. J. (Jan. 2011). "Trajectory Generation for Aircraft Avoidance Maneuvers Using Online Optimization". In: *Journal of Guidance, Control, and Dynamics* 34.1, pp. 218–230. ISSN: 0731-5090. DOI: 10.2514/1.49518.

Quintero, S. A. P., Papi, F., Klein, D. J., Chisci, L., and Hespanha, J. P. (Dec. 15–17, 2010). "Optimal UAV Coordination for Target Tracking Using Dynamic Programming". In: *Proceedings of the 49th IEEE Conference on Decision and Control*. Atlanta, GA, pp. 4541–4546. ISBN: 978-1-424-47745-6. DOI: 10.1109/CDC.2010.5717933.

Rao, C. V., Rawlings, J. B., and Mayne, D. Q. (Feb. 2003). "Constrained State Estimation for Nonlinear Discrete-Time Systems: Stability and Moving Horizon Approximations". In: *IEEE Transactions on Automatic Control* 48.2, pp. 246–258. ISSN: 0018-9286. DOI: 10.1109/TAC.2002.808470.

Rathinam, S., Sengupta, R., and Darbha, S. (Jan. 2007). "A Resource Allocation Algorithm for Multivehicle Systems with Nonholonomic Constraints". In: *IEEE Transactions on Automation Science and Engineering* 4.1, pp. 98–104. ISSN: 1545-5955. DOI: 10.1109/TASE.2006.872110.

Ray, S. S. (2013). *Graph Theory with Algorithms and its Applications*. New Delhi, India: Springer. ISBN: 978-8-132-20750-4. DOI: 10.1007/978-81-322-0750-4.

Reuder, J., Brisset, P., Jonassen, M., Müller, M., and Mayer, S. (Apr. 2009). "The Small Unmanned Meteorological Observer SUMO: A new tool for atmospheric boundary layer research". In: *Meteorologische Zeitschrift* 18.2, pp. 141–147. ISSN: 0941-2948. DOI: 10.1127/0941-2948/2009/0363.

RIEGL (Feb. 14, 2011). *RIEGL LMS-Q240i*. URL: http://www.riegl.com.

Roke (Feb. 14, 2011). *Roke Miniature Radar Altimeter*. URL: www.roke.co.uk.

Rowaihy, H., Eswaran, S., Johnson, M., Verma, D., Bar-Noy, A., Brown, T., and Porta, T. L. (Apr. 9–13, 2007). "A Survey of Sensor Selection Schemes in Wireless Sensor Networks". In: *Proceedings of SPIE Defense and Security Symposium – Unattended Ground, Sea, and Air Sensor Technologies and Applications IX*. Orlando, FL, USA, pp. 1–13. EPRINT: http://citeseerx.ist.psu.edu/viewdoc/summary?doi=10.1.1.100.6353.

Sanderson, T. J. O. (1988). *Ice Mechanics: Risk to Offshore Structures*. London, UK: Graham & Trotman. ISBN: 0-8601-0785-X.

Savla, K., Frazzoli, E., and Bullo, F. (July 2008). "Traveling Salesperson Problems for the Dubins Vehicle". In: *IEEE Transactions on Automatic Control* 53.6, pp. 1378–1391. ISSN: 0018-9286. DOI: 10.1109/TAC.2008.925814.

Sheykin, I. B. (June 14–18, 2010). "Icebreaker Reconnaissance for Ice Mangement: offshore experience". In: *Proceedings of the 20th IAHR International Symposium on Ice*. Lahti, Finland, pp. 525–536. ISBN: 978-1-629-93395-5.

Simicon (Feb. 13, 2011). *Simicon Arctic UAS*. URL: http://simicon.no/.

Simon, D. (May 2006). *Optimal State Estimation*. Hoboken, NJ, USA: John Wiley & Sons Inc. ISBN: 978-0-470-04534-3.

Skjetne, R., Fossen, T. I., and Kokotović, P. V. (Mar. 2004). "Robust output maneuvering for a class of nonlinear systems". In: *Automatica* 40.3, pp. 373–383. ISSN: 0005-1098. DOI: 10.1016/j.automatica.2003.10.010.

Smith, S. D. (Nov. 1993). "Hindcasting iceberg drift using current profiles and winds". In: *Cold Regions Science and Technology* 22.1, pp. 33–45. ISSN: 0165-232X. DOI: 10.1016/0165-232X(93)90044-9.

Smith, S. D. and Banke, E. G. (1983). "The influence of winds, currents and towing forces on the drift of icebergs". In: *Cold Regions Science and Technology* 6.3, pp. 241–255. ISSN: 0165-232X. DOI: 10.1016/0165-232X(83)90045-9.

Soh, L., Tsatsoulis, C., Gineris, D., and Bertoia, C. (Jan. 2004). "ARKTOS: An Intelligent System for SAR Sea Ice Image Classification". In: *IEEE Transactions on Geoscience and Remote Sensing* 42.1, pp. 229–248. ISSN: 0196-2892. DOI: 10.1109/TGRS.2003.817819.

Song, Z., Chen, Y., Liang, J., and Uciński, D. (Aug. 2–6, 2005). "Optimial Mobile Sensor Motion Planning Under Nonholonomic Constraints for Parameter Estimation of Distributed Systems". In: *Proceedings of 2005 IEEE/RSJ International Conference on Intelligent Robots and Systems*. Edmonton, Canada, pp. 3163–3168. ISBN: 0-7803-8912-3. DOI: 10.1109/IROS.2005.1545192.

Tang, Z. and Özgüner, Ü. (Oct. 2005). "Motion Planning for Multitarget Surveillance with Mobile Sensor Agents". In: *IEEE Transactions on Robotics* 21.5, pp. 898–908. ISSN: 1552-3098. DOI: 10.1109/TRO.2005.847567.

Timco, G. W., Gorman, B., Falkingham, J., and O'Connell, B. (Feb. 2005). *Scoping Study: Ice Information Requirements for Marine Transportation of Natural Gas from the High Arctic*. Tech. rep. CHC-TR-029. Ottawa, Canada: Canadian Hydraulics Centre. EPRINT: ftp://ftp2.chc.nrc.ca/CRTreports/PERD/Arctic_Trans_05.pdf.

Timco, G. W. and Gorman, R. (June 27–30, 2007). "Survey of Canadian Arctic Captains: Current Status and Research Needs". In: *Proceedings of the 19th International Conference on Port and Ocean Engineering under Arctic Conditions (POAC'07)*. Dalian, China, pp. 695–704. ISBN: 978-7-561-13631-7.

Tisdale, J., Kim, Z., and Hedrick, J. K. (June 2009). "Autonomous UAV Path Planning and Estimation". In: *IEEE Robotics and Automation Magazine* 16.2, pp. 35–42. ISSN: 1070-9932. DOI: 10.1109/MRA.2009.932529.

Tricaud, C. and Chen, Y. (June 10–12, 2009). "Optimal mobile actuator/sensor network motion strategy for parameter estimation in a class of cyber physical systems". In: *Proceedings of the American Control Conference, ACC '09*. St. Louis, MO, pp. 367–372. ISBN: 978-1-424-44523-3. DOI: 10.1109/ACC.2009.5160289.

Tricaud, C. and Chen, Y. (2012). *Optimal Mobile Sensing and Actuation Policies in Cyber-physical Systems*. London, UK: Springer-Verlag. ISBN: 978-1-447-12262-3. DOI: 10.1007/978-1-4471-2262-3_1.

UAV Factory (Sept. 13, 2013). URL: http://www.uavfactory.com.

UVSI (Feb. 13, 2011). *Unmanned Vehicle Systems International*. URL: http://www.uvs-international.org.

Vaidya, U., Rajaram, R., and S., D. (Oct. 2012). "Actuator and sensor placement in linear advection PDE with building system application". In: *Journal of Mathematical Analysis and Applications* 394.1, pp. 213–224. ISSN: 0022-247X. DOI: 10.1016/j.jmaa.2012.03.046.

Wächter, A. and Biegler, L. T. (May 2006). "On the implementation of an interior-point filter line-search algorithm for large-scale nonlinear programming". In: *Math. Programming* 106 (1), pp. 25–57. ISSN: 0025-5610. DOI: 10.1007/s10107-004-0559-y.

Wadhams, P. and Doble, M. J. (Jan. 2008). "Digital terrain mapping of the underside of sea ice from a small AUV". In: *Geophysical Research Letters* 35.L01501. ISSN: 1944-8007. DOI: 10.1029/2007GL031921.

Wang, Y. and Hussein, I. I. (2012). *Search and Classification Using Multiple Autonomous Vehicles*. London, UK: Springer-Verlag. ISBN: 978-1-447-12957-8. DOI: 10.1007/978-1-4471-2957-8_1.

WMO (1989). "WMO Sea-ice nomenclature. Terminology, codes and illustrated glossary, WMO/OMM/BMO, Rept. No. 259, TP 145. Supplement no. 5". In: *(First edition 1970 ed.)* WMO, Geneva, Switzerland.

Xianyi, Z., Qian, W., and Yunquan, Z. (Dec. 17–19, 2012). "Model-driven Level 3 BLAS Performance Optimization on Loongson 3A Processor". In: *Proceedings of 2012 IEEE 18th International Conference on Parallel and Distributed Systems (ICPADS)*. Singapore, pp. 684–691. ISBN: 978-0-769-54903-3. DOI: 10.1109/ICPADS.2012.97.

You, F. and Leyffer, S. (Dec. 2011). "Mixed-Integer Dynamic Optimization for Oil-Spill Response Planning with Integration of a Dynamic Oil Weathering Model". In: *AIChE Journal* 57.12, pp. 3555–3564. ISSN: 1547-5905. DOI: 10.1002/aic.12536.

Zhang, Q., Skjetne, R., Løset, S., and Marchenko, A. (July 1–6, 2012). "Digital Image Processing for Sea Ice Observations in Support to Arctic DP Operations". In: *Proceedings of the ASME 2012 31th International Conference on Ocean, Offshore and Arctic Engineering, OMAE2012*. Rio de Janeiro, Brazil, pp. 555–561. ISBN: 978-0-791-84493-9. DOI: 10.1115/OMAE2012-83860.

Zhou, K. and Roumeliotis, S. I. (Aug. 2011). "Multirobot Active Target Tracking with Combinations of Relative Observations". In: *IEEE Transactions on Robotics* 27.4, pp. 678–695. ISSN: 1552-3098. DOI: 10.1109/TRO.2011.2114734.